PREDICTING THE BREAKDOWN PRESSURE IN HARD ROCK MATERIAL SUBJECTED TO HYDRAULIC FRACTURING AND QUANTIFYING FLUID FLOW WITHIN A FRACTURE NETWORK

by

Mark Baidoo

A thesis submitted in partial fulfillment

of the requirements for the degree of

Master of Applied Science (M.A.Sc.) in Engineering Science

Office of Graduate Studies

Laurentian University

Sudbury, Ontario, Canada

THESIS DEFENCE COMMITTEE/COMITÉ DE SOUTENANCE DE THÈSE
Laurentian Université/Université Laurentienne
Office of Graduate Studies/Bureau des études supérieures

Title of Thesis
Titre de la thèse: PREDICTING THE BREAKDOWN PRESSURE IN HARD ROCK MATERIAL SUBJECTED TO HYDRAULIC FRACTURING AND QUANTIFYING FLUID FLOW WITHIN A FRACTURE NETWORK

Name of Candidate
Nom du candidat: Baidoo, Mark

Degree
Diplôme: Master of Science

Department/Program
Département/Programme: Engineering Science

Date of Defence
Date de la soutenance: February 16, 2023

APPROVED/APPROUVÉ

Thesis Examiners/Examinateurs de thèse:

Dr. Marie Hélène Fillion
(Co-Supervisor/Co-drecteur(trice) de thèse)

Dr. Claudia Gonzalez
(Co-Supervisor/Co-directeur(trice) de thèse)

Dr. Eugene Ben-Awuah
(Committee member/Membre du comité)

Dr. Javier Andrés Vallejos Massa
(External Examiner/Examinateur externe)

Approved for the Office of Graduate Studies
Approuvé pour le Bureau des études supérieures
Tammy Eger, PhD
Vice-President Research (Office of Graduate Studies)
Vice-rectrice à la recherche (Bureau des études supérieures)
Laurentian University / Université Laurentienne

Abstract

This research is part of the Natural Heat Exchange Engineering Technology for Mines (NHEET) project conducted by Mirarco Mining Innovation. The NHEET project consists of developing a system using natural means to provide economically significant thermal regeneration capacity through a volume of rock fragments for ventilating mine workings. This system can provide heating (during winter) and cooling (during summer) of air on seasonal basis, without using artificial refrigeration. Optimizing the system requires creation of a specific volume of rock fragments having, among other criteria, a pre-determined porosity and fragment size distribution to meet the thermal storage and ventilation requirements of the mine site. This research is part of the NHEET project's scope of work and investigates an alternative system, which consists of a fractured rock mass with sufficient fracture density and connectivity to admit enough airflow for the NHEET system requirements. This alternative system has the potential of reducing the footprint at surface.

Firstly, the hydraulic fracturing (HF) method is investigated for preconditioning the rockmass with the objective of strategically creating additional fractures. Increasing the volumetric fracture intensity and fracture network connectivity within the rock mass can optimize airflow within the fracture network. A numerical predictive model for the breakdown pressure in hard rock subjected to hydraulic fracturing is developed using the lattice spring modeling method for HF simulation. The developed numerical model is calibrated based on the results obtained from a HF field experiment conducted in a northern Ontario mine.

Secondly, a laboratory experiment is conducted to quantify fluid flow through a fracture network. In this context, a 3D physical model representing a fractured rock mass is generated using 3D

printing technology. The 3D printed model is fixed into an experimental setup for fluid flow measurements. This experiment allowed for establishing the behaviour of the changing pressure to fluid transfer through fracture openings. The flow-pressure measurements are compared to a simple model for the volumetric flow rate in a block of naturally fractured rock with a number of fractures.

The numerical model developed, and laboratory results obtained in this thesis provide valuable information for the construction of a NHEET system. The numerical predictive model for the breakdown pressure in hard rock subjected to HF is a tool to evaluate the amount of fluid pressure needed to create additional fractures in the rock mass and facilitate the planning of HF operations. The pressure-flow rate laboratory measurements are key data that can be used to calibrate a subsequent numerical simulation at a larger scale, representative of the NHEET system. Additionally, direct fluid flow measurements in fracture networks are useful to assess the influence of various fracture properties (e.g. intensity, connectivity, aperture) on fluid flow.

Keywords: hydraulic preconditioning, lattice modeling, fracture initiation, 3D printing, Discrete Fracture Network, fluid flow through rock fractures, Natural Heat Exchange

Acknowledgments

My deepest appreciation goes to my supervisor, Assistant Professor Marie-Hélène Fillion and co-supervisor, Dr. Claudia González for their guidance and support during my M.A.Sc. program at Laurentian University. I wish to also express my sincere appreciation to MIRARCO Mining Innovation for the financial support for my M.A.Sc. program and also to the NHEET team for the guidance in my research. I am also grateful to Dr. Alexander Hutchison for the support and guidance in my experimental work and also extend my appreciation to Professor Dean Millar and to my committee member Professor Eugene Ben-Awuah.

Table of Contents

List of Tables

List of Figures

List of Appendices

Chapter 1

1 Introduction

For the past 50 years, Vale's Creighton mine has been using the Natural Heat Exchange Area (NHEA) which provides heating (during winter) and cooling (during summer) of air on seasonal basis (Acuña and Connor, 2010; MIRARCO, 2019). The system uses natural means to provide economically significant thermal regeneration capacity through a volume of rocks fragments for ventilating mine workings. Figure 1.1a shows Creighton's NHEA which allows the operation to avoid artificial refrigeration (Acuña and Connor, 2010; Saeidi *et al.*, 2017). Effectively, Figure 1.1b shows that the resulting temperature (green line) varies significantly less than the outside environment (red line).

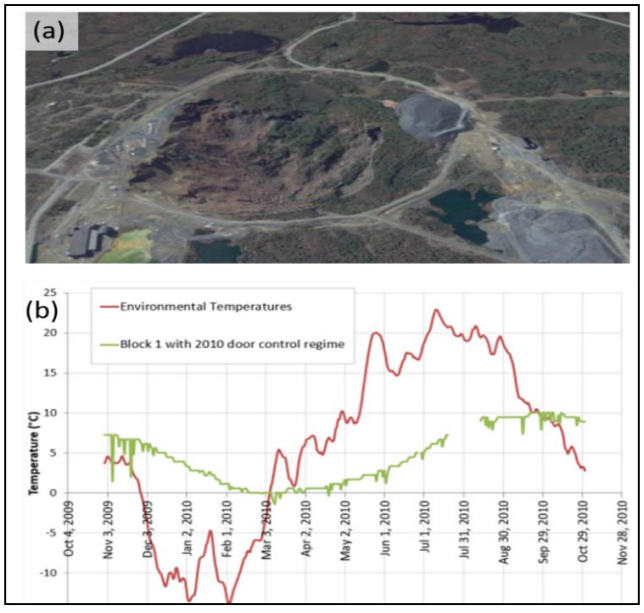

Figure 1.1 (a) Natural heat exchange area and (b) temperature profiles within the mine (green) and outside (red) (modified from MIRARCO, 2020b).

Building on previous studies regarding Creighton's NHEA (Acuña and Connor, 2010; Saeidi *et al.*, 2017). MIRARCO Mining Innovation, a not-for-profit organization owned by Laurentian University, investigated the constructability of a Natural Heat Exchange Engineering Technology (NHEET) system. The main objective is to establish a robust methodology for the engineering of a NHEET system (MIRARCO, 2019) for mine ventilation to be able to optimize and implement the NHEA exploited at Creighton Mine to diverse mine sites across Canada, and internationally. Optimizing the system requires to create a specific volume of rock fragments having, among other criteria, a pre-determined porosity and fragment size distribution to meet the thermal storage and ventilation requirements of the mine site. In the existing NHEA, the air is drawn from surface by fans located underground, through a mass of broken rocks contained in the open pit which connect to the underground mine workings (Acuña and Connor, 2010; Fava *et al.*, 2012).

1.1 Problem Definition

This research is part of the NHEET project's scope of work and investigates the use of hydraulic fracturing (HF) for strategically preconditioning the rockmass to facilitate the construction of the NHEET system. HF consists of initiating and propagating fractures into the rockmass by injecting a pressurized fluid into a borehole, which results in the modification of rock properties such as porosity and permeability (Adachi *et al.*, 2007; ASTM D4645-08, 2008). The HF technique, predominantly used to enhance the improvement of oil and gas production for decades has evolved since its introduction and is currently an essential technique in various sectors for different applications (Hubbert and Willis, 1957; Pettitt *et al.*, 2011; Li *et al.*, 2016; Huang *et al.*, 2020).

HF is one major technique for preconditioning in-situ rock materials to meet the purpose of engineering applications such as in block caving and mitigation of stresses in rockmass (ASTM

D4645-08, 2008; Gambino *et al.*, 2014). Examples of these applications in the mining industry are: i) use for hydraulic preconditioning (block cave mining) with the purpose of stimulating and inducing fragmentation; ii) use for distressing the rock mass to mitigate rock bursts (Gambino *et al.*, 2014; Katsaga *et al.*, 2015; He *et al.*, 2016); and iii) use for in-situ stress measurement at greater depth. Various applications in HF can be well differentiated with the methodology and purpose, which can vary greatly in terms of injecting pressure and volume of fluid injected, the scale of application, fluid with or without additives or proppants and fracture initiation, propagation or opening. For instance, HF applications for determining the strength of rockmass require, in some cases, a small volume of injecting fluid at high pressure compared to inducing fractures at greater depth within the rockmass with the same technique (Adams and Rowe, 2013). One key parameter of HF is the breakdown pressure which is the pressure at which the part of rockmass exposed to fluid pressure initiates its fracture (Lakirouhani and Farkhondeh, 2018; Zhang, 2019a; Wu *et al.*, 2020). This implies that the breakdown pressure can be used to determine fracture formation in rocks. It also aids in estimating rock stress such as maximum and minimum horizontal stress (Guo *et al.*, 1993) and at depth, the breakdown pressure is normally high due to the high stress and fracture toughness (Xi *et al.*, 2021).

Another critical aspect of the NHEET system is to ensure sufficient fluid flow through the system to provide economically significant seasonal/diurnal thermal regeneration capacity. An alternative system that could possibly reduce the footprint at surface (as opposed to a volume of rock fragments) is a specific volume of in-situ rock with sufficient fracture intensity and connectivity to admit enough flow for thermal regeneration capacity. HF can be used for preconditioning the rockmass, i.e. for creating additional fractures and increasing the volumetric intensity of fractures, which can improve the connectivity of the fracture network (Stacey, 2010; He *et al.*, 2016). In hard

rocks, fluid flow is highly sensitive to the aperture of fractures and their connectivity, as fractures are the preferential flow paths within the rockmass (Öhman, 2005; Blyth and Freitas, 2017). To verify the flow through a fractured rockmass, the flow associated with the secondary permeability (i.e. fracture permeability) is investigated with a small-scale laboratory experiment using 3D printing technology to build a 3D physical model of a fractured rockmass. 3D printing, as described by Jiang (2017) is an innovative manufacturing technology that enable the printing of objects through the accumulation of layers. This technology has gained numerous application in various field such as in mining and petroleum industries and has been used by Jiang (2017) Suzuki *et al.* (2017) and Suzuki *et al.* (2019) in their studies.

This research focuses on two main aspects: 1) develop a HF numerical predictive model that is able to quantify the breakdown pressure of the rock formation; this means the pressure required to initiate and develop a fracture, or the pressure to re-open a naturally pre-existing fracture; and 2) evaluate the secondary permeability of a fractured media. Both aspects of the research are beneficial for the NHEET project by: (a) quantifying the breakdown pressure which will be relevant for HP of rockmass to improve fracture intensity; and (b) investigating the fluid flow through secondary permeability of rockmass for the construction of the NHEET system.

1.2 Thesis Objectives

The thesis aims at improving the understanding of the HF technique for initiating fractures and preconditioning a rockmass, and evaluating the capability of the secondary permeability to admit enough airflow through a fracture network. The principal research objectives are to:

(1) Develop a predictive numerical model for fracture initiation using the HF method and calibrate the model based on the results from a hydraulic preconditioning (HP) field experiment. This involves the application of field HP data for software calibration to arrive at a set of parameters that gives good description of the rockmass behavior.

(2) Verify with direct airflow measurements collected during a laboratory experiment, whether the secondary permeability of a fracture network is able to admit fluid flow, as well as the behavior of the changing pressure to fluid transfer through fracture openings. A laboratory testing was set up for this study and the sample was a 3D physical model with fracture openings.

1.3 Research Methodology

The first step in this process was to conduct a comprehensive review of the literature specific to the two main topics of this thesis, i.e. hydraulic fracturing for rockmass preconditioning (or HP) and fluid flow through fractures. This was followed by reviewing the data collected during a HP field experiment in order to develop a numerical predictive model for fracture initiation (section 1.3.1). Section 1.3.1.1 summarizes the steps for rockmass characterization and model calibration and Section 1.3.1.2 describes the steps for numerical modeling. The flow through a fracture network was investigated with a laboratory experiment (section 1.3.2) using a lab-scale physical model. Section 1.3.2.1 presents the modeling process using the Discrete Fracture Network (DFN) generator MoFrac, section 1.3.2.2 highlights the steps for building the 3D printed physical model used for the flow experiment and section 1.3.2.3 presents the steps for the lab-scale experiment.

1.3.1 Predicting Fracture Initiation from Hydraulic Preconditioning

This section summarizes the methodology for the first topic of the thesis, which is the use of HF for rockmass preconditioning, by developing a numerical model for fracture initiation and calibrating the model based on the results obtained during a HP field experiment.

1.3.1.1 Rockmass Characterization and Model Calibration

The rockmass data were obtained from an operating mine in Northern Ontario in which an experimental field testing in HF was conducted. The rock type at the experimental depth of about 1350 m is norite. Rousell *et al.* (2009) presents the detailed geology of the Sudbury rock. The mechanical properties of the rock such as the uniaxial compressive strength (UCS), tensile strength (σ_t), density, Poison's ratio, Young Modulus, etc. were known from lab testing conducted by MIRARCO in the same type of rock for that rockmass and were selected for the numerical modeling. The UCS ranges between 50 – 90 MPa. This parameter was varied within that range of values to calibrate the numerical model. A comparison of the breakdown pressure obtained from the field experiment and the numerical simulation suggested that the modeling results can reliably represent the HP field results.

1.3.1.2 Numerical Modeling of the Rock Breakdown Pressure

The numerical model built to simulate the HP field experiment is performed with the software, XSite (Itasca, 2022), a HF simulator. A predictive model for fracture initiation and estimation of the rockmass breakdown pressure is obtained from this numerical simulation. The mechanical properties (e.g. UCS, tensile strength, fracture toughness, density, young modulus) of the rockmass are known and used as input for the model.

The natural stress regime and the model size are first defined. In this rockmass, the stress regime corresponds to the Canadian shield. The injection fluid properties (e.g. fluid type, injection pressure, etc.) are established based on the actual HP field experiment.

Following the code strategy, the numerical modeling is executed in two stages; the purely mechanical stage and the hydromechanical coupling stage. At the mechanical stage, the model is taken to equilibrium. At the hydromechanical coupling stage, the fluid and mechanical stages are coupled, resulting in the interaction between the mechanical processes and the fluid injection during the hydraulic fracturing. The formation and modification of the aperture of the microcracks to form a fracture plane in the rock occurs during the hydromechanical coupling. The breakdown pressure at which fracture is formed can be obtained in a pressure-time curve from the hydraulic fracturing process.

1.3.2 Laboratory Experiment to Evaluate Fluid Flow Through a Fracture Network

This section briefly introduces the second topic of the thesis about the lab-scale verification of the secondary permeability represented in a fracture network. A review of the literature was conducted to establish probable data for DFN modeling using the DFN generator MoFRAC (MIRARCO, 2022).

1.3.2.1 Discrete Fracture Network (DFN) Modeling

Naturally occurring discontinuities form complex fracture networks, which dominate the geometrical and fluid transport properties of a rockmass. A computational model such as DFN is used to represent these complex networks and their geometrical properties (Lei *et al.*, 2017). In this study, DFN modeling is used to represent a fracture network at the lab-scale. Two fracture sets

parameters, adopted from Esmaieli *et al.*(2010) are used to create the 3D DFN model with the software MoFRAC. By using input data such as fracture intensity, dip, dip direction, Fisher's constant, etc., it was possible to represent the DFN as fracture planes. The fracture aperture is assigned to each fracture using the software Solidworks (SolidWorks, 2021) to represent the secondary permeability of a rockmass. In Solidworks, the 3D DFN is extruded in a 3D cylindrical shape, to generate a 3D physical model of a fractured rockmass specimen.

1.3.2.2 3D Printed Physical Model

A physical DFN model is 3D printed (synthetic rockmass specimen) to represent an in-situ fracture network in a rock. The equipment to create the artificial rock specimen is a Stratasys Dimension SST 1200es 3D printer. Using this technology, it is possible to manufacture valuable physical representations of specific characteristics of rock such as the geometrical features of existing natural fractures. With a physical DFN model, direct measurements of fluid flow (Q) through the specimen can be performed at the lab-scale.

Thus, the DFN model representing a rockmass with in-situ fractures was used in a laboratory set-up to measure the fluid flow through the secondary permeability and also establish the behaviour of changing pressures to the flow through the represented rock mass. The experimental set-up is described in section 1.3.2.3.

1.3.2.3 Experimental Set-up and Data Collection

The laboratory experiment was carried out in the ventilation laboratory at Laurentian University. The lab-scale experimental setup consists of an anemometer calibration rig described in detail in section 4.3. It comprises a flow duct designed and built for fluid flow from upstream to downstream

of the setup. The flow duct is built to use a differential meter (orifice plates), which regulates and streamline the airflow (Morris and Langari, 2012). The 3D printed DFN model is fixed in the experimental setup. The motivation behind this experiment is to measure and verify the flow through the secondary permeability represented by DFN in the 3D physical model. This aims to contribute to assess the constructability of the NHEET alternative system by considering the flow through a preconditioned rockmass. A complete detailed description of this laboratory test is given in Section 4.3.

1.4 Thesis Structure

This research consists of five chapters. The following outline describes the structure of the thesis chapters:

- Chapter 1: Introduction

  The research motivations, objectives, and research methodology are introduced.

- Chapter 2: Literature review

  A review of HF technique and applications is provided and the field procedure is described. Background about the lattice spring modeling for HF numerical simulations is presented, including details about the code X-site from Itasca used in this study to simulate HF. All rock properties used for the numerical model are also provided. Additionally, background about fluid flow through fractures (secondary permeability) and DFN modeling is presented.

- Chapter 3: Numerical simulation of the breakdown pressure from a hydraulic

preconditioning field experiment in a deep northern Ontario mine.

The numerical modeling strategy, including the model setup, selection of input parameters obtained from a HP field experiment conducted in a Northern Ontario mine and numerical model calibration is described. Furthermore, a comparison of the field and numerical simulation results in terms of fluid pressurized into the rock mass versus time and the point at which the breakdown pressure is reached is presented.

- Chapter 4: Controlled lab-scale evaluation of the secondary permeability represented in a 3D printed discrete fracture network (DFN) model

  The modeling process with the DFN generator MoFRAC is described. Details about the three-dimensional physical model are provided, including the modeling process to obtain a volume with predetermined fracture aperture, the material used for the specimen and the validation process for the physical properties of the 3D printed DFN model. The lab-scale experiment for fluid flow measurement through the specimen model is described, including information about the experimental setup and the process for data collection and calibration. A comparison between the laboratory results and a basic empirical approach taken from the literature for estimating fracture volumetric flow rate is presented.

- Chapter 5: Conclusions and recommendations

  The main contributions of the research are summarized, and the limitations of the research are stated. Finally, recommendations are made for future work.

Chapter 2

2 Literature Review

To investigate the constructability of a NHEET system within a rockmass using the HP method, two distinct research topics were established. The first topic is to develop a predictive model for fracture initiation with the HF technique. Section 2.1 provides a general literature overview relevant to this first topic, including the hydraulic fracturing concept and its various applications, and the theory that supports the lattice spring numerical strategy to simulate HF is presented. Also, the details about the base model for predicting fracture initiation and the formulation base on which the numerical predictive model is developed using the Xsite software (Itasca, 2022) are provided. The background for the second topic consists of evaluating the secondary permeability of a fractured rockmass. Section 2.2 presents previous relevant investigations, including concepts about fluid flow through fractures and DFN modeling to represent systems of fractures (or fracture networks) within a rockmass.

2.1 Hydraulic Fracturing

2.1.1 Hydraulic Fracturing Technique and Applications

Hydraulic fracturing (HF) has been defined by ASTM D4645-08, (2008) as the "*fracturing of the rock by fluid pressure for the purpose of altering rock properties, such as permeability and porosity*". The HF methodology varies greatly in terms of injecting pressure and volume of fluid, the scale of application, the type of proppant and fracture propagation or opening (Adams and Rowe, 2013). Other definition indicates that HF is the initiation and propagation of fractures that are induced to create a network of highly conductive fractures in the area surrounding a wellbore (Adachi *et al.*, 2007; Barati and Liang, 2014).

Early analyses of the hydraulic fracturing process assumed that a single fracture is developed as a result of the injection in a small isolated interval of a borehole delimitated by two off-pressurized packers in a stressed elastic continuum (Fairhurst, 2013). The pre-existing natural fractures have a significant influence on fracture development (Fairhurst, 2013), and on the associated distributions of pressurized fluid flow and stresses in the rock (Lavrov, 2016; Zhang, 2019a). This technique has been developed in the late 1940's to enhance recovery from petroleum reservoirs. Today, HF can be applied to various subsurface engineering projects. In differentiating hydraulic fracturing application, Adams and Rowe, (2013) described various hydraulic fracturing applications which includes; enhancing water well production by fracturing rock aquifers; preconditioning rockmass to reduce the size of caving material; stress measurement in the mines, tunnels, dams which is carried out to estimate the in-situ stresses in rockmass; and enhanced geothermal energy production where hydraulic fracturing is used to established a flow path between the injection and extraction wells. Adams and Rowe, (2013) indicated that the various technique can be characterised with the amount of fluid injection during the application, the amount of pressure required, whether fracture propagation is required or not (e.g. in stress measurement fracture propagation is not required), injectate volume, nature of injectate (e.g. inclusion of chemical additives) and the usage of proppant.

2.1.2 Applications in Oil and Gas Production Industry

In the oil and gas industry, HF has been successful in yielding production results by enhancing the rock permeability and porosity (Hubbert and Willis, 1957; Haimson, 1993; Haimson and Cornet, 2003). It is now a major technique employed to optimize and improve energy mining efficiencies in petroleum industries (Pettitt *et al.*, 2011; Cheng and Zhang, 2020; Huang *et al.*, 2020). One of its application in oil and gas industry is to stimulate production wells by propagating a fracture

from a wellbore towards the reservoir using a fluid driving force from the surface into the rockmass. The fracture formed constitutes a highly permeable path, which optimize the flow of hydrocarbon from the reservoir to the well. Mostly additives and proppants are adopted to keep the fractures open (Lhomme, 2005; Adams and Rowe, 2013). The HF technique can be initiated in stages within the reservoir to connect several oil-bearing layers, as indicated in Figure 2.1.

The central purpose of HF is to engineer the properties of a reservoir rock by inducing new fractures and improving the permeability of the existing fracture network at the hosting rockmass. This purpose ensures the creation of pathways to connect different volumes within the reservoir and also optimizing the conductivity between pre-existing joints (Haimson and Fairhurst, 1969; Pettitt *et al.*, 2011).

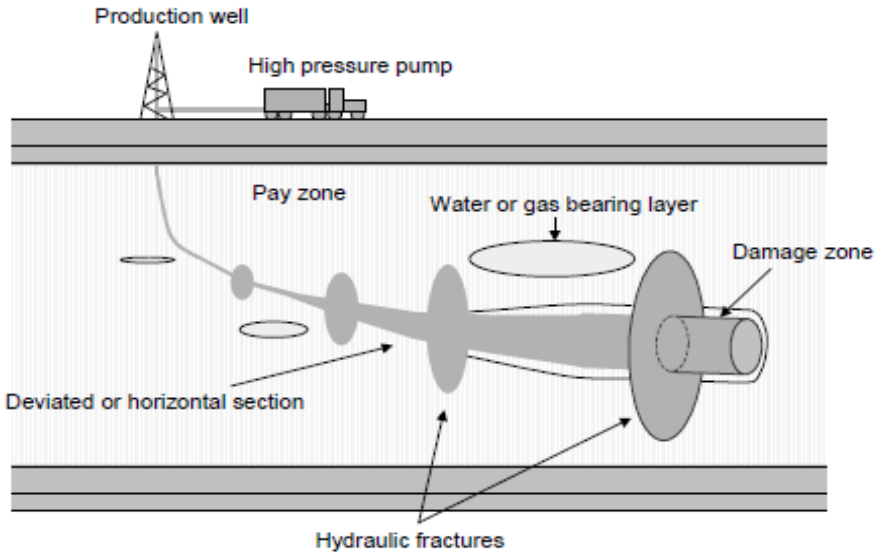

Figure 2.1 Simulation of horizontal wellbore by hydraulic fracturing technique (Lhomme, 2005)

2.1.3 Applications in Mining and Civil Industries

Lin et al. (2018) study suggests that the knowledge of the stresses in the rockmass is useful in identifying high risks zones for potential failure such as rock failure within the mine; and knowing the stress state of the ground is a prerequisite for safety assessment in both mining and surface construction (Farkas *et al.*, 2019; Yang *et al.*, 2020). HF can be used to estimate the stress state in the in-situ rockmass at various depth (Haimson and Cornet, 2003; ASTM D4645-08, 2008).

Several studies have investigated the application of hydraulic fracturing techniques for in-situ stress measurement in various conditions (Wang *et al.*, 2017; Han and Yin, 2018; Rubtsova and Skulkin, 2018; Farkas *et al.*, 2019; Yang *et al.*, 2020). In-situ stress measurement techniques available are discussed by Amadei and Stephansson (1997) and Lin et al. (2018). These techniques measure borehole deformation via specific instrumentations like the United State Bureau of Mines (USBM) deformation gauge (Cai, 1990). In different rock conditions, the technique has been successfully used to estimate the stress state of the in-situ rock material for decades (Healy and Zoback, 1988; Hayashi *et al.*, 1997). It has been a key technique for different stress magnitudes and orientations determination at significant depth over relatively large volume of rockmass within the ground (Haimson, 1993; Farkas *et al.*, 2019). Yang et al., (2020) conducted a field experiment at a depth of 170 – 2050 m and demonstrated the use of the technique over a wider range of depth.

Another HF application in mining is for rockmass stimulation for block caving operations by improving caveability and fragmentation of the blocks. Preconditioning effectiveness is achieved by the introduction of additional fractures within the rockmass (Katsaga *et al.*, 2015; He *et al.*, 2016). The technique is also widely used in coal mining with some common applications such as

improving the permeability in gas-bearing coal seam (Huang *et al.*, 2012; Dai and Zhou, 2020) and controlling hard roof rock-burst (Fan *et al.*, 2012).

Lin et al. (2018) pointed out that, with the usage of impression packer, compass, borehole scanning technique and appropriate ancillary equipment, the stress orientations can be estimated from the hydraulic fracturing test. This view is supported by Haimson and Fairhurst (1969) that stated "the estimation of the in-situ stress orientation can be deduced from the orientation of the fractures". The magnitudes of these stresses are estimated from test results and, as noted by Farkas et al. (2019), HF tests are repeated in a single experiment to ensure consistency and good estimation. In the in-situ stress measurement, it is needed to create fractures of smaller radius comparing to full-scale hydraulic fracturing where larger radius of fractures is created at far depth such as application in the oil and gas industries (Serdyukov *et al.*, 2016).

2.1.3.1 Field Procedures for Hydraulic Fracturing

HF is a borehole designed technique which enables the test to be executed at a point that can be located at different intervals within a borehole (Haimson and Cornet, 2003; Farkas *et al.*, 2019; Yang *et al.*, 2020). HF application in mining as described by Hayashi et al. (1989), Wang et al. (2017) and Yang et al. (2020) has been successful at various depth in hard rock. HF can be simplified into the following processes; (i) the mechanical deformation of rock induced by fluid pressure; (ii) fracture initiation (iii) the flow of fluid within the fracture; (iv) the fracture propagation (Adachi *et al.*, 2007); and (v) the leak-off of fluid from the fracture into the surrounding rock (Hu *et al.*, 2014).

First, a borehole is drilled by diamond drilling and coring technique or by rotary drilling to a required depth prior to the execution of the HF process. The borehole can be vertical, horizontal

or inclined to a preferred orientation (Haimson and Cornet, 2003; ASTM D4645-08, 2008; Rubtsova and Skulkin, 2018). Typical borehole diameters ranges from 76 to 96 mm (Haimson and Cornet, 2003). By examining the rock core extracted from the drilled borehole and applying a geophysical tool such as borehole cameras or televiewers, a section at an appropriate depth, or test interval is selected for injection (Haimson and Cornet, 2003; ASTM D4645-08, 2008; He *et al.*, 2016).

Straddle packers are pressurized and anchored to the wall of the borehole to seal off the selected interval at the appropriate depth (Zang and Stephansson, 2009; Farkas *et al.*, 2019). The sealed off interval is pressurized gradually by injecting fluid under pressure until the borehole wall starts being damaged (Zang and Stephansson, 2009; Cheng and Zhang, 2020) and the peak pressure or the breakdown pressure is obtained. Fracture initiation precedes the breakdown pressure. Once the initiation pressure is reached, microcracks are initiated and extends as the injection rate increases until the breakdown pressure is attained (Ibrahim and Nasr-El-Din, 2018; Cheng and Zhang, 2020; Huang *et al.*, 2020).

Pressure from the fluid creates one or more fractures extending into the rock medium (Ching and Weng, 2014). The peak pressure at which the borehole wall fractures is the breakdown pressure (P_b) (Haimson and Cornet, 2003; ASTM D4645-08, 2008) and has been found to relate to the minimum principal stress (Li *et al.*, 2016; Ibrahim and Nasr-El-Din, 2018; Huang *et al.*, 2020). At this stage, the operator stops pumping without venting and the interval pressure decays to a lower level at which the opened fractures close. The pressure at which the fracture closes is the shut-in pressure (P_S). The pressurization process is repeated for different cycles with the same flow rate to obtain the fracture reopening pressure and subsequent shut-in pressure. The reopening pressure

does not overcome additional tensile strength (T) of the rock and is generally expected to be lower than the breakdown pressure (Haimson and Cornet, 2003; ASTM D4645-08, 2008). Once the test cycles are completed, the packers are deflated and retrieved from the hole or moved to another test interval (Farkas *et al.*, 2019).

Figure 2.2 (a-c) modified from Zang and Stephansson (2009) is a typical hydraulic fracture schematic diagram of a downhole hydraulic fracturing equipment setup, pressure-time curve and fracture mechanic. In Figure 2.2a, no. 1 is the pressure pipe for inflating the parkers, no. 2 is the pressure pipe for pressurizing the sealed section and no. 3 are the packers. In Figure 2.2b, P_{b1}, P_{b2} and P_{s1}, P_{s2} represent the breakdown/ reopening pressure and shut-in pressures for cycle 1 and 2 respectively. Figure 2.2c, indicates the respective points on the pressure-time curve representing the fracture initiation pressure P_{fl}, breakdown pressure P_b, fracture propagation pressure, P_{fp}, shut-in pressure P_s and fracture closure pressure P_{fc}. Point 1-4, represent the various stages of fracture mechanics from fracture initiation to the closure of open fracture after pumping is stopped. The hydraulic fracture induced within the 1 m sealed section is shown in Figure 2.2a.

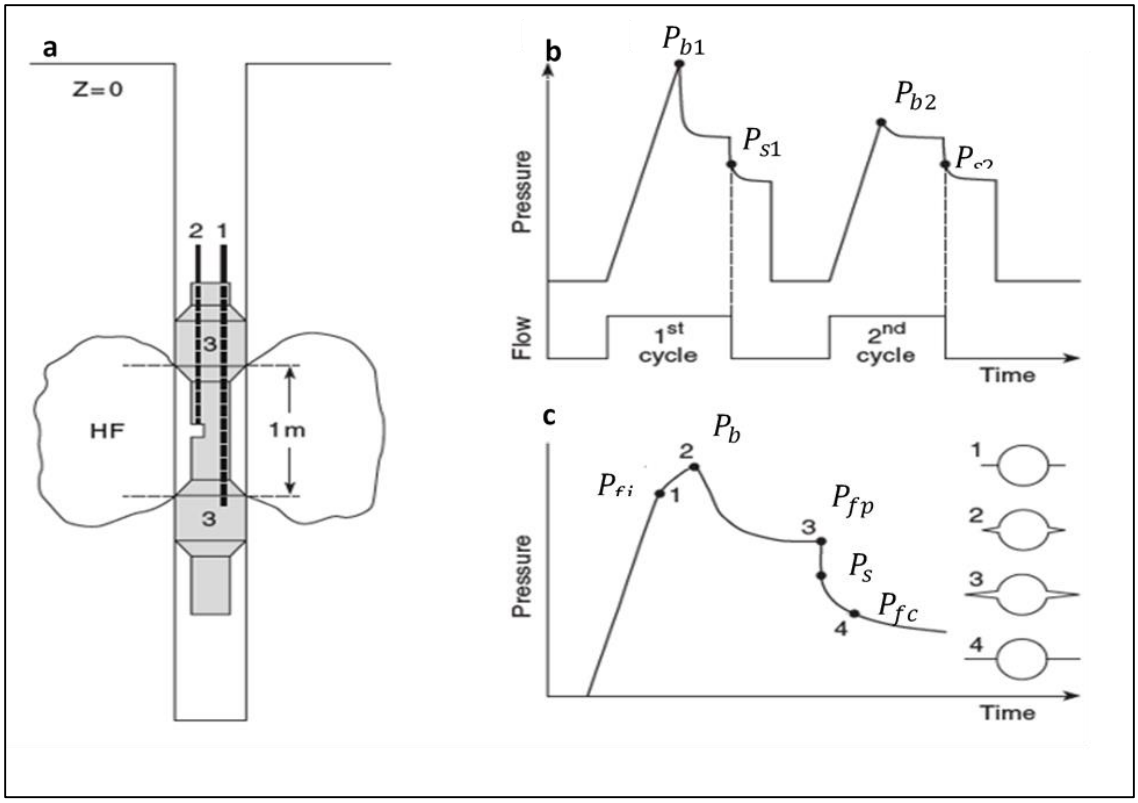

Figure 2.2 Hydraulic fracture schematic diagram of (a) a downhole HF equipment setup, (b) the pressure-time curve and (c) the 4 stages of fracture mechanic (modified after Zang and Stephansson, 2009).

The observation of the fractures and estimation of the fracture orientation is inferred from the oriented impression packers or borehole logging tools such as borehole televiewer (Figure 2.3) (Zang and Stephansson, 2009; Farkas *et al.*, 2019). Tiltmeter monitoring is another technique capable of monitoring the volume, strike and dip and mapping of fractures at depth as discussed by Chen and Jeffrey (2009).

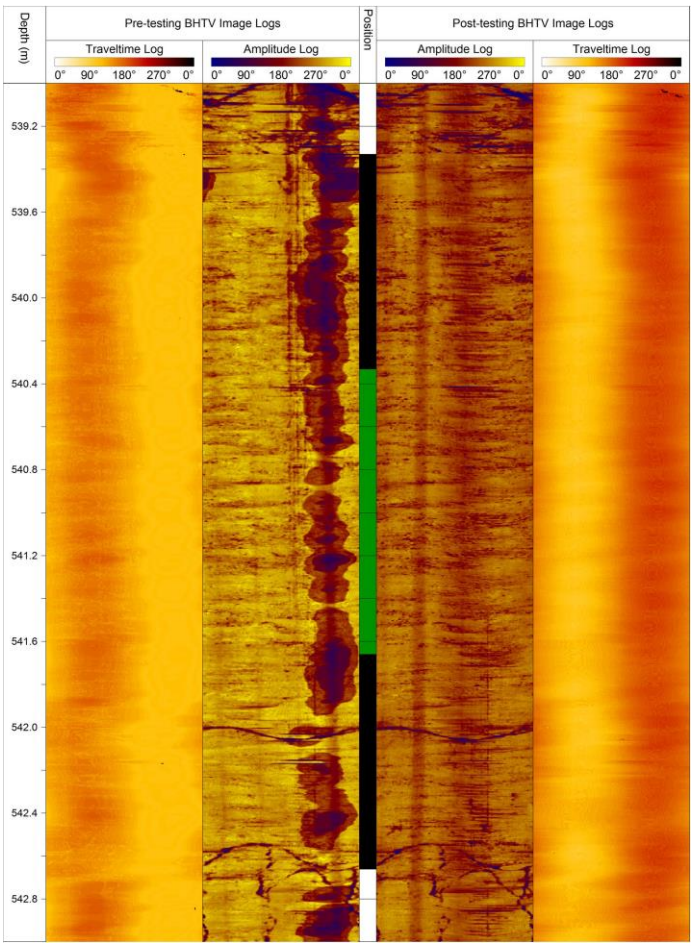

Figure 2.3 Pre and post testing images from borehole televiewer (modified after Farkas et al. 2019)

The magnitude of pressure required in generating, propagating, extending and keeping the fractures open is related to the magnitude of the existing stresses (Farkas *et al.*, 2019). A review by Lin et al. (2018) indicated that hydraulic fracturing is influenced by the fault mechanisms in the rockmass. Yang et al. (2020) pointed out that, for field experiments at depth of 170-800 m range, the in-situ stress relationship is $\sigma_H > \sigma_h > \sigma_v$, which is an indication of reverse faulting and at depth of 1000-2021 m, the stress relationship favors strike-slip faulting i.e. $\sigma_H > \sigma_v > \sigma_h$, where σ_H, σ_h and σ_v are the in-situ stresses corresponding to the maximum and minimum horizontal, and vertical stresses respectively. Figure 2.4 illustrates the different fault regimes

(Markou and Papanastasiou, 2018). Figure 2.5 provides a summary of the stress state for the formation of either type of fractures.

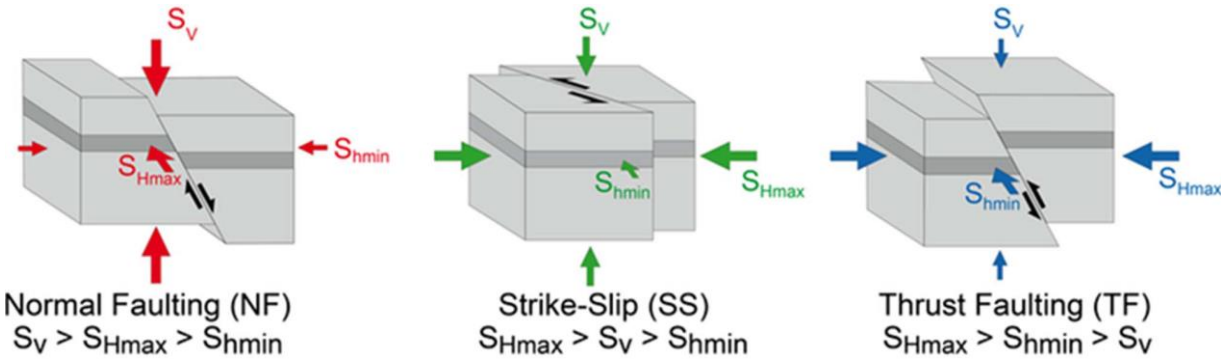

Figure 2.4 Main fault regimes (Markou and Papanastasiou, 2018)

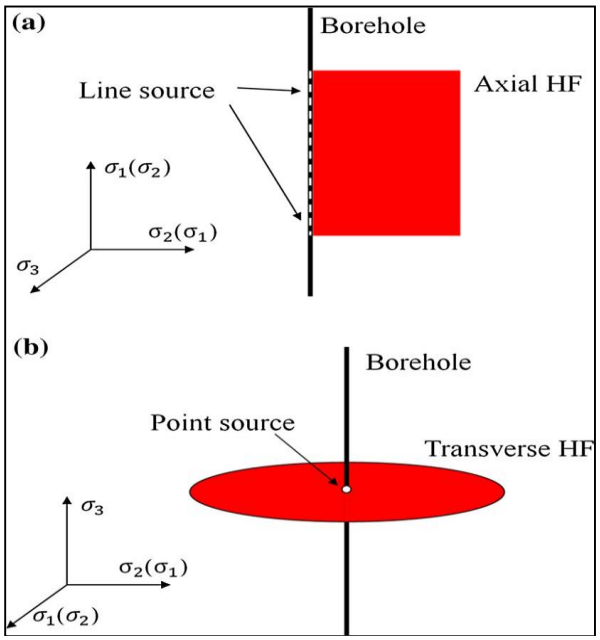

Figure 2.5 Stress conditions for the formation of (a) axial and (b) transverse fractures (He *et al.*, 2016)

In the application of HF for in-situ stress determination, the vertical borehole is assumed to be parallel to the vertical stress σ_v. The shut-in pressure is required in the estimation of the in-situ stress (Zang and Stephansson, 2009). The shut-in pressure equilibrates the stress normal to the fracture which is used in addition to tensile strength and pore pressure in arriving at the equation 2.1 for the minimum horizontal stress σ_h (Haimson and Cornet, 2003; ASTM D4645-08, 2008).

$$\sigma_h = P_{s1} \tag{2.1}$$

Where, p_{s1} is the shut-in pressure for the first pressurization cycle.

The maximum horizontal stress estimate with or in the absence of pore pressure is given by equation 2.2 and 2.3 respectively.

$$\sigma_H = 3\sigma_h + T - P_{bi} + P_0 \tag{2.2}$$

$$\sigma_H = 3\sigma_h + T - P_{bi} \tag{2.3}$$

Where P_{bi} for the first pressurization cycle is the breakdown pressure , i is the cycle number and P_0 is the pore pressure. The tensile strength (T) value is determined in the laboratory from the core samples (Haimson and Cornet, 2003).

When the fracture is observed to close fully after each pressurization cycles, the reopening pressure P_{bi} is estimated to be the difference between the breakdown pressure and the tensile strength of the rock (ASTM D4645-08, 2008). This implies equation 2.2 and 2.3 become:

$$\sigma_H = 3\sigma_h + T - P_{b2} + P_0 \tag{2.4}$$

$$\sigma_H = 3\sigma_h + T - P_{b2} \quad (2.5)$$

Where P_{b2} is the reopening pressure for the second pressurization cycle, and $P_{b2} = P_{b1} - T$ (ASTM D4645-08, 2008).

Vertical stress can be estimated from the weight of the overburden and the thickness of the rock layer as given by Hudson and Harrison (1997), Haimson and Cornet (2003) and ASTM D4645-08 (2008) in equation 2.6.

$$\sigma_v = \sum_{i=1}^{n} \gamma_i D_i \quad (2.6)$$

Where γ_i is the mean unit weight of rock layer i over the test section, D_i is the thickness of the rock layer i, and n is the number of rock layers overlying the test section.

2.1.3.2 HF Application for Rockmass Preconditioning and Destressing

Hydraulic preconditioning (HP) entered in the mining industry as one of the techniques efficiently used to destress the highly stressed rockmass. This is because HP can alter the character of the rockmass in such a way that the magnitude of mining induced seismic events is reduced in highly stressed ground. The rockmass is subjected to natural in-situ stresses and underground excavation can result in unavoidable induced stress redistribution, which can result in high stress and energy stored concentration in the rockmass (Feng, 2018). As a result, the excavated surfaces may experience damage and bursting events (in high storage energy locations) during the re-equilibrium processes. The HP technology has been successfully employed for such purposes at El Teniente Mine in Chile for tunnel development and selection of exploration method (Pardo and Rojas, 2016; Rojas and Landeros, 2017).

Some approaches like destress drilling, destress blasting, application of dynamic support system are used to mitigate potential rock burst with reasonable excavation method (Feng, 2018). Destress blasting technique has been used in a mine to shift the critical stress level further inside the rockmass by fracturing the rockmass and reducing the stress level in an area designated for excavation (Konicek *et al.*, 2011; Saharan and Mitri, 2011; Mazaira and Konicek, 2015). Some of the limitations for the technique are: limited understanding about the extent and direction of fractures growth, limited in depth of application, the possibility of cutter failure and floor heave from this technique, and high cost of operation (Konicek *et al.*, 2011).

Stress-induced rock fracturing and failures such as rock bursts are unavoidable near excavations, far from mine openings and within the rockmass. The sudden release of stored energy results in violent failure of the rock such as rock bursts. The severity of rock burst increases with depth (Kaiser and Cai, 2012; Kaiser *et al.*, 2013; Cai and Kaiser, 2018; Li *et al.*, 2019). Seismicity is related to rock burst or its magnitude, though not all rock burst are seismic event (Cai and Kaiser, 2018; Li *et al.*, 2019). Cai and Kaiser (2018) review on rock burst, indicated that HF has been introduced as an effective means of seismic energy release control. Zhu et al. (2017) demonstrated that HF in deep underground coal seam, reduces the stress and strain energy in the rockmass and can be used to mitigate rock bursts. Lekontsev and Sazhin (2008) observed the potential of rockmass pressure re-distribution in underground mine by HF.

Discussing rockmass preconditioning by means of HF versus destress blasting, some authors found that the former addresses the shortfall of the destress blasting (He *et al.*, 2016). Some of these are the lower cost associated with using HF, which is also noted by Van As and Jeffrey (2000), and its application at various depths (Haimson and Fairhurst, 1969). Thus, the application of HF is an

effective destressing method for avoiding rock burst in deep mining workings comparing to labour-intensive, time-consuming and high cost conventional destress measures in deep underground workings (Zhu *et al.*, 2017).

One of the first application of HF for caving in mining was in 1997 (Van As and Jeffrey, 2000). Application of HF to rockmass preconditioning for caving is carried out by inducing fractures at interval for every few meters along each hole for all different boreholes intended for the caving purpose (Chen and Jeffrey, 2009). HF application in rockmass preconditioning has shown indications of reduction in microseismicity during caving of a preconditioned volume of rockmass (Katsaga *et al.*, 2015).

HF was observed to contribute massively in the reduction of the seismic events and magnitude at the El Teniente Mine in Chile, specifically within the TEN-SUB-6 mining block as reported in Figure 2.6 (Pardo, 2015; Cai and Kaiser, 2018). Figure 2.6 shows the reduction in seismic events resulting in an increased production rate from 1992 to 2015.

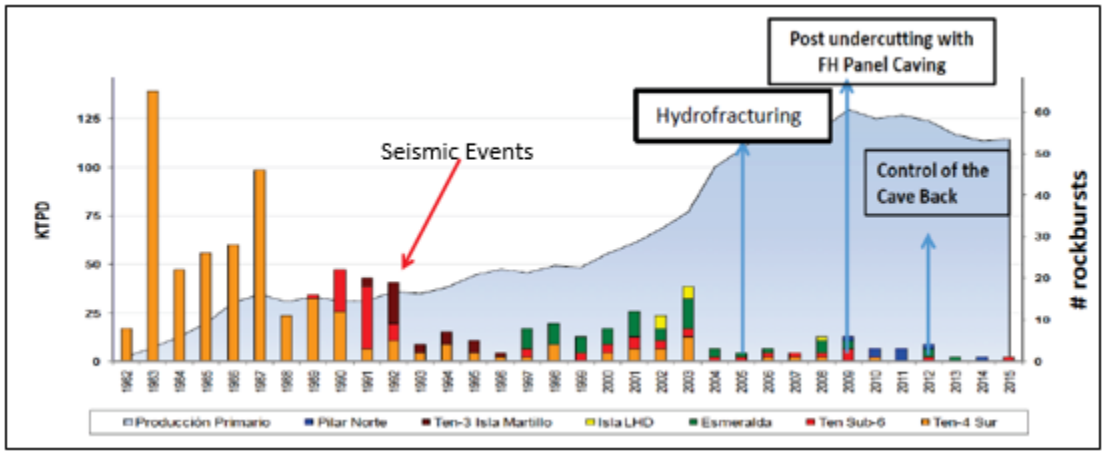

Figure 2.6 HF and improved ground support system impact on rock burst history at El Teniente Mine (Pardo, 2015; Cai and Kaiser, 2018)

HF, as published by Rojas and Landeros (2017), has also been used in EL Teniente Mine tunnel development to achieve various seismic response in a large volume of rockmass by introducing closely spaced fractures. Rojas and Landeros (2017) further indicated that hydraulic fracturing resulted in seismic hazard reduction for large volume of rockmass, but did not affect the potential of large seismic sources outside of the hydraulic fractured zone.

HF has been applied in destressing highly induced stress zones (Zhao *et al.*, 2013) and has been successful in overcoming the limitations of the destress blasting. In this context, an experimental test was carried out in an operating mine located in northern Ontario (Canada), by a researcher team of the Geomechanics Research Centre at MIRARCO Mining Innovation. The HP test was performed until reaching fracture initiation and natural fracture opening (Baidoo *et al.*, 2023). More details of the field test can be found in Maloney and Gonzalez (2017). When planning HP operations, the estimation of the breakdown pressure, i.e. the fluid pressure needed to initiate and propagate a fracture or reopen an existing fracture, is a key parameter. This is the goal of the numerical modeling described in Chapter 3.

2.1.4 Description of Lattice Formulation and Xsite Software

2.1.4.1 Background to Lattice Spring Modeling

HF can be executed at various depths within the rockmass. Several discontinuities such as fractures, joints, fissures, faults, etc. together with the intact material makes up the large volume of rockmass. The rockmass depicts anisotropy due to the discontinuities embedded within it, forming a fracture network. Generally, discontinuities are soft with weaker strength comparing to the intact rock material hosting them. The pre-existing natural fractures patterns within the rockmass produces anisotropic behaviour of the rockmass. Their presence decreases the stiffness

and strength of a region with increasing region size until a representative volume is reached. Thus, the presence of discontinuities produces a scale effect within the rockmass (Ivars *et al.*, 2011; Wang *et al.*, 2016) until the volume beyond which the rockmass behaves as continuous. This scale effect is illustrated in Figure 2.7.

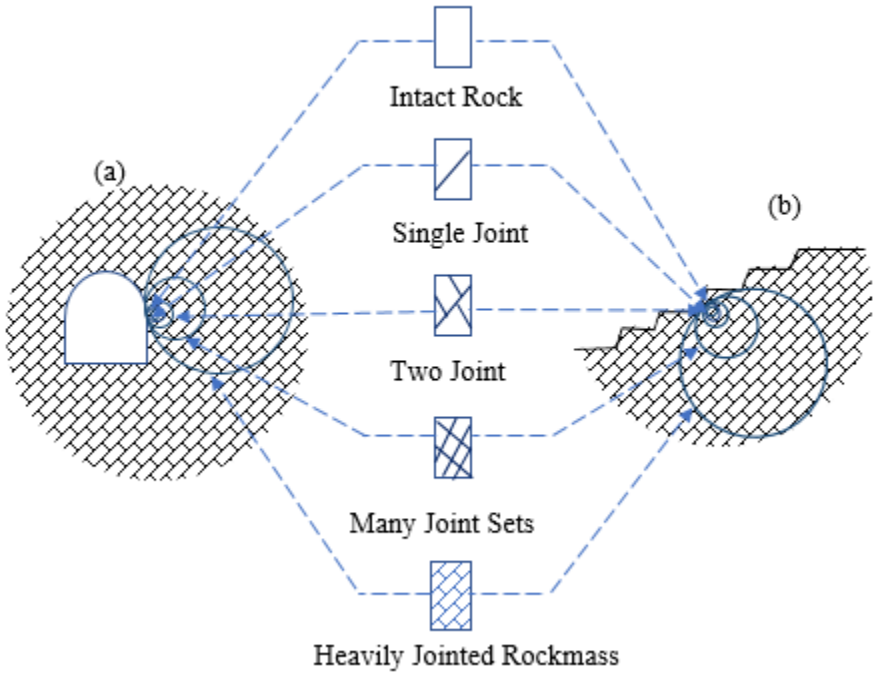

Figure 2.7 Scale effect of discontinuities in rockmass (a) underground excavation (b) open pit (modified after Hoek *et al.*, 2000)

The synthetic rockmass (Figure 2.8) has been developed based on bonded particle model and smooth joint modeling (Ivars *et al.*, 2011; Xing *et al.*, 2018) to represent some cases of rock mass numerically. The development of Synthetic Rockmass Modeling (SRM) is useful in studying the mechanical behaviour of jointed rockmass in the 3D space. It represents the intact rock as an

assembly of bonded particles and the joints with Discrete Fracture Network (DFN) (Pierce *et al.*, 2009; Ivars *et al.*, 2011). The SRM combines; (1) the bonded-particle model (BPM) to represent rock matrix, and (2) the smooth joint model (SJM) to represent the mechanical behaviour of pre-existing fractures (Damjanac *et al.*, 2016; Xing *et al.*, 2018). In the BPM, the particles elastic properties of the contact such as shear and normal stiffness can be calibrated to the desire elastic properties such as Young's modulus and Poisson's ratio. The contact of the bond in BPM is brittle and the breakage of these bonds connect together to form microcracks. The BPM also provides no limitation with regards to the fracture propagation path and complexity of fracture patterns. However, the selected particle size (resolution) in BPM is usually not related to the actual roughness of the pre-existing joints which has been accounted for in the SJM (Damjanac *et al.*, 2016; Qiu, 2021). Also, explicit modeling of discontinuity in BPM can be carried out with SJM (Ivars *et al.*, 2011).

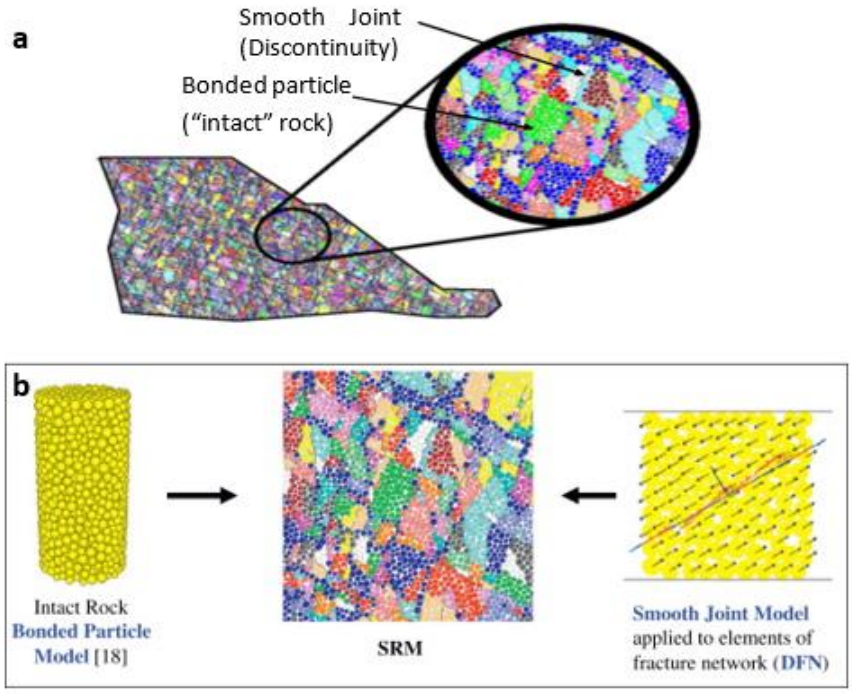

Figure 2.8 (a) A two-dimensional SRM model showing bonded particles and a smooth joint and (b) Basic components of synthetic rockmass (Pierce *et al.*, 2009; Ivars *et al.*, 2011)

The smooth-joint contact model is developed in the PFC for simulation of joint planes within the bonded assembly. It simulates the behaviour of an interface regardless of the local particle contact orientations along the interface. Sliding along a smooth planar feature can be modelled by assigning smooth-joint models to all contacts between particles that lie upon opposite sides of the macroscopic joint plane (Figure 2.9). Particle pairs joined by a smooth-joint contact may overlap and "slide" past each other, instead of being forced to move around one another as indicated in Figure 2.9 (Ivars *et al.*, 2008; Pierce *et al.*, 2009). Figure 2.8, 2.9 and 2.10 give a 2D representation of bonded particle in synthetic rockmass, joint geometry and smooth joints contact model respectively.

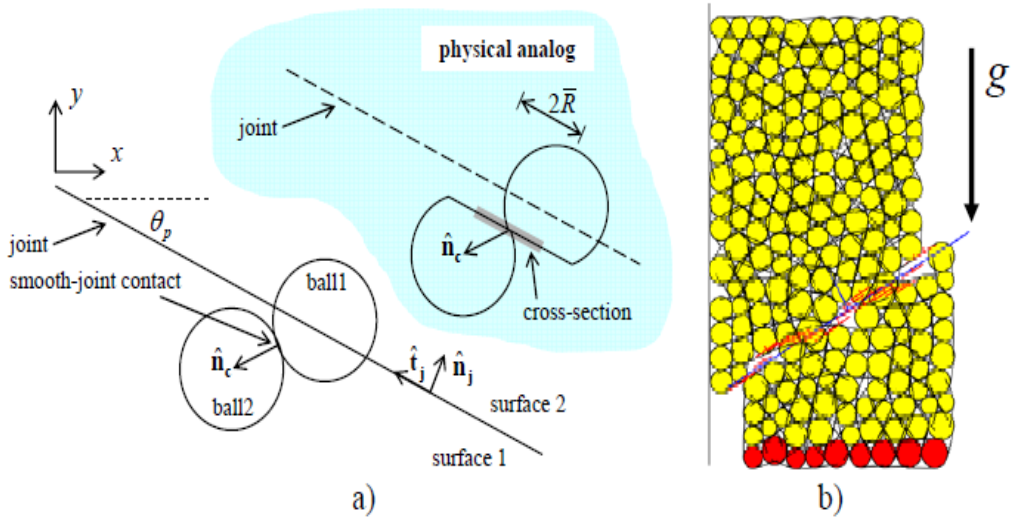

Figure 2.9 (a) Effective joint geometry, and (b) 2D specimen with frictionless joint loaded by gravity (Ivars *et al.*, 2011).

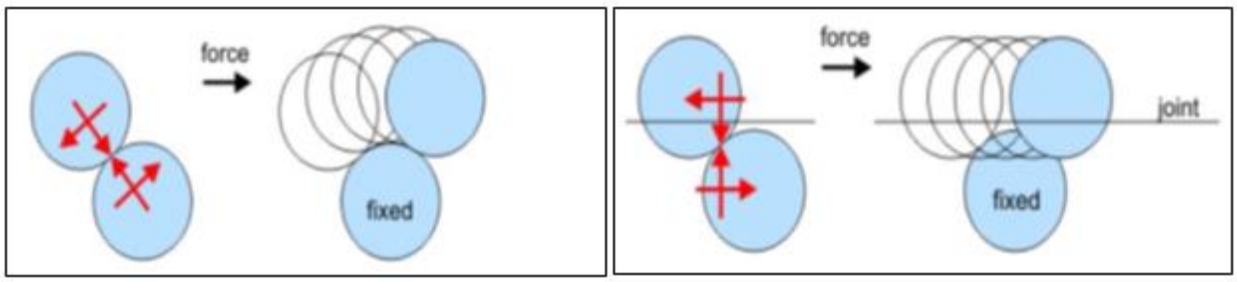

Figure 2.10 (a) How the smooth joint model can realign the default contact orientation to honor a macroscopic joint orientation (Pierce *et al.*, 2009)

SRM employs assemblies of circular/spherical particles bonded together. Computational efficiency can be realized with the lattice approach described in Section 2.1.4.2 where the point masses (nodes) connected by springs, replaces the balls and contacts (respectively) of PFC3D (Damjanac *et al.*, 2011).

2.1.4.2 Lattice Model and Lattice Formulation in Xsite

XSite (Itasca, 2022) is a code based on the SRM and lattice methods. Xsite numerical code implements the SRM in lattice method. Details of the software formulation and user guide is captured in (Damjanac *et al.*, 2011, 2020; Itasca, 2013). This provides simplification of the numerical modeling and improvement in computational efficiency. The SRM is used to represent the mechanical behaviour of the rockmass in three dimensions. The rockmass characteristics are represented by bonding of spherical particles to each other using the bonded-particle model (BPM) and the lattice approach ensures the representation of the physics, essential for the simulation of HF by giving a representation of the mechanical behaviour of a brittle rock (Potyondy and Cundall, 2004; Damjanac *et al.*, 2016; Djabelkhir, 2020).

Advanced application of SRM concept is based on the lattice representation of brittle rock matrix. The lattice consists of point masses, or nodes, which are connected by springs. The nodes and springs replace the balls and contacts of PFC3D respectively, and provides much computational efficiency (Damjanac *et al.*, 2016; Xing *et al.*, 2018). The lattice, as described by Damjanac *et al.* (2016), is a quasi-random three-dimensional array of nodes (with given masses) connected by springs. It is formulated in small strain with each node connected by two springs, one representing the normal and the other shear contact stiffness. The springs represent the elasticity of the rockmass and the tensile and shear strengths of the springs control the macroscopic strength of the lattice.

Figure 2.11 gives a representation of the lattice spring model as given by Wong et al. (2015). This model shows a clear geometry of how the nodes and springs are arranged and connected. The lattice simulation is a simplification of the bonded particle model (BPM) where the finite sized particles and contacts are replaced by nodes and springs (Djabelkhir, 2020) as shown in Figures 2.11 and 2.12.

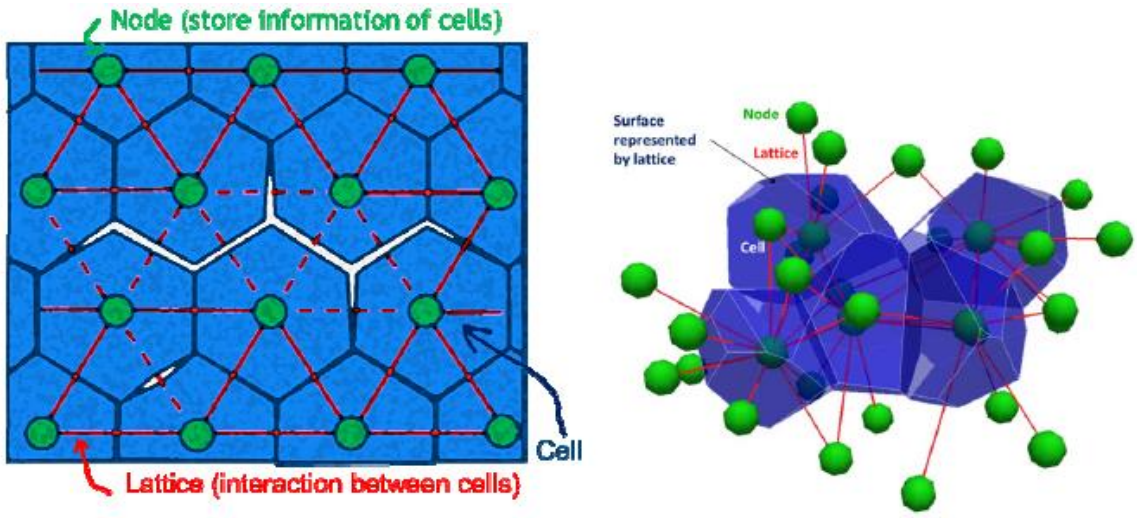

Figure 2.11 Illustration of the basic components of lattice spring model (Wong *et al.*, 2015)

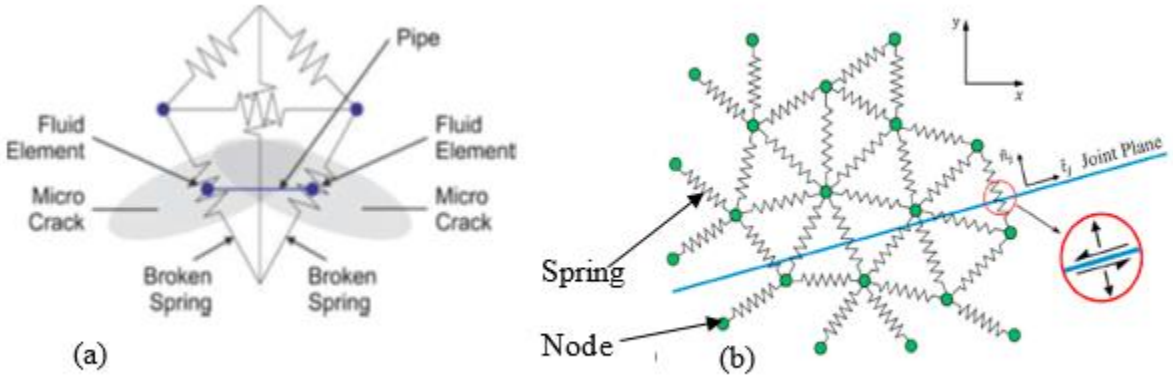

Figure 2.12 (a) Pipe network for fracture flow and formation of microcracks (Damjanac *et al.*, 2016) (b) Schematic of a lattice array with joint plane through springs (modified after Fu et al., 2019)

In XSite, the translational degree of freedom, the direction that the nodes can move or rotate is calculated using the central difference equations as given in equation 2.7 and 2.8 (Damjanac *et al.*, 2020). The nodes angular velocity is also solved by equation 2.9 (Damjanac *et al.*, 2020). The equation of motion for all nodes is carried out by using explicit numerical method.

$$\dot{u}_i^{(t+\nabla t/2)} = \dot{u}_i^{(t-\nabla t/2)} + \sum F_i^{(t)} \Delta t/m \tag{2.7}$$

$$u_i^{(t+\nabla t/2)} = u_i^{(t-\nabla t/2)} + \dot{u}_i^{(t+\nabla t/2)} \Delta t \tag{2.8}$$

$$\omega_i^{(t+\Delta t/2)} = \omega_i^{(t-\Delta t/2)} + \frac{\sum M_i^{(t)}}{I} \Delta t \tag{2.9}$$

Where $\dot{u}_i^{(t)}$ and $u_i^{(t)}$ are the velocity and position (respectively) of component i $(i = 1,3)$ at time *t*, $\sum F_i$ is the sum of all force-components i acting on the node of mass m, with time step Δt. ω_i represents the angular velocities of component i $(i = 1,3)$ at time t. $\sum M_i^{(t)}$ is the sum of all moment-components acting on the node of moment of inertia I.

The normal and shear forces acting on the springs are updated and calculated with equations 2.10 and 2.11 (Damjanac *et al.*, 2020), using the relative displacements of the nodes. A condition is automatically established such that if the force exceeds the calibrated spring strength, the spring breaks and, at this point, a microcrack is formed.

$$F^N \leftarrow F^N + \dot{u}^N k^N \Delta t \tag{2.10}$$

$$F^S \leftarrow F^S + \dot{u}^S k^S \Delta t \tag{2.11}$$

Where N denotes normal, S denotes shear, k is spring stiffness, Δt is the time step, $\dot{u}$ is the velocity and F is the spring force.

In XSite, fracture propagation occurs as a combination of intact-rock failure in tension, and slip and opening of joints. The pre-existing joints is a user specified parameter and can be applied within the lattice at preferred locations and orientations. Fluid injection is simulated in the HF simulator (Damjanac *et al.*, 2013). The fluid flow model and hydro-mechanical coupling are suitable for simulation of hydraulic fracturing. The fluid flow occurs through the network of pipes that connect fluid elements, located at the centers of either broken springs or springs that represent pre-existing joints (Damjanac *et al.*, 2016).

The breaking of the springs in tension when the tensile limit is reached (i.e. if the force exceeds the calibrated strength) represents crack formation (Damjanac *et al.*, 2016). This implies that the spring tensile limit is the representative of the rock strength. The broken springs represent the microcracks with fluid nodes forming at points where the spring breaks. The microcracks are connected by fluid pipes to represent hydraulic fractures, as indicated in Figure 2.12. New fluid nodes are created where the spring breaks and there is continuous update of fluid network following each spring break.

2.1.4.3 Flow in Particles

In XSite, the flow through the particles occurs through the network of pipes that connects the fluid elements (fluid nodes) located between the particles. In 3D, the fluid elements are either located

at the centers of either broken springs or at position where the springs intersect the surfaces of pre-existing joints (Figure 2.12a). The pipes are formed between the fluid element (i.e. location of the broken springs) which are at a certain distance to each other. This critical distance is a function of the average particle resolution.

In Xsite, the flow rate q along fractures is calculated with the lubrication equation as given in equation 2.12 (Damjanac *et al.*, 2020).

$$\mathrm{q} = \beta k_r \frac{a^3}{12\mu}\left[p^A - p^B + \rho_w g\left(z^A - z^B\right)\right] \tag{2.12}$$

Where a is the hydraulic aperture, μ is viscosity of the fluid, p^A and p^B are the fluid pressures at nodes A and B respectively, and z^A and z^B are elevations of nodes A and B respectively, ρ_w is fluid density, k_r is the relative permeability and β is a dimensionless calibrated parameter.

$$\mathrm{k_r} = \mathrm{s}^2\left(3 - 2s\right) \tag{2.13}$$

Where s is saturation, and $s = 1$ when the pipe is saturated.

Pressure increment, $\Delta\mathrm{P}$ during the flow time step, $\Delta\mathrm{t_f}$ is given as (Damjanac *et al.*, 2020):

$$\Delta\mathrm{P} = \frac{\mathrm{Q} - \Delta\mathrm{V}}{\mathrm{V}}\mathrm{K_f}\Delta\mathrm{t_f} \tag{2.14}$$

Where, $\mathrm{K_f}$ is the fluid bulk modulus, V is the fluid element volume, $\Delta\mathrm{V}$ is the fluid element volume change due to mechanical deformation and $Q = \sum_i qi$ is the sum of all flow rates qi from the pipes connected to the fluid elements.

2.1.4.4 Hydro-Mechanical Coupling

Coupling of mechanical process and fluid flow in the model is required in HF simulation. The rock compressibility and a stable time step contributes to the hydro-mechanical coupling of hydraulic simulation in X-site (Djabelkhir, 2020). The fluid bulk modulus property is related to the compressibility of the hydraulic fluid and the stiffness of the lattice model. This parameter is based upon the initial fracture aperture and deformation of the model. Another parameter of hydro-mechanical coupling implemented is the fracture permeability. The fracture permeability is controlled by the pre-existing joint and the microcracks formed as the model deforms. The fluid pressure also affects the strength and the deformation of the model (Damjanac *et al.*, 2016; Djabelkhir, 2020).

2.1.4.5 Description of Rock Properties

The modeling of the hydraulic fracturing to obtained a predictive model for breakdown pressure required the used of some mechanical properties of the rockmass which are mainly the uniaxial compressive strength (UCS), tensile strength (σ_t), density, Poison's ratio, Young Modulus, porosity, permeability and fracture toughness. The UCS is the load per unit area at which an unconfined cylindrical specimen of rock will fail under compression test (ASTM D653-14, 2014). Tensile strength is the load per unit area at which an unconfined cylindrical specimen will fail in a simple tension (pull) test (ASTM D653-14, 2014). Rock density, a very important parameter for estimating the overburden stress, is a measure of the mass of rock contained in a given unit volume. Young's Modulus is the ratio of the increase in stress on a test specimen to the resulting increase in strain under constant transverse stress limited to materials having a linear stress-strain relationship over the range of loading (ASTM D653-14, 2014). A rock with high Young's Modulus

is less deformable and vice versa. For hydraulic fracturing, Young modulus can be given as the amount of pressure needed to deform the rock (Zhang, 2019b). Poisson's ratio measures the ratio between linear strain changes perpendicular to and in the direction of a given uniaxial stress change (ASTM D653-14, 2014). Fracture toughness expresses the resistance of a rock to resist propagation (Ouchterlony, 1990). The permeability measure the ability of a porous medium to conduct fluid flow (Zhang, 2019b). Low Poisson's ratio implies rock fracture easily and vice versa (Belyadi *et al.*, 2019). The principal stresses σ_1 (major), σ_2 (intermediate) and σ_3 (minor) within the rockmass were estimated from the stress relationship given by Yong and Maloney (2015).

2.2 Fluid Flow Through Rock Fractures

The second part of this research consists of quantifying airflow through a fracture system using a 3D physical model of a rockmass at the laboratory scale. Section 2.2.1 presents a review of the secondary permeability (or fracture permeability), including previous numerical and experimental flow investigations, and a review of existing models for flow characterization. Section 2.2.2 presents a description of Discrete Fracture Networks (DFN) modeling that can be used to reliably represent fracture systems in three dimensions.

2.2.1 Secondary Permeability and Fluid Flow Formulation

In the evaluation of fluid flow through fractured media, porosity and permeability of the rockmass are essential properties for many applications, e.g. oil extraction, geothermal energy extraction, nuclear waste management, mining, etc. (Öhman, 2005; Singh *et al.*, 2014). In hard rocks, fluid flow is highly sensitive to the aperture of fractures and their connectivity, as fractures are the preferential flow paths within the rockmass (Blyth and Freitas, 2017; Berre *et al.*, 2019). While porosity is the ratio of volume of voids to the total volume of the rockmass, permeability is the

measure of the flow through a porous sample (Blyth and Freitas, 2017). Rockmass permeability is the sum of both the matrix (or primary) permeability and the fracture (or secondary) permeability. Table 2.1 shows the magnitude of primary and secondary permeability for rocks. The intergranular (matrix) porosity of most rock materials is low, with the exception of recemented sandstone or rocks comprising a significant proportion of sandstone sized clasts (Singhal and Gupta, 2010). The secondary permeability of a rockmass is that formed through fracturing processes following the formation of the rock. Additional fractures can be developed in rockmasses through blasting, stress redistribution after excavation, or through hydraulic fracturing as a result of pressurization of the openings created within the rockmass (Öhman, 2005; Silva *et al.*, 2019), and other than for the sandstone exceptions, this creates porosity. Generally, for dense and unfractured rocks, the permeability is very low. The presence of fractures can increase the permeability by several orders of magnitude (Singhal and Gupta, 2010). In heterogeneous fractured rock, permeability depends on fracture intensity, aperture and connectivity (Öhman, 2005; Blyth and Freitas, 2017; Xu *et al.*, 2021).

Table 2.1 Typical values of primary (a) and secondary (b) hydraulic conductivity from laboratory and field tests (Hudson and Harrison, 1997)

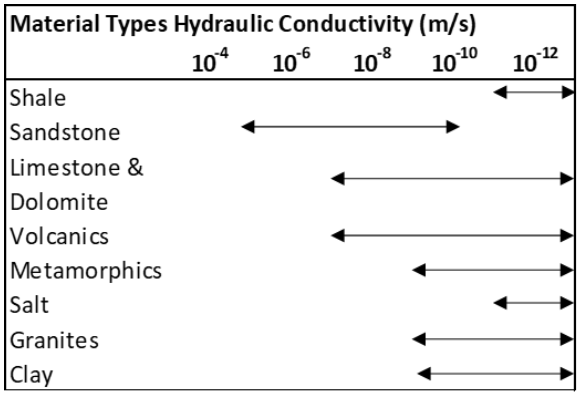

(a)

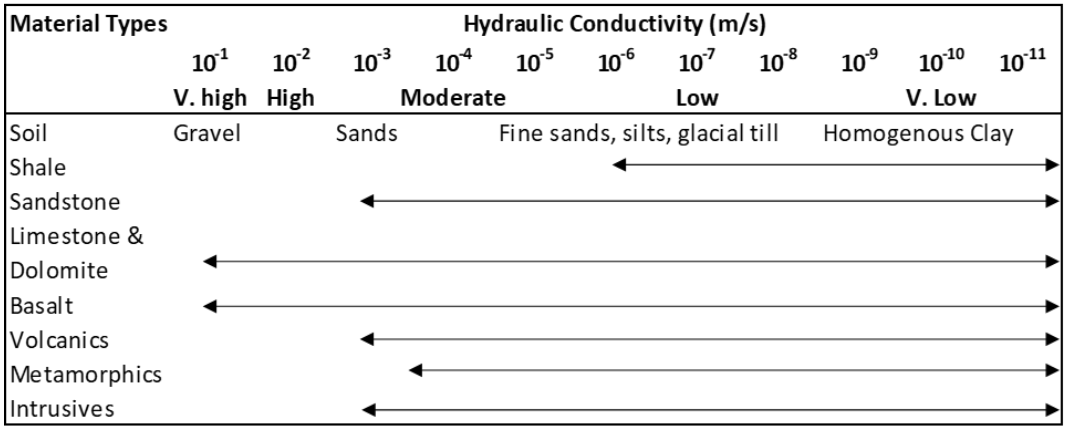

(b)

In general, fractures represent a small fraction of the total volume of a rockmass. However, fracture networks play a decisive role in conducting fluid through rockmass, particularly in hard rocks (Xu *et al.*, 2021). Discrete Fracture Networks (DFN) are 3D representations of fracture systems based upon field observations of the size, orientation and intensity of fractures and can be used to statistically represent a rockmass fracture system (Rogers *et al.*, 2009).

Numerous investigations of fluid flow using Discrete Fracture Networks (DFN) and numerical modeling methods have been conducted by several authors (Nordqvist *et al.*, 1992; Sarkar *et al.*, 2004; Öhman, 2005; Baghbanan and Jing, 2007; Klimczak *et al.*, 2010; Li *et al.*, 2020). Nordqvist

et al. (1992) and Öhman (2005) have studied flow and transport in fracture networks. The impact of three-dimensional variable apertures was investigated by Nordqvist *et al* (1992), while Öhman (2005) provided an enhanced upscaling method to estimate equivalent properties of flow with DFN modeling. Sarkar *et al.* (2004) investigated, using computational fluid dynamics (CFD) modeling, fluid flow in series and parallel combinations of fractures, as well as flow in inclined, intersecting fractures and mixed networks. Baghbanan and Jing (2007) and Klimczak *et al.* (2010) investigated the permeability of fractured rocks by simulating flow through numerous 2D stochastic DFNs and demonstrated that, for models with correlated aperture and trace length, the presence of large fractures with wider aperture are dominant factors controlling the overall permeability. Li *et al.* (2020) established that the surface roughness and fracture apertures are both influential factors to the flow behavior in intersecting fractures.

There are fewer laboratory experiments regarding fluid flow through fractures than numerical simulations. Chen *et al.* (2000) conducted a laboratory experiment on the permeability of granite samples and demonstrated that, due to tortuosity and surface roughness, the hydraulic aperture, which is an equivalent aperture that conducts fluid flow, was found to be less than the mechanical aperture, which is a measure of void spaces existing between two fracture surfaces. Due to specimen size limitations, other previous experimental work investigating fluid flow through fractures performed at the lab-scale have considered mainly one fracture (Singh *et al*., 2014; Zhang *et al*., 2019; Kulatilake *et al*., 2020; Cardona *et al*., 2021). However, these previous lab-scale experiments cannot capture the influence of fracture intensity and connectivity on fluid flow through a fracture network.

In a laboratory experimental work, Zhang *et al.*, (2019) investigated the non-linear flow behavior for various Reynolds number under different joint roughness coefficient (JRC) and observed a nonlinear flow behavior between hydraulic gradient and average velocity. Chen *et al.* (2000) also investigated the hydraulic behavior of a granite rock and established that shear dilation influences the permeability of the fracture even at higher normal stresses.

Darcy's law, which governs fluid flow through porous media, and also known as the 'cubic law' due to the dependence of transmissivity on the cubic of the aperture, provides a simple relationship between the hydraulic aperture of a fracture and its permeability (Sarkar *et al.*, 2004; Ranjith and Viete, 2011). This has been presented in various forms by some researchers as summarized in table 2.2.

Table 2.2 Different forms of Darcy law/Cubic law

Equation	Terminology	Reference
$Q = -\frac{kA}{\mu}\left(\frac{P_o - P_i}{l}\right)$	Q= total volumetric flux, A=Wh = cross-sectional area, $k = \frac{h^2}{12}$ is the permeability of the fracture, h=hydraulic aperture, W=width of the fracture, μ = dynamic viscosity of the fluid, P_o and P_i are the outlet and inlet pressure and l is the length of the fracture. The negative sign indicates flow is opposite to the direction of increasing gradient.	(Sarkar *et al.*, 2004; Atangana, 2018)
$Q = \frac{\rho g W e^3}{12\mu l}(\Delta h)$	Q = total discharge (m^3/s), ρ = density of fluid (Kg/m^3), g= acceleration due to gravity (m/s^2), W= width of the fracture normal to flow path, e = fracture aperture (m), Δh = difference in hydraulic heads over fracture length (m), μ = dynamic viscosity of fluid (Kg/m.s) and l = fracture length (m)	(Singh *et al.*, 2014)

$Q = C(2b)^3 \times \Delta h$ $C = \left(\frac{2\pi}{\ln\left(r_e / r_w \right)} \right)\left(\frac{\rho g}{12\mu} \right)$ for radius flow $C = \left(\frac{W}{L} \right)\left(\frac{\rho g}{12\mu} \right)$, for straight flow	b = fracture aperture, Δh = drop in hydraulic heads, r_e and r_w are outer and wellbore radius respectively, ρ = density of fluid, g = acceleration due to gravity, W= width of the fracture, L = fracture length (m), μ = dynamic viscosity	(Witherspoon *et al.*, 1980)
$Q = \frac{kA}{u} * \frac{\Delta P}{L}$ $k = \frac{e_h^2}{12}$ $e_h = \left(\frac{12uQL}{d\Delta P} \right)^{\frac{1}{3}}$	Q = the flow rate through the sample, k = permeability of the sample, A = cross-section flow area of the sample, ΔP = pressure drop through the sample, L = length of the sample, μ = fluid viscosity, e_h = hydraulic aperture of fracture, d = fracture length orthogonal to no-flow boundary	(Chen *et al.*, 2000)
$Q = \frac{nw^3}{12u}\left(\frac{\Delta P}{L} \right)$	n = the number of fractures, w = the fracture width, e = the fracture aperture, μ = the dynamic viscosity of the fluid, ΔP = the pressure drop through the sample and L = the sample length	(Tiab, D. and Donaldson, 2015)

The simplest model of fluid flow through a rock fracture is the parallel plate model, well-known as ‘cubic law’, which assumes that the fracture walls can be represented by two smooth, parallel plates, separated by an aperture. Using this model, an exact calculation of the flow or permeability is possible. Tiab and Donaldson (2015) present an equation for volumetric flow rate (Table 2.2) as a basic approach for estimating fracture permeability in a block of naturally fractured rock with n fractures. This equation assumes rectangular and smooth fractures that do not contain any mineral.

2.2.2 Discrete Fracture Network (DFN)

A DFN, as defined by Lei *et al.* (2017), refers to the generation of fractures by computational model that explicitly represents the geometrical properties of individual fractures and the topological relationships between fractures and fracture sets. DFN modeling can be used to represent the natural fractures (including their orientation, size, position, shape, connectivity, etc.) in a rockmass. Thus, a DFN maps the location of discontinuities within a rockmass (Junkin *et al.*, 2018).

Discontinuous rockmass are composed of discontinuities such as fractures (joints), bedding planes, shear zones, faults, etc. and these discontinuities are essential in engineering applications. These natural occurring discontinuities are present in the rockmass as a complex network which presents inevitable influence on the mechanical and hydrological behavior of the in-situ rockmass. DFNs can be used to characterize the discontinuities within a rockmass (Lei *et al.*, 2017; Xin and Cai, 2020) by mapping and obtaining field data representative of the natural existing discontinuities or by stochastic realization to represent rock fracture network or structures such as fault, bedding planes, etc. (Lei *et al.*, 2017). DFN modeling also provides statistical representation of the rockmass fracture system which is established on the observed fractures properties. Despite some variations between the different DFN generators, the basic input data are related to the distributional form of primary characteristics of the fractures, and include fracture shape, fracture size distribution, fracture orientation, and fracture intensity (Table 2.3) for each set of fractures (Valerio *et al.*, 2020). Rogers *et al.*, (2009) presented the different measures of fracture intensity. The different dimensions of the sampling region according to the dimension of the feature are shown in Table 2.2.

Table 2.3 Quantification of fracture parameters (modified after Rogers *et al.*, 2009)

		Measurement Dimension				
		0	1	2	3	
Dimension of sample region	1	P10 ($Length^{-1}$) No. of fractures per unit length of a scanline (Linear intensity)	P10 ($Length^{0}$) Length of fractures per unit length of a scanline			Linear Measure
	2	P20 ($Length^{-2}$) No. of fractures per unit area	P21 ($Length^{-1}$) Length of fractures traces per unit area sampling plane	P22 ($Length^{0}$) Area of fractures per unit area of sampling plane		Areal Measure
	3	P30 ($Length^{-3}$) No. of fractures per unit volume of rockmass		P32 ($Length^{-1}$) Area of fractures per unit volume of rockmass	P33 ($Length^{0}$) Area of fractures per unit volume of rockmass	Volumetric Measure
Term		Volumetric density		Volumetric intensity	Porosity	

Esmaieli *et al.*, (2010) suggested that the geometrical representative elementary volume (REV) can be determined based on P32, the fracture area per rock volume. Variations in the calculated P32 decrease as the sample size increases, which demonstrated the importance of establishing the REV.

There are several applications for DFN models. These includes ground water modeling, radioactive waste disposal site selection, stability analysis of wedge and blocks, application in engineering design such as mine design, geothermal enhancement, oil and gas production and also modeling of jointed rocks in synthetic rockmass modeling (Ivars *et al.*, 2011; Lei, 2020; Valerio *et al.*, 2020; Xin and Cai, 2020).

The research results for the two main topics of the thesis are presented in chapters 3 and 4. In chapter 3, the numerical predictive model for the breakdown pressure is presented and the results

are compared with the data collected during a HP field experiment. In chapter 4, the lab-scale evaluation of the secondary permeability represented in a DFN model is described.

Chapter 3

3 Numerical Modeling of the Breakdown Pressure from a Hydraulic Preconditioning Field Experiment in a Deep Northern Ontario Mine

3.1 Introduction

Maloney and Gonzalez (2017) provides information about the field experiment conducted by MIRARCO Mining Innovation in a northern Ontario mine.

In this research, a numerical model was developed to represent the results of the field experiment. The model simulates the breakdown pressure achievement and is calibrated by using the field experiment data (fluid injection pressure, in-situ stresses and rockmass properties among others) and comparing the results obtained. The simulation is focused on the breakdown pressure recorded during the field experiment in a vertical borehole at a depth of about 1350 m performed to reopen a natural discontinuity.

3.2 Field Experiment

The hydraulic preconditioning field experiment was conducted in an underground mine in northern Ontario by MIRARCO's Geomechanics Research Centre at Laurentian University (Maloney and Gonzalez, 2017). The field experiment was an underground trial with equipment developed at the Geomechanics Research Centre, MIRARCO. The trial was performed in a geotechnical context with high in-situ stress conditions in strong rock at a depth of ~ 1350 m. The borehole was NQ-sized (76 mm diameter). A vertical borehole, with a length of 30 m was drilled from the 1350 m deep level. The borehole was logged and televiewer scans (acoustic and optical) were performed before and after the injections to establish the characteristics of the borehole before and after the

HF experiment. The equipment consists of two inflatable rubber packer elements straddled by an interval spacer. The packer elements are used to seal off a segment of the hole to avoid leak-off pressures during hydraulic pressurization. The fracture interval (Figure 3.1) is of 750 mm and the packer effective length is of 400 mm, thus the injection zone results in 350 mm.

The fluid injected was supplied by two modules which provided fluid independently to packers and to injection points. The pressure applied was registered by both manometers to packers and injection points, respectively. Simultaneously, the pressures and the water flow rate were recorded by a data logger in real time. The fluid was then pumped into the hole with a constant flow rate. During the HP test, the pressure increases in the hole linearly, as long as there is no leak in the system, and the rock matrix is not highly permeable.

Figure 3.2 and 3.3 present the results for the HP test conducted in a vertical borehole at the borehole depth of $24.7\,\mathrm{m}$ with respect to the collar of the borehole. At that location a pre-existing natural discontinuity was identified and fluid pressure applied at the isolated section for opening of the pre-existing natural discontinuity. The pressure applied in packers is represented in blue color and the injection pressure applied directly in the rockmass is represented in orange color. The injection volume of water is shown in grey color in Figure 3.2a. The optical and acoustic images are compared before and after the injection test (Figure 3.2b). The two green bands suggest the approximate border location for the packers. The acoustic images show the more damaged pre-existing fracture after treatment (indicated by the red ellipse).

Figure 3.3 shows result of the pressure-time curve with the breakdown (P_b), reopening (P_r) and closure (P_c) pressures which was recorded during the HF test. Table 3.1 provides the orientation of the pre-existing natural fracture within the injection zone of the borehole.

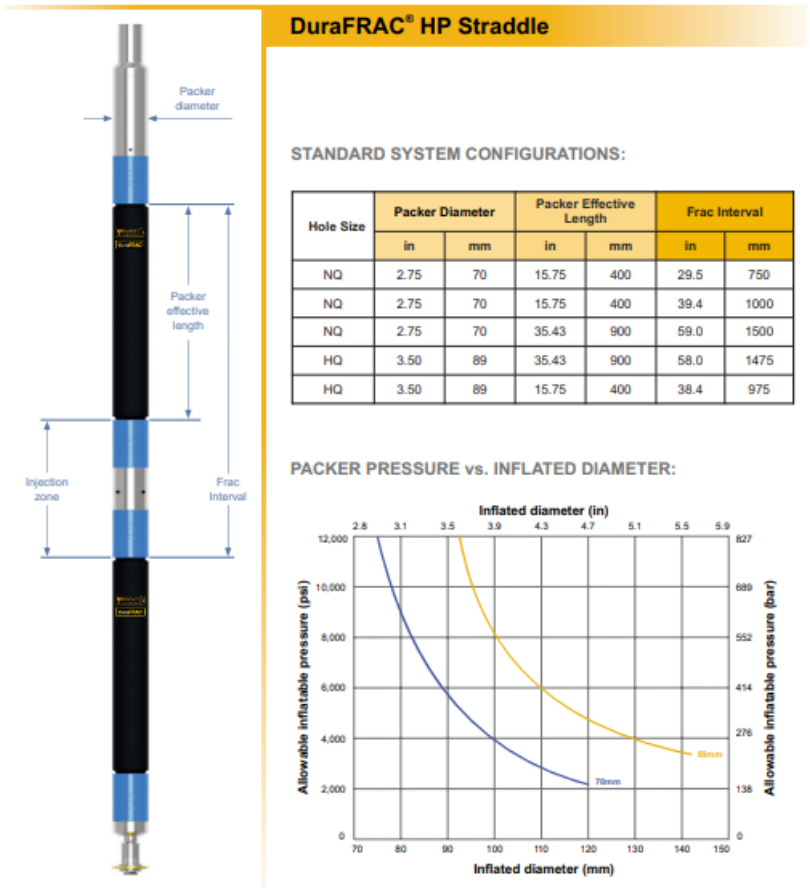

Hole Size	Packer Diameter		Packer Effective Length		Frac Interval	
	in	mm	in	mm	in	mm
NQ	2.75	70	15.75	400	29.5	750
NQ	2.75	70	15.75	400	39.4	1000
NQ	2.75	70	35.43	900	59.0	1500
HQ	3.50	89	35.43	900	58.0	1475
HQ	3.50	89	15.75	400	38.4	975

Figure 3.1 Straddle packer system (IPI, 2022)

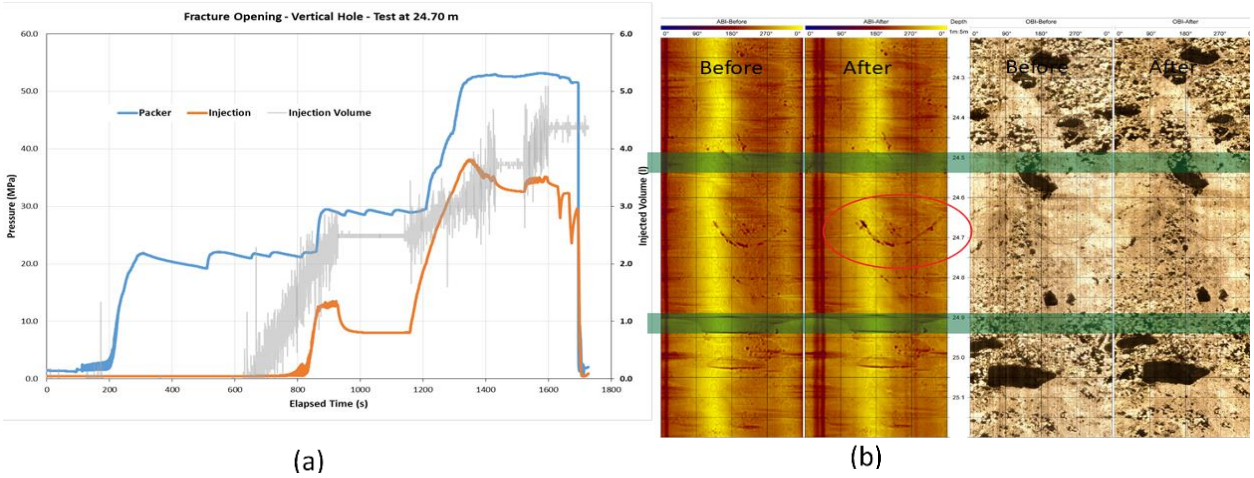

Figure 3.2 (a) HP Test result in vertical hole to open a natural discontinuity at 24.7 m depth and (b) Optical and acoustic televiewer images obtained before and after the test (Maloney and Gonzalez, 2017).

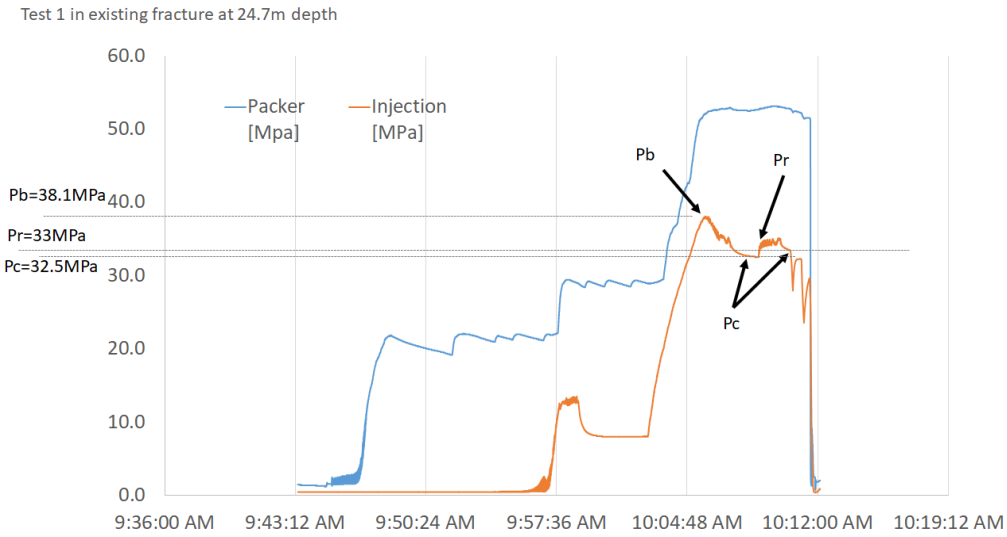

Figure 3.3 Interval pressure vs. time to injection and packers, at 24.7 m depth (Maloney and Gonzalez, 2017).

Table 3.1 Natural discontinuity at 24.7m depth dip and azimuth angles

Dip (degrees)	Dip Direction (degrees)
46	49

The available data collected during the field HP experiment conducted and published by MIRARCO Mining Innovation (Maloney and Gonzalez, 2017) were used in this research to setup the numerical model in the Xsite software. Section 3.3 presents the numerical model developed in this work.

3.3 Numerical Model Setup

The Xsite software is based on the Synthetic Rockmass (SRM) and lattice method described in Sections 2.1.4.1 and 2.1.4.2. This section presents the main steps for numerical model setup in Xsite consisting of the main rock properties, model resolution, structural features, hydraulic

fracturing parameters and simulation history, as described in Sections 3.3.1 to 3.3.6. Further details of the software is found in the user's guide (Itasca, 2013). Figure 3.4 presents the model setup and Table 3.2 provides the rock properties and input parameters used. The rock properties were obtained from typical properties of rock present at the mine site where the lithology is mostly Norite.

3.3.1 Main Rock Properties

The set of rock properties were calibrated from ranges of values estimated for the host rock in which the field test took place. Related to the initial conditions: it is assumed there is no water in the rockmass, the experiment and the simulation were performed in dry initial conditions. The in-situ stresses can be estimated to represent the type of fault regime occurring at the region of interest within the rockmass.

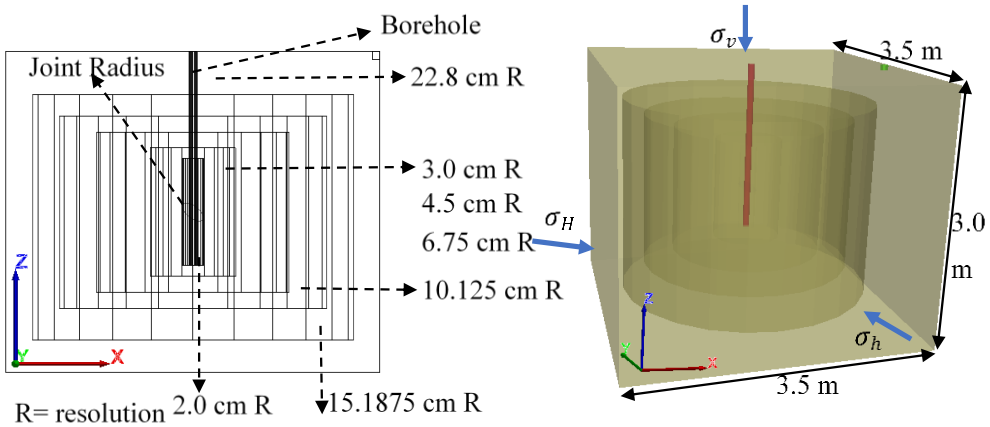

Figure 3.4 A representation of the numerical model setup for numerical simulation

Table 3.2 Mechanical properties and modeling parameters

Rock and Model Properties		Unit	Parameters
Density	ρ	kg/m3	2957
Young Modulus	E	GPa	64
Uniaxial Compressive Strength	UCS	MPa	51
Poisson's Ratio	v		0.25
Tensile Strength	σ_t	MPa	5
Fracture Toughness	K_{IC}	Mpa.m^0.5	2.9
Porosity	ϕ	%	2

In this study, the model represents the reverse faulting scenario. This is representative of the faulting regime within the Canadian Shield at a depth of the experiment ~ 1350m. The stress tensor was obtained based on the work of Yong and Maloney (2015) and is presented in Table 3.3.

Table 3.3 Initial conditions, natural stresses estimation

Stress component		Magnitude (MPa)	Dip Angle (º)	Dip Direction (º)
Maximum Horizontal Stress	σ_H	60.3	0	90
Minimum Horizontal Stress	σ_h	48.2	0	0
Vertical Stress	σ_v	39.8	90	0

3.3.2 Model Resolution

Using Xsite, different resolution levels can be defined within the model. The model resolution is the average lattice node spacing. A variable resolution was defined around the borehole, with higher resolution in the vicinity of the borehole and progressively lower resolution as the distance from the borehole increases. This ensure finer lattice nodes are specified around the borehole to provide a higher accuracy for the model results. This higher resolution at the borehole scale is necessary to adequately capture the magnitude of breakdown pressure. The simulation time is approximately proportional to the resolution. Hence, using a variable resolution, the simulation time can be reduced and optimized (as opposed to using a uniform resolution). The variable

resolutions of 2.0 cm, 3.0 cm, 4.5 cm, 6.75 cm, 10.125 cm and 15.1875 cm, as illustrated on Figure 3.4, were used to reduce the simulation processing time. The remaining part of the model resolution was set to 22.8 cm.

3.3.3 Structural Features

The pre-existing joint is defined as a structural feature. The joint is represented at the location of interest within the model geometry. The orientation of the joint can be specified as well as the joint properties in the numerical model. The joint surface can be represented from very weak, to strong according to rock mass characterization criteria or user-defined joint properties can be selected to suit the model application. In this model a medium weak surface joint was assumed to represent the pre-existing joint with dip of 46 degrees and dip direction 49 degrees. A non-zero gap is required to define a joint. A very small value of $2.1\times10^{-4}\,\mathrm{m}$ was assumed to define the joint. In this case, the joint represents the defect in the borehole wall which can be reactivated by the fluid pressure, thus providing a point for fracture initiation

3.3.4 Hydraulic Fracturing Parameters

The HF parameters assumed from the actual field experiment are shown in Table 3.4

Table 3.4 Hydraulic fracturing parameters

Injection Rate	Q	m^3/s	0.0143
Borehole Radius	r	m	0.038

The well trajectory is an input tool from the code and allows the definition of the position, orientation, radius and depth of the borehole. Under the hydraulic fracturing parameters, the well trajectory is used to define the borehole geometry and the simulation stages, the fluid injection cluster segments and the boundary conditions such as the fluid injection rate. The open borehole

option is used to simulate the borehole breakdown pressure. The vertical borehole is located at the center of the 3D model, as illustrated on Figure 3.4. The simulation sequence is used to specify simulation in batches. The numerical model was run for 0.4 seconds at injection rate of 0.0143 m^3/s.

3.3.5 Simulation History

Simulation history records selected variables such as the cluster pressure (borehole pressure), flowrate, etc. which can be specified before initiating the model and the record can be exported. The cluster pressure, which is the pressure recorded at the point of injection during the HF is the important parameter for this analysis since its represent the rock mass behavior against the injection pressure it is receiving from the HP. This parameter can be added as simulation history, a software tool that records all selected variables during the simulation, and can be exported and graphically compared with the field experimental result.

3.3.6 Numerical Modeling Steps

The main steps in the numerical modeling process are:

1) Formation of the SRM (geometry of the model);
2) Initial conditions: input of the stress conditions; and water if it is present in underground;
3) Input of the geotechnical properties;
4) Input of the hydraulic preconditioning parameters: injection fluid properties and injection parameters of the borehole;
5) Initial state: The model run in the mechanical mode to build model equilibrium;

6) Hydro-mechanical coupling where fluid injection is applied and the required histories are established (e.g. cluster pressure, fluid pressure, flow rate, etc.).

Flow rate and viscosity are key parameters in HF. The experimental work by Cheng *et al.*, (2021) identifies a linear relationship between flow rate and pressure and established that fracture initiation and breakdown depend on the flow rate introduced into the rock formation. For the numerical simulation, the injection rate was estimated from the borehole pressure and the volume of water pumped during the field experiment, as shown on Figure 3.5. Firstly, the time taken to achieve the breakdown pressure is estimated from the pressure-time curve. Then, the total volume of water pumped until the breakdown pressure is reached was also estimated from the volume-time graph in Figure 3.5. The estimated injection rate was calculated by dividing the total volume of water injected (i.e. 2,869.1 liters) by the time taken to reach breakdown pressure which was about 200 seconds. This gives an injecting rate of 14.35 l/s (0.01435 m^3/s).

The viscosity of the injection fluid adopted in the simulation was obtained from equation 3.1. This was a numerical strategy used to increase the injection energy which also decreases the computation time for the simulation. Additionally, adopting the real field injection rate at lower viscosity exaggerates the numerical injection rate in the simulation. Using a higher viscosity, enabled a lower injection rate to be used for the numerical simulation while ensuring enough fracturing energy for fracture propagation. Material properties such as fluid viscosity, fracture toughness and Young modulus were previously scaled to establish the input for the numerical simulation. The scaling of these properties also controls the fracturing mechanisms and reduces the boundary effect in the numerical modeling. Equations 3.2 and 3.3 are used to scale these material properties for the numerical modeling (Dontsov and Zhang, 2018).

$$\mu' = 12\mu \tag{3.1}$$

$$\mathrm{K}' = \left(\frac{32}{\pi}\right)^{\frac{1}{2}} K_{IC} \tag{3.2}$$

$$E' = \frac{E}{1-\nu^2} \tag{3.3}$$

μ is the fracturing fluid viscosity, K_{IC} is the mode I fracture toughness of the rock, E is the Young modulus, ν is the Poisson's ratio, μ', K' and E' are the scaled parameters for fracturing viscosity, fracture toughness and Young Modulus respectively.

The model is built and run in a mechanical mode, to excavate the borehole and to set the model to equilibrium. It is then followed by the hydro-mechanical mode over the indicated modeling time of about 0.030 seconds.

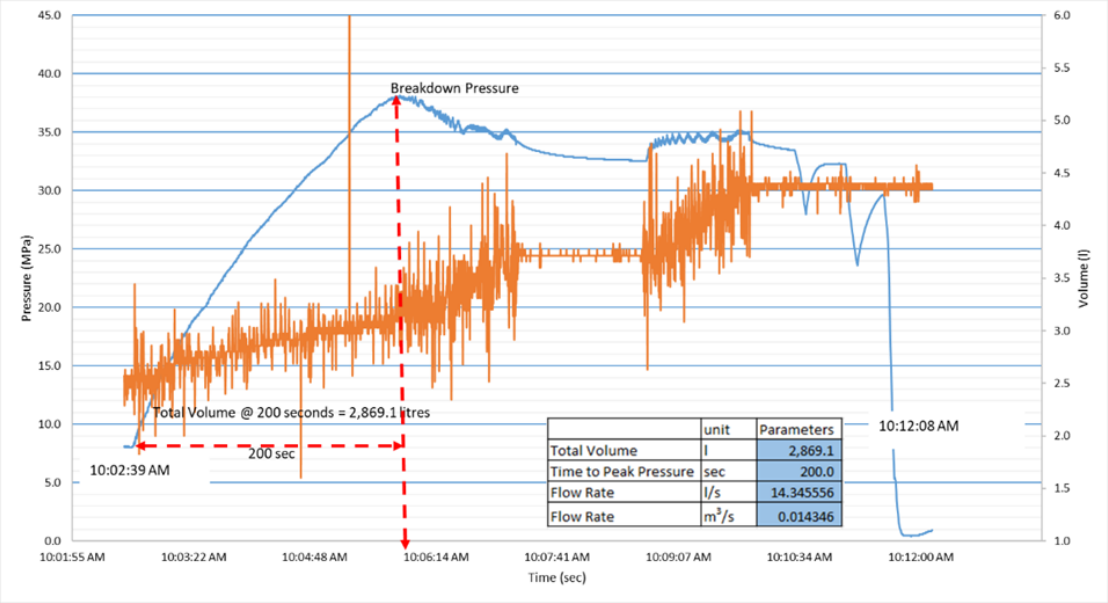

Figure 3.5. Borehole pressure curve and pumping result from the hydraulic preconditioning field experiment

3.4 Results and Discussion

The numerical simulation was performed to determine the breakdown pressure needed to open a pre-existing natural discontinuity into the rockmass via water injection in a preconditioning HF at the depth of more than 1300 m and to reproduce numerically a field experiment carried out in Northern Ontario. Figure 3.6 presents the results obtained from the numerical simulation, compared with the results from the field experiment. The stress level for the numerical simulation was the same as estimated for the rockmass field stress, establishing a similar stress condition in the synthetic rockmass as in the field case.

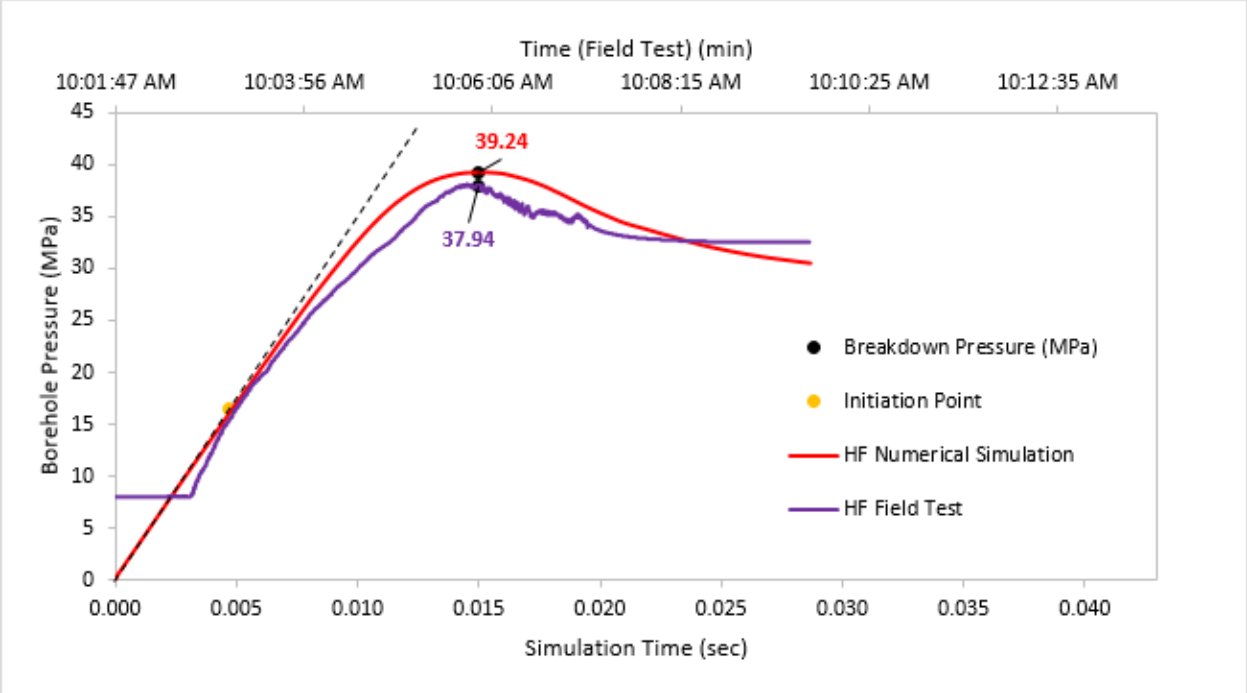

Figure 3.6 Numerical and field experiment results for borehole pressure during hydraulic fracturing

As the pressure increases to a pressure of 16.5 MPa the rate of pressure increase changes in a way that the pressure-time curve departs from linearity as fracture initiation occurs (Zang and Stephansson, 2009). After linearity, pressure is typically seen to increase at a lower rate until a

maximum pressure is reached, and this pressure is called breakdown pressure (p_b). This behavior agrees with the literature descriptions (see Figure 2.2 in Section 2.1.3). After this point, the pressure falls rapidly until a level where it remains steady.

From the numerical modeling results, the pressure required to reopen the pre-existing joint in the SRM is about 39 MPa (Figure 3.6). This result agrees well with the breakdown pressure of about 37 MPa observed from the results of the field experiment.

The numerical approach of Xsite code to simulate cracks and finally fracture creation is: when the tensile strength of the spring is reached, it breaks and, as the hydro-mechanical coupling process continues, a number of springs break to form well-defined microcracks as many individual springs reach the tensile limit of the rock. This process resulted in the formation of a transverse fracture plane representing a reverse faulting stress regime as expected in the Canadian Shield. Figure 3.7 shows the micro-cracks formed during the numerical simulation with the general transverse fracture plane.

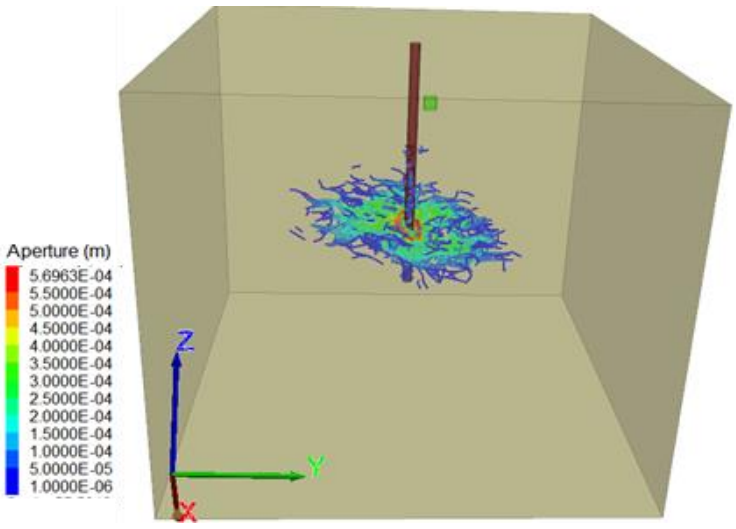

Figure 3.7 Crack formation in numerical simulation

The synthetic rockmass given in Figure 3.4 shows uniform properties throughout, with a pre-existing fracture set at the injection point to provide a seed point for crack initiation in Xsite. The agreement between the results from the field experiment and the results from the numerical simulation indicates that the set of parameters used for modeling is well calibrated and it is able to provide a reliable representation of the field experimental test. The breakdown pressure obtained for the simulation is found to match that of the field test. Not only the shape of the curves is similar, but the order of magnitude too, with a difference of 3.4%, which represent an acceptable approximation of the field breakdown pressure.

One of the limitations of this work was that the size of the numerical model had to be reduced due to very long computational time and lack of memory of the modeling computer used. Hence, due to the very large number of nodes involved, setting up a model to match the length of the injection borehole of 24.7 m was not achievable and the model was reduced to 3.5m long x 3.5m wide x 3.0 m high. The model volume focused on the location of the injection cluster and a stress state representative of the field experiment was used for the numerical simulation. Additionally, the simulation focused on estimating the breakdown pressure because of the difficulties in simulating both breakdown pressure and fracture propagation in a single Xsite model. This is due to the significant difference in scale of the elements involved in the model, namely the injection borehole, the seed fracture, the injection cluster and the rockmass volume, which can vary from several orders of magnitude in scale. To simulate fracture propagation, a second model should be developed in Xsite at the rockmass scale.

3.5 Conclusion

In this work, a numerical model was developed to represent the breakdown pressure from a hydraulic preconditioning field experiment conducted in a Northern Ontario mine. The breakdown pressure estimated with the calibrated numerical model is in good agreement with the results observed from the field experiment. This demonstrates that the developed numerical model is capable of simulating the injection pressure required for reopening a pre-existing joint in a rockmass. Thus, the developed numerical model can serve as a valuable tool for predicting the magnitude of the injection pressure needed for fracture initiation and fracture reopening, and to reach the breakdown pressure of the rock formation. This is very important for hydraulic preconditioning planning and operations.

The developed numerical model can serve as a tool to estimate the amount of fluid pressure needed to stimulate pre-existing fracture initiation without carrying out high-cost HP field experiments. However, it is necessary to reliably characterizing the rockmass, the natural stress distribution and the orientation of the pre-existing discontinuities. However, fracture initiation does not imply that it will grow further. For a fracture to start propagating, the injection pressure must exceed the breakdown pressure. The future work will be to investigate fracture propagation from hydraulic preconditioning, as a subsequent process to fracture initiation.

HP can be used to create additional fractures to increase the fracture intensity and connectivity in a rockmass. This is an alternative to the current NHEET system which consider a volume of rock fragments (as opposed to a fractured rock mass). The alternative system can create a volume of in-situ rock with sufficient fracture intensity and connectivity to admit enough flow, thus optimizing heat transfer and reducing the footprint at surface.

Chapter 4

4 Lab-Scale Verification of the Secondary Permeability Represented in a 3D Printed Discrete Fracture Network (DFN) Model

4.1 Introduction

This chapter first provides a description of a Discrete Fracture Network (DFN) modeling creation with the software MoFRAC to represent a sample of rock mass (rock matrix and joints) for the laboratory experiment. Also, the steps to generate a physical model representing a fractured rockmass via 3D printing technology are detailed. Additionally, the laboratory experimental setup is presented. This lab test is used for fluid flow measurements and is further used to establish the behaviour of the changing pressure to fluid transfer through fracture openings. The results of the laboratory experiment are compared to a basic empirical approach for estimating fracture volumetric flow rate.

4.2 DFN Modeling with MoFRAC

For this study, a numerical DFN model is built using MoFRAC, which is software modeler developed by MIRARCO Mining Innovation (MIRARCO, 2022). A parent DFN (A) of volume 32,674 cm^3 was generated with MoFRAC containing two fracture sets parameters adopted from Esmaieli *et al.* (2010). DFN modeling requires information about the size, orientation and intensity of fractures (Figure 4.1). The fracture intensity P_{32}, which is the area of fractures per unit volume (Rogers *et al.*, 2009), provides input for the volumetric intensity of the two fracture sets generated. The dip and dip direction controls the orientations of the fractures planes. The Fisher K value describes the tightness or dispersion of the fracture distribution from the mean orientation. A larger

K value, implies tighter cluster and a smaller K value implies a more dispersed cluster (Love, 2007) as indicated in Figure 4.2. MoFRAC differentiates fracture set with color base on dip values.

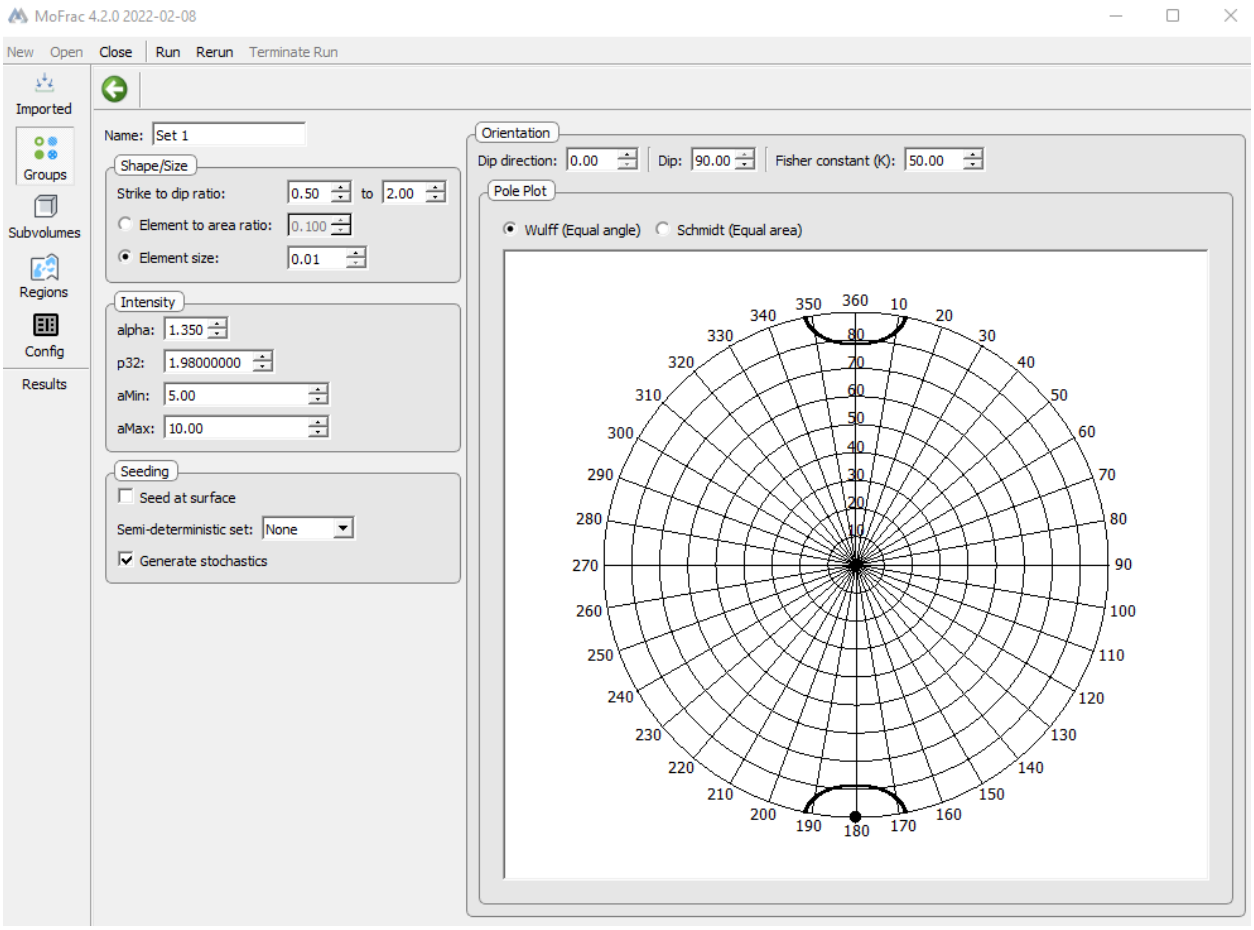

Figure 4.1 MoFRAC interface for defining fracture sets

The minimum and maximum area of fracture planes (aMin and aMax) is an input to represent the fracture size threshold. Alpha is a numerical parameter of the code that represents the negative exponential size distribution. A lower value means larger fractures with respect to small fractures. A higher value results in more small fractures with respect to large fractures. Table 4.1 shows the fracture set properties, and the parameters such as Fisher constant, alpha, aMin and aMax used to generate the DFN model. Details about the software MoFRAC can be obtained from (MIRARCO,

2020a). The numerical DFN sample simulated to represent a rockmass with fractures is shown in Figure 4.3, where the fracture set 1 is colored in blue and the fracture set 2 in orange.

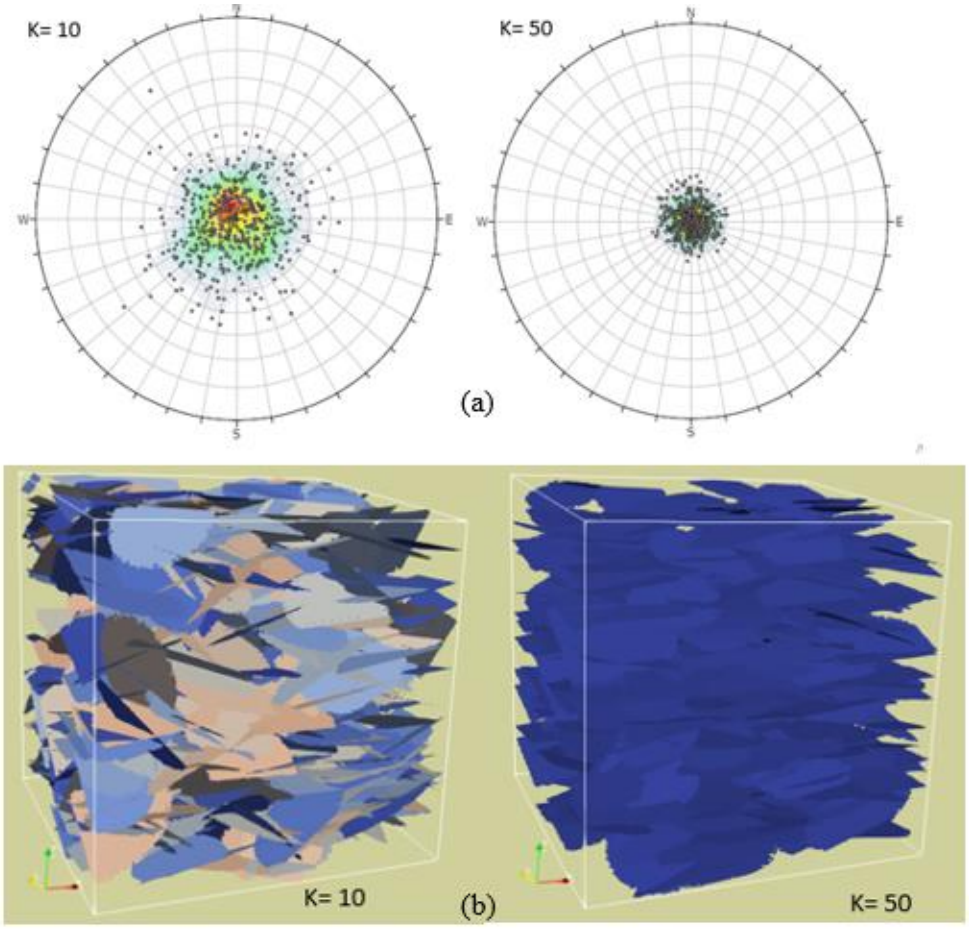

Figure 4.2 (a) Effect of Fisher K on a randomly generated joint set in DIPS (b) effect of Fisher K on a randomly generated fracture set in MoFRAC

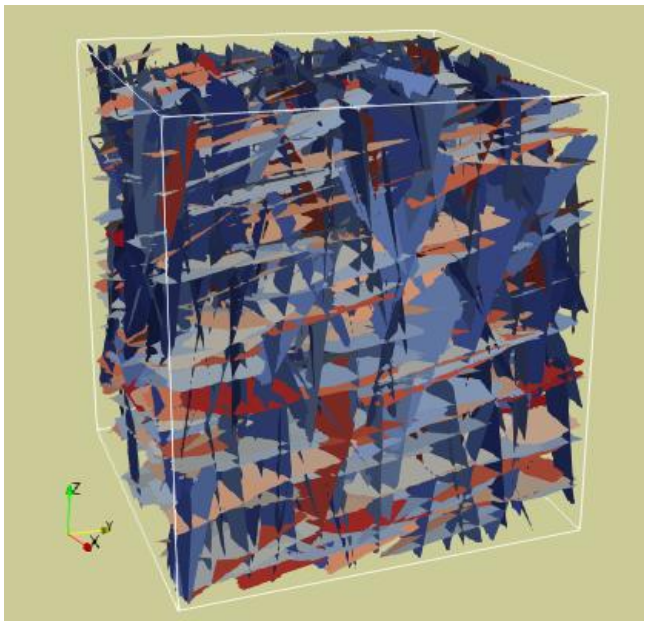

Figure 4.3 3D DFN model generated with MoFRAC (set 1 in blue and set 2 in orange)

Table 4.1 Input parameters for DFN modeling with MoFRAC

Parameter	Set 1	Set 2
Volumetric fracture Intensity, P_{32}	0.98	1.09
Dip Direction (^{o})	7	227
Dip (^{o})	89	17
Fisher K	17	57
Alpha	1.35	1.35
aMin	40	40
aMax	80	80

4.2.1 Representative Elementary Volume (REV)

The DFN volume dimension has an impact on the resulting DFN average properties (fracture orientation, size, intensity, etc.) and there is a minimum volume dimension, i.e. the Representative

Elementary Volume (REV), for which the 'average value' do not vary significantly under repeated testing (Esmaieli *et al.,* 2010). In other words, the REV operates as a scale factor to reliably represent, in a smaller sample, the real scale problem. A REV analysis allowed for determining the minimum size for the 3D printed DFN model used in the experimental setup. This REV ensures that the 3D printed DFN model maintains similar properties as the larger DFN volume modeled with MoFRAC. The REV has to be of reasonable size to contain enough fractures in order to represent the characteristics of the larger volume (Fernandes *et al.,* 2012).

Figure 4.4 shows the three different volumes extracted from the parent volume A and to establish the REV. As given in Figure 4.4, volume B of about 4,084 cm^3, comprising 178 fractures, is a good representation of the parent volume A of 32,674 cm^3 (1255 fractures). Effectively, volume B with P_{32} of 2.04 m^{-1}, shows the least deviation from the input P_{32} value. The experimental setup (Section 4.3.1) requires a DFN of about 1000 cm^3 for the flow experiment, considering the diameter of the flow duct which is about 16.8 cm. Thus, volume B, having 4,084 cm^3 and 178 fractures was practically not possible to fit into the experimental setup.

For practicality during the 3D printing process, four sub-volumes contained within volume B were generated with MoFRAC (Table 4.2) to determine the minimum number of fractures that would ensure a REV. The average dip and dip direction values, as well as the Fisher's constant K and the P_{32} values were calculated for each fracture set and for each simulated DFN volume. Statistical analyses were conducted to determine the minimum DFN volume, which minimizes the variation of the average output model parameters from the input parameters used in MoFRAC to generate the DFN. DIPS (Rocscience, 2022) was used to determine the average dip, dip direction and K values.

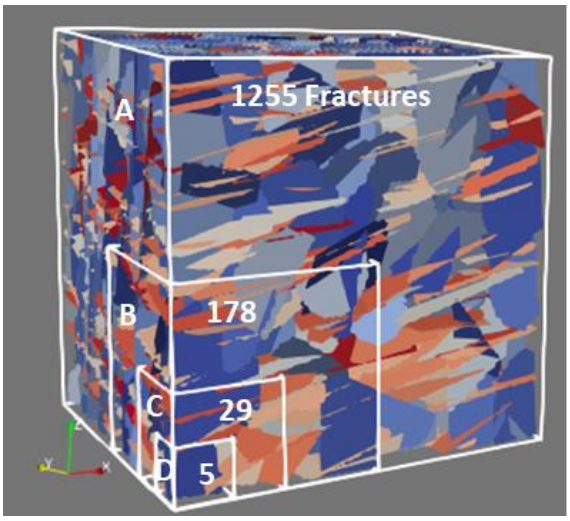

Figure 4.4 DFN model with two fracture sets (set 1 in blue and set 2 in orange) with Representative Elementary Volume (REV) simulations (volumes A, B, C and D)

The selected volume (REV) comprises 58 fractures (Figure 4.5). The selected REV have less significant variation comparing to other volumes, with dimension of 9.76 cm x 9.76 cm x 10.7 and volume of 1,021 cm^3. Figure 4.6 shows the result of the statistical analysis for the estimation of sub-volume of the DFN with volume B to arrive at the REV volume of 58 fractures.

Table 4.2 DFN sub-volumes used in REV analysis

Length (cm)	Volume (cm^3)	No. of Fractures
15.5	4,084	178
12.30	2,042	97
9.76	1,021	58
7.75	511	30

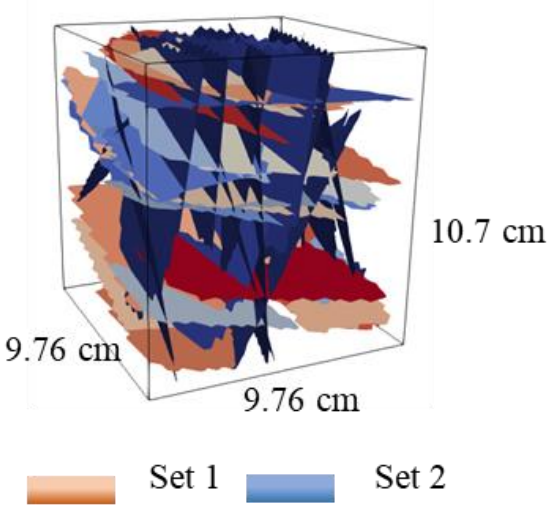

Figure 4.5 Selected REV with 2 fracture sets (58 fractures)

One of the considerations for the lab-scale experiment was to minimize the number of fractures in order to ensure that the internal structure of the physical model can be reliably printed without issues related to the support of the printing material during the process. A second consideration was to ensure that the internal structure is able to withstand the fluid flow pressure used during the lab experiment. These practical limitations further justify the selection of the smaller DFN volume with 58 fractures.

Figure 4.7 shows stereographic projections for the comparison between the orientation (dip and dip direction) of the fractures generated by the DFN model, visualized using DIPS (Figure 4.7b), and the input values used in MoFRAC (Figure 4.7a). As illustrated on Figure 4.7, the variation between the input orientation and the DFN model results is not significant.

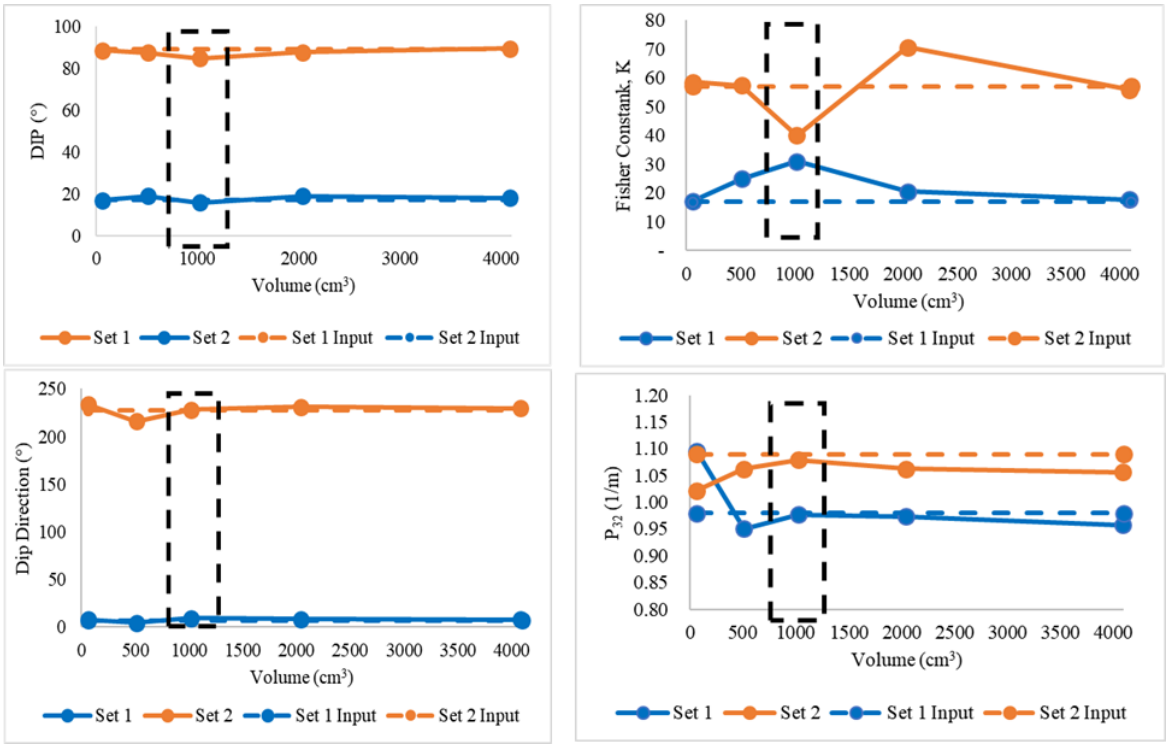

Figure 4.6 Average values for the (a) dip, (b) dip direction, (c) Fisher's constant K and (d) volumetric intensity P_{32} with increasing DFN volume.

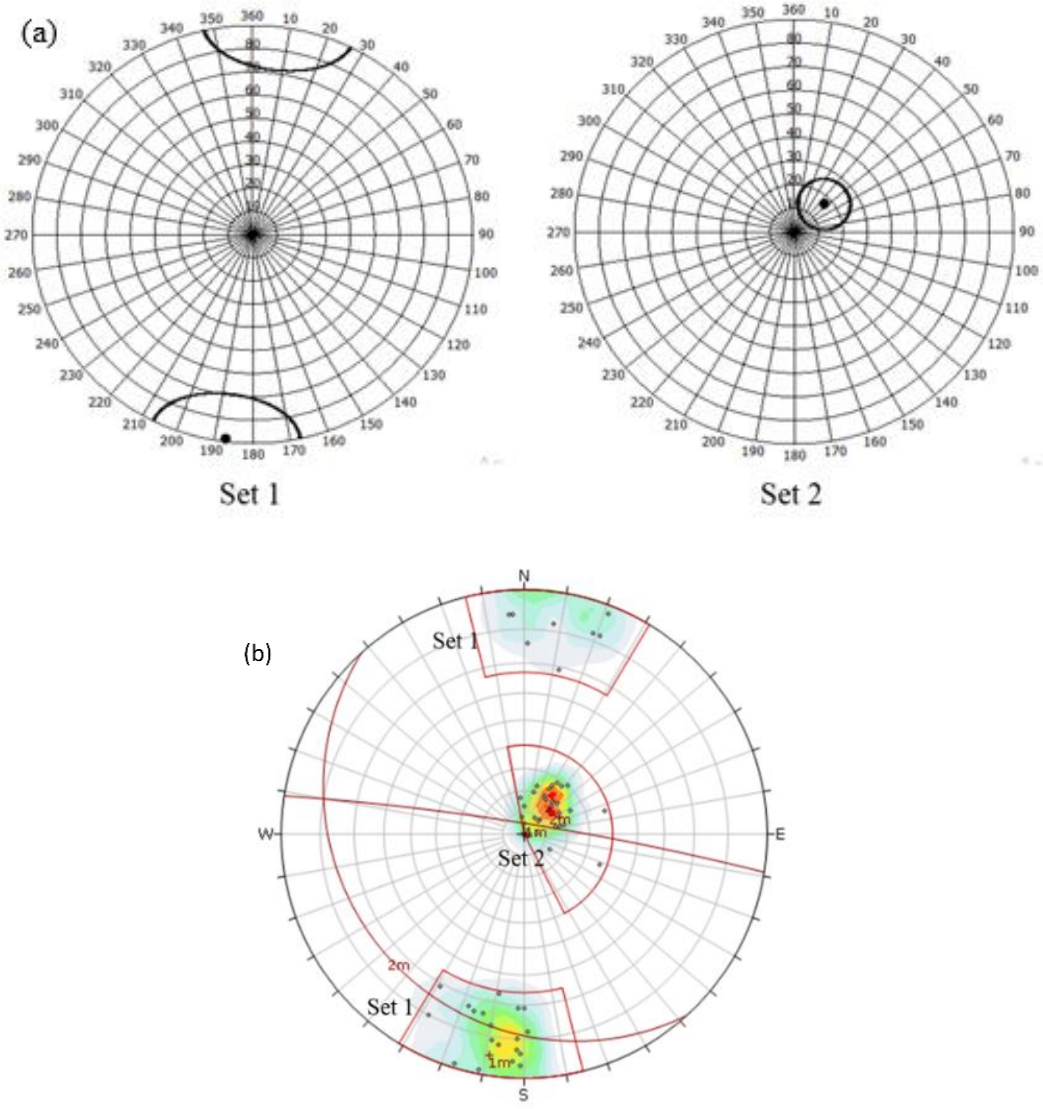

Figure 4.7 Stereographic projections for the orientation of the two-fracture sets (a) input orientation in MoFRAC and (b) orientation of the 58 fractures generated with MoFRAC visualized with DIPS

4.2.2 Three-Dimensional Physical Model

The first step to obtain a 3D printed DFN model was to model a 3D shape surrounding the fracture planes generated with MoFRAC and to model an aperture size for the fractures. The selected DFN volume (REV) was imported into the software Solidworks (SolidWorks, 2021) to generate the required solid. A cylindrical 3D shape was modeled to obtain a 3D volume representing a rockmass

with in-situ fractures. The aperture of the fractures was set to a fixed value of 1 mm. To ensure that the 3D printed DFN model does not have any loose parts due to intersecting fractures that can potentially create loose blocks in the 3D structure, an annulus of 1 mm was added around the boundary of the initial solid. This annulus of solid material with no fracture also ensures that the external boundary along the length of the physical model is impermeable to the flow during the experiment. Figure 4.8 shows the 3D solid modelled in Solidworks with fracture network of 1 mm aperture size each.

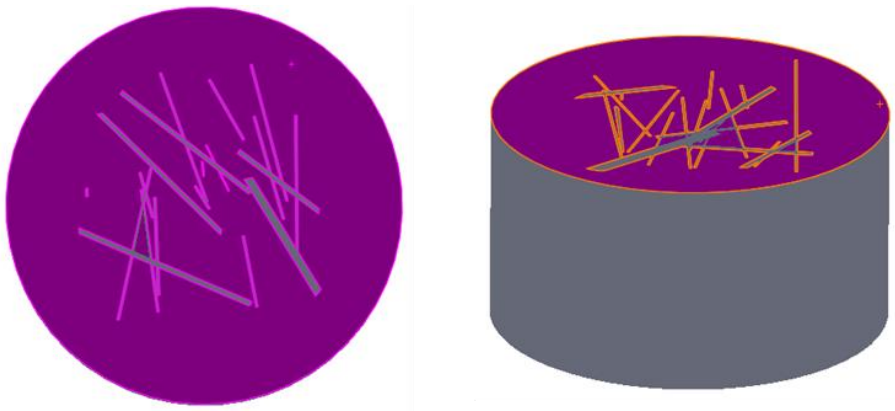

Figure 4.8 3D modeling of rockmass with DFN in SolidWorks

Additionally, the potential loose parts within the fracture network were supported by adding pins to the Solidworks design to fix these loose parts inside the 3D DFN model. The resulting 3D solid, cylindrical in shape, was represented as a 3D physical model with a 3D printer, as discussed in the next section. Figure 4.9a shows the 3D Solidworks model, with diameter and height of 16.8 cm and 9.0 cm respectively, and figure 4.9b shows a section through figure 4.9a, illustrating the location and aperture of the fractures.

4.2.3 3D printed Physical DFN Model

A physical DFN model was printed with ABS material using a Stratasys Dimension SST 1200es 3D printer in order to represent an in-situ fracture network. An initial 3D test model was designed and printed with a smaller number of fractures (12 fractures), in order to validate the accuracy of the 3D printer. The test print model geometry is 70 mm x 70 mm x 55 mm. The aperture of the fractures within the 3D printed DFN model was measured at various locations with feeler gauges and compared to the designed aperture of 1 mm. Figure 4.10 presents the flow-diagram of the test print generation and validation.

Measurements of the fracture aperture at different locations gave a range of 0.99 to 1.00 mm. Additionally, the test print was cut along its length to compare the location of the fractures with the 2D section obtained in Solidworks. The comparison between the 3D test print and the 3D model designed in Solidworks shows that the fracture aperture and location is comparable in both models. This validates that 3D printing technology can be used to represent a fracture network without significant variation from the designed geometrical properties.

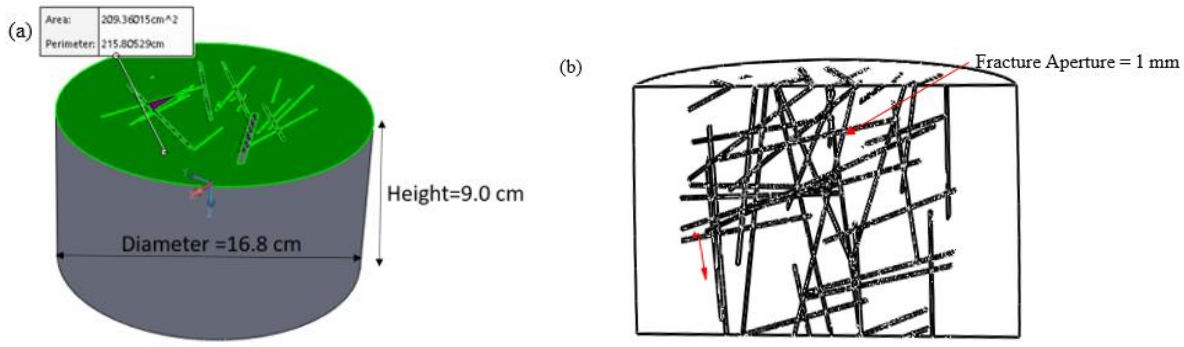

Figure 4.9 3D solid modeled in Solidworks with (a) 3D dimensions and (b) Longitudinal section showing the location and aperture of the fractures within the 3D model.

After validating the accuracy of the 3D printer, the selected REV, i.e. the DFN model with 2 fracture sets and a total of 58 fractures with each fracture assigned a thickness of 1 mm (Figure 4.5), was extruded in a 3D cylindrical solid body (Figure 4.9a). The generated 3D printed DFN model is shown in Figure 4.11.

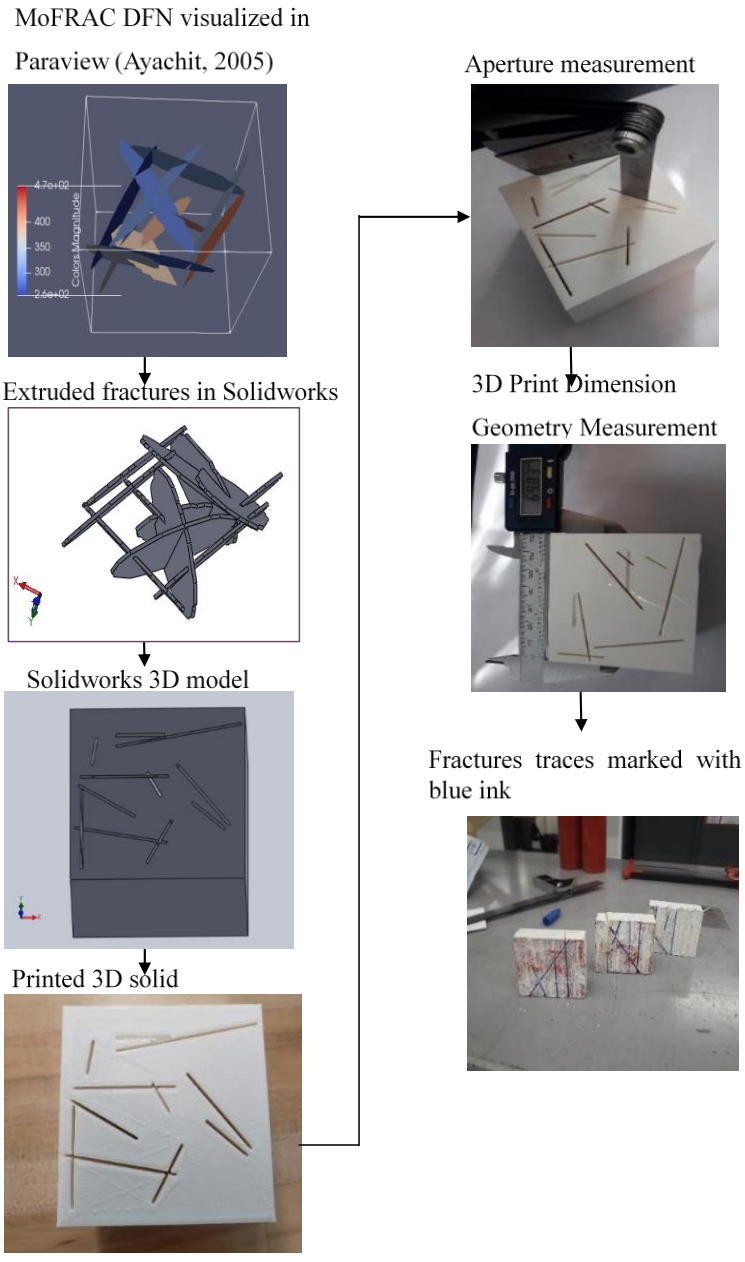

Figure 4.10 3D modeling process and test print validation

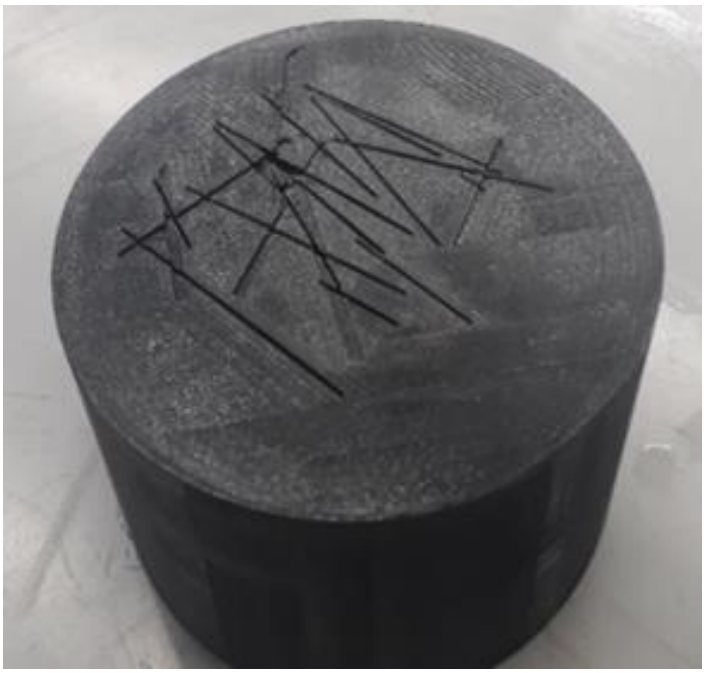

Figure 4.11 3D printed DFN model generated with a Stratasys Dimension SST 1200es 3D printer using ABS material

4.3 Lab-Scale Experiment for Fluid Flow Measurements

Fluid flow measurements were recorded with the 3D printed DFN model installed in an experimental set-up, with orifice plate which functions as a differential pressure meter by restricting the airflow through a transition duct (Morris and Langari, 2012). This experimental set-up is used to establish the behaviour of the changing pressure to fluid transfer through fracture openings.

4.3.1 Experimental Setup

Figures 4.12 and 4.13 show, respectively, a schematic diagram and the actual experimental setup (Figure 4.13a) with the orifice plates used for the flow measurement (Fig 4.13b). The experimental setup comprises a voltage source (feeder), a voltage regulator, a centrifugal fan, a transition duct, orifice plates, the 3D printed DFN model and a manometer. These devices are used to measure the airflow through the 3D printed DFN model.

The feeder supplies the power to the centrifugal fan, which induces air flow through the transition duct. The voltage regulator is used to control the flow pressure by regulating the fan pressure. The orifice plate, installed in the laboratory setup (Figure 4.13b), restricts the air flow through the transition duct (Morris and Langari, 2012). Two different orifice plates were used for flow measurements, with orifice diameters of 1.27" and 2.84". The manometer, fixed across the orifice plate, measures the pressure drop across the plate. The gauge pressure manometer measures the gauge pressure at the downstream of the flow. The gauge pressure is measured for the point at which flow enters the 3D printed DFN model. One end of the 3D printed DFN model is exposed to the atmosphere. For this reason, when the 3D printed DFN model is fixed to the setup, the gauge pressure is taken to be the pressure difference across the 3D sample in the experimental setup. A minimum length L_1 of straight transition duct between the fan and the flow measurement point (Figure 4.12) ensures that the flow conditions upstream are in steady state (Morris and Langari, 2012).

4.3.2 Data Collection and Calibration

The purpose of the experimental setup is to measure the airflow, Q (m^3/s), at different pressures. This will indicate whether the secondary permeability, represented by the 3D printed DFN model, is able to admit sufficient flow. At the start of the experiment, the voltage regulator is used to control the airflow pressure by controlling the energy supplied to the fan.

Flow measurements were collected in two steps, using each of the two orifice plates as a differential pressure meter. First, for calibration purposes, the gauge pressure and the flow rates with increasing flow pressure were evaluated without fixing the 3D printed DFN model to the experimental setup. These measured flow rates through the orifice provide the actual readings

through the setup with minimal resistance (i.e. in the absence of the 3D printed DFN model) at the downstream. These measurements are used to correct the errors in the measured pressure through the duct for the experiment with the 3D printed DFN model fixed, in order to calibrate the airflow measurements.

The second step involves the measurement of the pressure difference across the sample and the flow rate through the 3D printed DFN model, referred to as the main experiment. At this step, the 3D printed DFN model is fixed to the left end of the setup, as shown in Figure 4.13a. The pressure difference across the sample and the flow rates through the 3D printed DFN model are then measured.

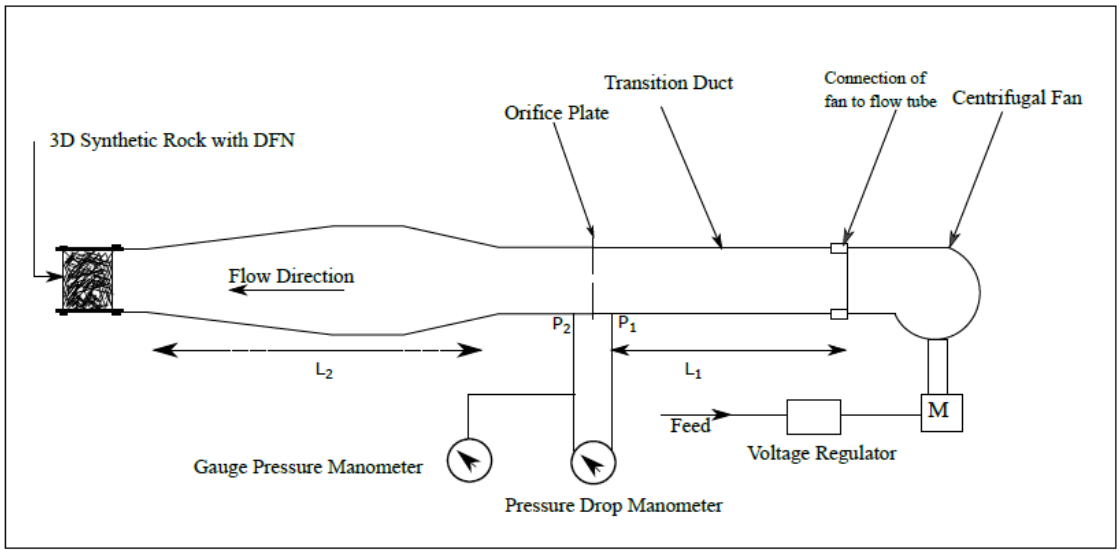

Figure 4.12 Schematic diagram of Anemometer Calibration Rig

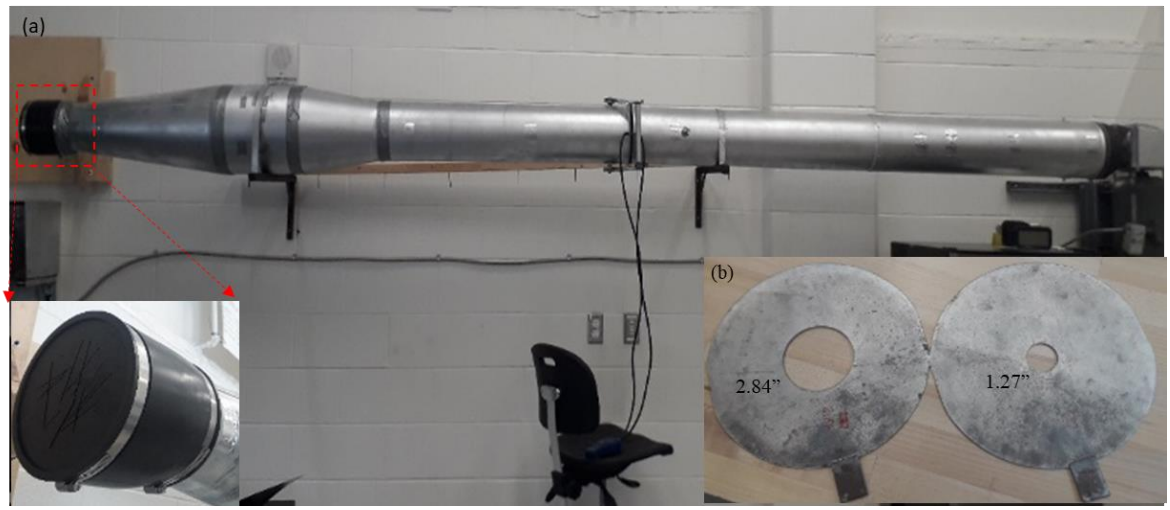

Figure 4.13 (a) Anemometer Calibration Rig and (b) Orifice plates used for the experiment

During the experimental work, sporadic temperature (T) and atmospheric pressure (P) measurements within the lab environment were collected to ensure that there is no significant variation. The maximum variation recorded is 0.87% and 0.67% for room temperature (Kelvin) and absolute pressure respectively. The measured flow velocity was between 0.00738 and 0.37833 m/s and air can be treated as an incompressible fluid (Anderson, 2003).

4.3.3 Impact of 3D Matrix Porosity

The 3D printed DFN model fracture porosity, as designed with Solidworks, is 8%. However, the 3D printed DFN model has voids in its internal structure (matrix) and the matrix porosity, as illustrated in Figure 4.14a, depends on the density of ABS material selected for the 3D printing process. An analysis of the impact of the 3D matrix porosity was performed to ensure that there is no significant portion of the flow that could be attributed to the matrix porosity.

The model porosity (i.e. fractures and matrix porosity) was calculated from equations 4.1 and 4.2, using the design model volume (bulk volume), V_b (i.e. 1845 cm^3), the actual volume of material,

V_S used for 3D printing (i.e. 1573 cm^3), and the void volume, V_V (i.e. 272 cm^3). The porosity, η of the 3D printed DFN model was estimated to about 14.7% as opposed to 8.0 % when considering fractures only.

$$V_v = V_b - V_s \tag{4.1}$$

$$\eta = \frac{V_v}{V_b} \times 100\% \tag{4.2}$$

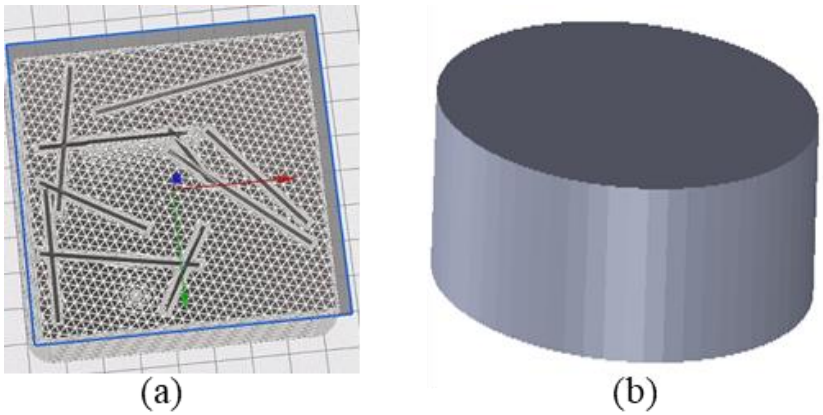

Figure 4.14 (a) Matrix (internal structure) of a 3D printed model (b) external boundary of a 3D printed model.

Visual observations of the 3D printed DFN model surface (Figure 4.14b) show a very tight and impermeable outer structure. This indicates the external surface and the surface of the fracture walls are likely to be impermeable to the flow. This implies that the measured flow is associated to the secondary (fracture) permeability only. In order to validate that the matrix porosity has no significant impact on the flow, a 3D printed model with no fractures (Figure 4.15) was generated. This solid was also used for the verification of potential leakage on the boundary of the model when fixed in the experimental setup.

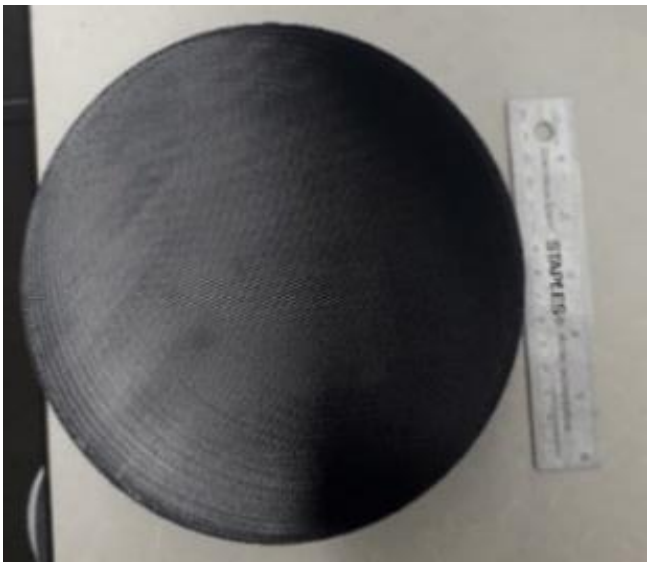

Figure 4.15 3D printed model without fractures

This 3D printed model with no fractures was fixed in the experimental setup to measure airflow at different pressures. Minimal flow was recorded, and this small amount could be attributed to minor leakage along the duct due to the high resistance to flow when the model with no fracture is fixed in the experimental setup. A simplified traditional approach was adopted to verify for potential leakage through the model internal structure. Soapy water was applied on the outer surface of the 3D printed model with no fractures to detect leakage with the apparition of air bubbles. At different pressures, there was no evidence of bubbling, which further demonstrate that the 3D outer structure and the surface of the fracture walls are impermeable to the flow despite the significant porosity estimated for the model.

4.4 Results and Discussions

The flow rate results of this lab-scale experiment are representative of the secondary permeability represented in a 3D printed DFN model with constant fracture aperture. First, the pressure through

the transition duct driving the flow is measured to calibrate the results. The best-fit equations for the pressure-flow rate curves without the 3D printed model fixed in the setup are shown in Figure 4.16.

This pressure difference recorded without the 3D printed DFN model fixed (Figure 4.16) is deducted from the pressure difference data recorded when the 3D printed DFN model is fixed to the setup. This allows calibrating the flow measurements in order to estimate the actual pressure difference at the inlet section of the 3D printed DFN model. The calibrated results of the pressure difference plotted against the measured flow rate through the 3D printed DFN model are shown in Figure 4.17.

As demonstrated in Figure 4.17, the flow results using the two orifice plates with different concentric diameters agree well. Additionally, it is observed that, as the pressure difference across the orifice plate is increased, the flow rate is gradually increased with a nonlinear relationship. A higher minimum pressure is required to detect flow when the larger orifice plate (2.84”) is used, because a lower pressure drop is measured across the plates. This is a limitation due to the precision of the manometer used to measure the pressure drop across the orifice plate.

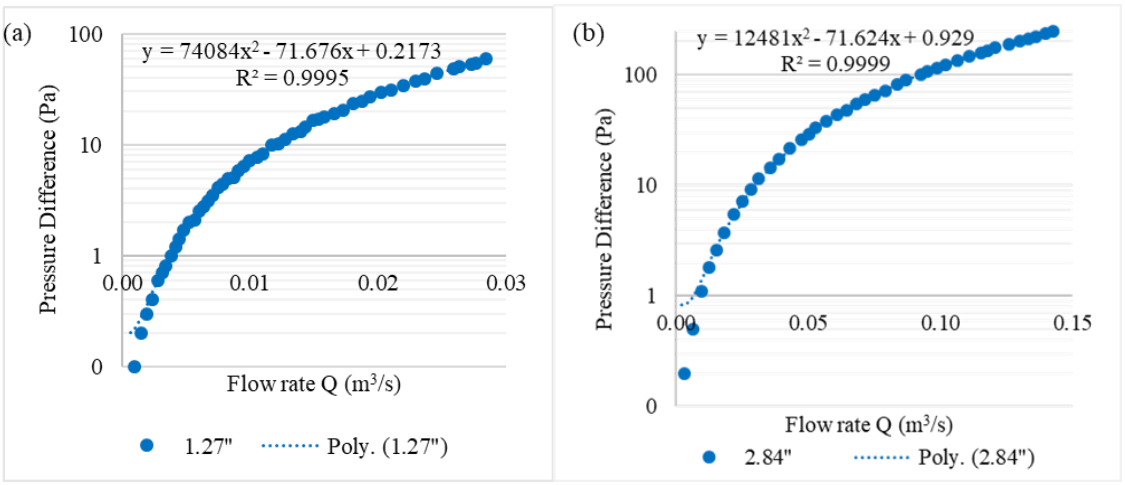

Figure 4.16 Flow rate with increasing pressure difference without the 3D printed model fixed in the experimental setup (i.e. with minimal airflow resistance) using (a) the 1.27" orifice plate and (b) the 2.84" orifice plate

The basic cubic law equation by Tiab and Donaldson (2015) as indicated in Table 2.2 was used to estimate the flow-pressure relationship based on the average fracture width and the number of fractures at the inlet section of the 3D printed DFN model (Figure 4.9b), which are respectively 4.07 cm and 19 fractures. These 19 fractures are prominent fractures receiving the flow at the inlet section. As illustrated on Figure 4.17, the basic approach described by Tiab and Donaldson (2015) yields a linear flow-pressure relationship, which is different from the nonlinearity observed from the laboratory results. Note that a logarithmic vertical axis is used to plot the results on Figure 4.17, but the best-fit shows the linear relation for the basic approach used. Additionally, Figure 4.17 illustrates that the basic approach can provide a good estimate of the flow-pressure relationship when the flow rate is relatively low, i.e. smaller than about 0.003 m^3/s. For higher flow rates, the difference between the basic approach and the measured flow rate becomes significant.

As expected, the basic approach cannot fully capture the flow through a fracture network. Given the complexity of fracture systems, there is no known exact formulation for the flow through a DFN. This highlights the need for experimental flow data, in order to calibrate the results obtained from numerical simulations, prior to upscaling the model to represent field properties. The data used for graphically representing Figure 4.16 and 4.17 are given in Appendices A to C. Appendix D, an excel VBA code for velocity conversion and measured fluid flowrate calculation, was developed by Laurentian University Ventilation Laboratory.

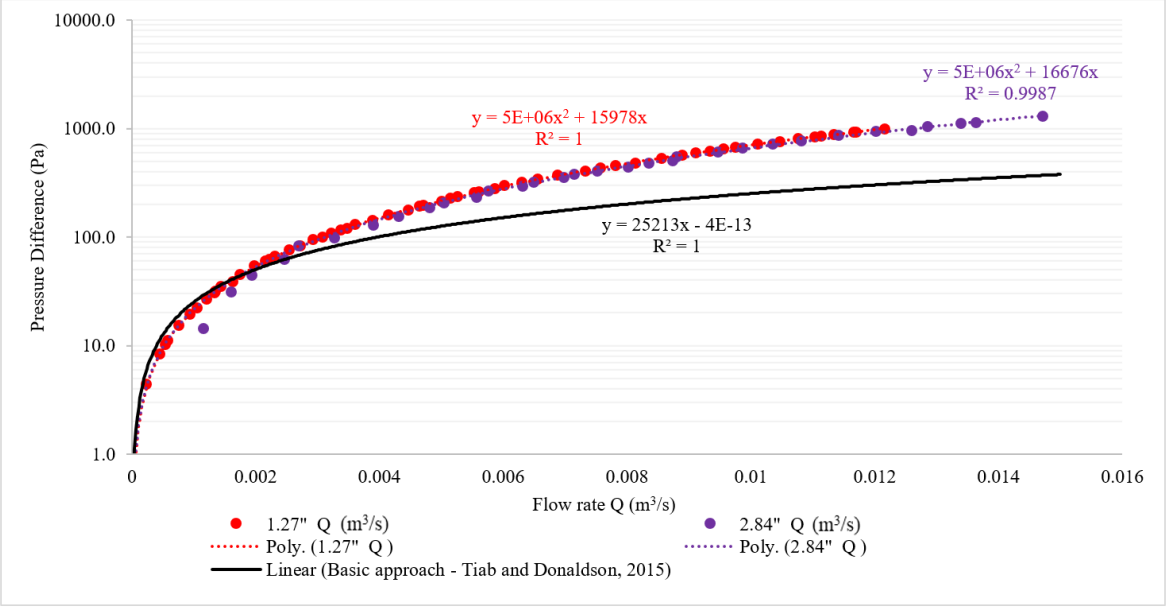

Figure 4.17 Calibrated pressure-flow rate curve measurements with 3D printed DFN model

4.5 Conclusion

The results of this study demonstrate that flow measurements can be obtained experimentally with a lab-scale 3D printed DFN model. Direct fluid flow measurements in fractured networks at the lab-scale are highly valuable because the results can be useful to obtain a physically quantified assessment (as opposed to numerical assessment) of the influence of the fracture properties

(intensity, connectivity, aperture, etc.) on fluid flow. For example, to evaluate the impact of increasing the secondary permeability of a rockmass with HF, the results of the base model are useful for comparison between the base model and the HF model, and for quantifying this impact.

The input pressure and the flow rate obtained from this lab experiment are key data collected and can be used to calibrate a subsequent numerical simulation to represent the experimental results. This is required for upscaling the model, in order to reliably represent the scale of the NHEET system.

Chapter 5

5 Conclusion and Recommendations for Future Research

5.1 Thesis Summary

Hydraulic fracturing in hard rock is gaining much interest in mining and, in some cases, has proven to be more efficient than conventional method like destress blasting. Its capability to reactivate and also generate new fractures in hard rock at various depth identifies the techniques to be beneficial in the NHEET alternative system, which seeks to improve the secondary permeability of in-situ rock material to optimize the air flow for a potential NHEET system.

HF is a tool to enhance strategically a given fracture network in a rockmass in order to optimize the secondary permeability of the rockmass. In this context, a numerical model has been developed in this research to simulate HP at the stage of fracture initiation or reactivation.

Additionally, fluid flow through the secondary permeability (DFN) in rock is of interest to various engineering applications. Existing literature places emphasis on laboratory experiments of mainly one fracture only, and those works have limited attention to lab-scale experiment for fluid flow through fracture network. Using existing state-of-the-art technologies, this research has investigated, with a lab-scale experiment, the influence of fracture network on airflow through the secondary permeability of a 3D physical model with DFN.

The review of existing literature was given in Chapter 2 to provide relevant background to fracturing in rock and flow through discrete fracture network. The result of the numerical model as given in Chapter 3 provides understanding of developing predictive model with HF in rock using numerical modeling. Chapter 4 provides the verification of secondary permeability in

discrete fracture network (DFN), which investigate the fluid flow through a 3D physical model using lab-scale experiment.

5.2 Conclusion

In this research, first a numerical model was developed to simulate a HP field experiment conducted in a Northern Ontario mine in which a breakdown pressure was achieved, and a pre-existing discontinuity was reopened. A calibration of the pumping water flowrate allowed the numerical model to estimate a breakdown pressure in good agreement with the results observed from the field experiment. This demonstrates that it is possible to estimate numerically the injection pressure required for hydraulic fracturing the rock mass by creating new fractures or reopening pre-existing ones in a rockmass. The results obtained numerically are in good agreement with those one from the actual experiment.

Considering this numerical model as a tool to make prognosis about the amount of pressure needed to stimulate a pre-existing fracture initiation, it is valuable to conduct such numerical simulations in order to reduce the amount of high cost HP field experiments. Effectively, fewer tests would be necessary for numerical model calibration. Also, a reliable rockmass characterization, an estimation of the natural stress distribution and the orientation of the preexisting discontinuities would be needed to perform such prognosis.

Similarly, with the existing software technology, a discrete fracture network has been developed during this research, including the estimation of the REV and the DFN representation in a 3D printed physical model. Thus, the model has customized joint sets with a defined orientation. This model represents a typical rockmass with DFN to be used in the laboratory for airflow

measurements. The laboratory experiment is conducted to determine whether the secondary permeability can admit fluid flow. The experimental results have shown that, with direct measurements, the influence of specific fracture and fracture network properties such as aperture, intensity, roughness, etc. on secondary permeability and fluid flow can be quantified. The lab-scale results are necessary to investigate the optimization of the secondary permeability of a DFN using HP.

5.3 Contributions of Research

The two major contributions of this research are:

(1) A HF predictive model for the breakdown pressure in hard rock is developed and calibrated based on the results obtained from a previously conducted field HP experiment. The numerical model developed is able to reliably predict the field HP breakdown pressure. This numerical model is useful to evaluate the amount of fluid pressure needed to stimulate pre-existing fracture opening, without carrying out high-cost HP field experiments.

(2) Airflow measurements through a lab-scale 3D printed DFN model are obtained to evaluate the secondary permeability of a fractured medium. Such experiment is unprecedented in the field of geomechanics. The impact of this research for various applications requiring the evaluation of fluid flow through a fractured media (e.g. oil industry, nuclear waste management, mining, etc.) is the opportunity to quantify, with direct measurements, the influence of specific fracture and fracture network properties (aperture, intensity, roughness, persistence, connectivity, etc.) on the resulting flow rate and secondary permeability. With the increasing variety of 3D printing materials available (e.g. sand, ceramic, etc.), this innovative work opens the door to lab-scale flow experiments using 3D

printing technology for studies that could be conducted with physical DFN models with varying matrix and fracture porosity.

In the context of the NHEET system, the potential key benefits are to:

(1) A developed numerical model which can serve as a valuable tool for predicting the magnitude of the injection pressure needed for fracture reopening, and to reach the breakdown pressure of the rock formation. This is very important for HP planning and operations required to optimize the fracture intensity in a rockmass;
(2) To determine whether the secondary permeability of a rock mass is sufficient to admit enough flow for providing economically significant seasonal/diurnal thermal regeneration capacity. The results of this study are valuable to investigate the hydraulic fracturing technique for rockmass preconditioning in order to enhance the secondary permeability of the rock mass and hence, to maximize flow through a fractured rock mass.

5.4 Research Limitations

Limitations encountered in this research have been summarised in section 5.4.1 and 5.4.2 respectively. Section 5.4.1 highlight the limitation relating to the numerical modeling and section 5.4.2 present the limitations during the modeling of the DFN, 3D physical model and laboratory experimental work.

5.4.1 Numerical Modeling Limitations

One of the limitations of this work was that the size of the numerical model, which was reduced due to very long computational time and lack of memory of the modeling computer used. Hence, due to the very large number of nodes involved, setting up a model to match the length of the

injection borehole of 24.7 m was not achievable and the model was reduced to 3.5m long x 3.5m wide x 3.0 m high. The model volume focused on the location of the injection cluster and a stress state representative of the field experiment was used for the numerical simulation. Additionally, the simulation focused on estimating the breakdown pressure because of the difficulties in simulating both breakdown pressure and fracture propagation in a single Xsite model. This is due to the significant difference in scale of the elements involved in the model, namely the injection borehole, the seed fracture, the injection cluster and the rockmass volume, which can vary from several orders of magnitude in scale. With a model at the rockmass scale, it was not possible to capture the peak representing the breakdown pressure. To simulate fracture propagation, a second model should be developed in Xsite, representing the rockmass scale.

5.4.2 Fluid Flow Experiment Limitations

As given by Mcpherson (2009), the frictional pressure drop depends on the air density as well as geometry of the airway. One of the limitations of the experiment is the inability to quantify resistance of the 3D flow path to the fluid flow through the fracture network due to the irregularity and complexity of the DFN in the 3D environment.

Another limitation was the 3D model size. Increasing the model size implies having more fractures and hence, more fracture networks. This is associated with having loose part in the 3D physical model. With the presence of loose parts, the pressure from the flow will distort the internal structure of the model. To overcome this, the model size was limited to the smallest REV as given in section 4.2.1.

Additionally, despite the sealing of potential leakages in the experimental setup, minor leakages were observed around the orifice plates, which were unavoidable. This motivated the printing of

the solid sample (i.e. the sample with no joint) which was tested to verify the influence of the internal matrix on the fluid flow measurements and to investigate potential fluid leakages in the experimental setup. Additionally, the precision of the manometer used for recording data requires higher minimum pressure to detect flow when the larger orifice plate (2.84”) is used, because a lower pressure drop is measured across the plates. As such, the manometer was limited to minimum pressure to detect flow across the orifice plates.

5.5 Recommendations for Future Research

This research has contributed to the modeling of HF and the verification of secondary permeability; to predict the amount of pressure needed to stimulate a pre-existing fracture initiation and to verify whether the secondary permeability of a DFN can admit flow respectively. This is part of ongoing research conducted at Mirarco Mining Innovation and future work is required to build on the research findings as follows:

(1) Investigating the fracture propagation from HP, as a subsequent process to fracture initiation;

(2) A second 3D printed DFN model with increased fracture intensity and connectivity representative of the HP treatment is required to evaluate the impact on airflow with different fracture intensity;

(3) Upscaling the numerical model and laboratory experiment to a larger scale for building a NHEET system and for evaluating the potential flow rate through the secondary permeability and its capability for thermal regeneration;

(4) Finally, a Computational Fluid Dynamics (CFD) model is required to represent the airflow results, which can be calibrated with the laboratory results.

References

Acuña, E. I. and Connor, D. O. (2010) 'A New Approach to Maximize the Natural Conditioning System at Creighton Mine', in *CIM Memo Conference*, Sudbury, Ontario, Canada.

Adachi, J., Siebrits, E., Peirce, A. and Desroches, J. (2007) 'Computer Simulation of Hydraulic Fractures', International Journal of Rock Mechanics & Mining Sciences, 44(5), pp. 739–757. Available at: https://doi.org/10.1016/j.ijrmms.2006.11.006.

Adams, J. and Rowe, C. (2013) 'Differentiating Applications of Hydraulic Fracturing', in ISRM International Conference for Effective and Sustainable Hydraulic Fracturing 2013, Brisbane, Australia, pp. 391–400. Available at: https://doi.org/10.5772/56114.

Amadei, B. and Stephansson, O. (1997) 'Methods of In-situ Stress Measurement', in *Rock Stress and Its Measurement*. Dordrecht: Springer, pp. 95–120. Available at: https://doi.org/10.1007/978-94-011-5346-1_3.

Anderson, J. D. (2003) 'Flight (Aerodynamics)', *Encyclopedia of Physical Science and Technology*, pp. 1–21. Available at: https://doi.org/10.1016/b0-12-227410-5/00915-7.

ASTM D4645-08 (2008) 'Standard Test Method for Determination of the In-Situ Stress in Rock Using the Hydraulic Fracturing Method 1', *ASTM International*, pp. 1–8. Available at: https://doi.org/10.1520/D4645-08.

ASTM D653-14 (2014) 'Standard Terminology Relating to Soil , Rock , and Contained Fluids', *ASTM International*, West Conshohocken, PA, pp. 1–45. Available at: https://doi.org/10.1520/D0653-14.2.

Atangana, A. (2018) ‘Principle of Groundwater Flow’, in *Fractional Operators with Constant and Variable Order with Application to Geo-Hydrology*, pp. 15–47. Available at: https://doi.org/10.1016/b978-0-12-809670-3.00002-3.

Baghbanan, A. and Jing, L. (2007) ‘Hydraulic Properties of Fractured Rock Masses with Correlated Fracture Length and Aperture’, *International Journal of Rock Mechanics and Mining Sciences*, 44(5), pp. 704–719. Available at: https://doi.org/10.1016/j.ijrmms.2006.11.001.

Baidoo, M., Gonzalez, C. and Fillion, M.-H. (2023) ‘Numerical Modeling of the Breakdown Pressure from a Hydraulic Preconditioning Field Experiment in a Deep Northern Ontario Mine’. [Manuscript in preparation], pp. 25.

Barati, R. and Liang, J. (2014) ‘A Review of Fracturing Fluid Systems used for Hydraulic Fracturing of Oil and Gas Wells’, *Journal of Applied Polymer Science*, 131(16), pp. 1–11. Available at: https://doi.org/10.1002/app.40735.

Belyadi, H., Fathi, E. and Belyadi, F. (2019) ‘Rock Mechanical Properties and In-Situ Stresses’, in *Hydraulic Fracturing in Unconventional Reservoirs*. Elsevier, pp. 215–231. Available at: https://doi.org/10.1016/b978-0-12-817665-8.00013-8.

Berre, I., Doster, F. and Keilegavlen, E. (2019) ‘Flow in Fractured Porous Media: A Review of Conceptual Models and Discretization Approaches’, *Transport in Porous Media*, 130(1), pp. 215–236. Available at: https://doi.org/10.1007/s11242-018-1171-6.

Blyth, F. G. H. and de Freitas, M. (2017) *A Geology for Engineers*. Seventh Edition, pages 337. London: Elsevier Butterworth Heinemann.

Cai, M. (1990) *Comparative Tests and Studies of Overcoring Stress Measurement Devices in Different Rock Conditions*. Ph. D. Thesis. Australia: University of South Wales.

Cai, M. and Kaiser, P .K. (2018) 'Rockburst Support Reference Book' [Unpublished Manuscript], pp. 284. MIRARCO Mining Innovation, Laurentian University, Sudbury, Canada. Available at: https://mirarco.org/rockburst-support-reference-book/.

Cardona, A., Finkbeiner, T. and Santamarina, J. C. (2021) 'Natural Rock Fractures: From Aperture to Fluid Flow', *Rock Mechanics and Rock Engineering*, 54(11), pp. 5827–5844. Available at: https://doi.org/10.1007/s00603-021-02565-1.

Chen, Z., Narayan, S. P., Yang, Z. and Rahman, S. S. (2000) 'An Experimental Investigation of Hydraulic Behaviour of Fractures and Joints in Granitic Rock', *International Journal of Rock Mechanics and Mining Sciences*, 37(7), pp. 1061–1071. Available at: https://doi.org/10.1016/S1365-1609(00)00039-3.

Chen, Z. R. and Jeffrey, R. G. (2009) 'Tilt Monitoring of Hydraulic Fracture Preconditioning Treatments', *43rd U.S. Rock Mechanics Symposium and 4th U.S.-Canada Rock Mechanics Symposium*, Asheville, North Carolina USA.

Cheng, Y. and Zhang, Y. (2020) 'Experimental Study of Fracture Propagation: The Application in Energy Mining', *Energies*, 13(6), pp. 1411. Available at: https://doi.org/10.3390/en13061411.

Cheng, Y., Zhang, Y., Yu, Z., Hu, Z., Ma, Y. and Yang, Y. (2021) 'Experimental and Numerical Studies on Hydraulic Fracturing Characteristics with Different Injection Flow Rates in Granite Geothermal Reservoir', *Energy Science and Engineering*, 9(1), pp. 142–168. Available at: https://doi.org/10.1002/ese3.816.

Ching, H. and Weng, Y. X. (2014) *Mechanics of Hydraulic Fracturing*. Second Edition. Gulf professional publishing.

Dai, Z. and Zhou, X. (2020) 'Research on Application of Hydraulic Fracturing Enhanced Technology in Coal Mine', *Geotechnical and Geological Engineering*, 38(2), pp. 1521–1529. Available at: https://doi.org/10.1007/s10706-019-01107-5.

Damjanac, B., Detournay, C. and Cundall, P. (2020) 'Modeling Rock Fracturing Processes', in *Numerical Simulation of Hydraulically Driven Fractures*. Springer, Cham, pp. 531–561. Available at: https://doi.org/10.1007/978-94-007-6904-5.

Damjanac, B., Detournay, C., Cundall, P., Purvance, M. and Hazzard, J. (2011) *HF Simulator: Description of Formulation with Validation Problems Revision I*, Itasca Consulting Group, Minneapolis, Minnesota 55401, USA.

Damjanac, B., Detournay, C. and Cundall, P. A. (2016) 'Application of Particle and Lattice Codes to Simulation of Hydraulic Fracturing', *Computational Particle Mechanics*, 3(2), pp. 249–261. Available at: https://doi.org/10.1007/s40571-015-0085-0.

Damjanac, B., Detournay, C., P. A., C. and Varun (2013) 'Three-Dimensional Numerical Model of Hydraulic Fracturing in Fractured Rock Masses', in *ISRM International Conference for Effective and Sustainable Hydraulic Fracturing*, pp. 819–830. Available at: https://doi.org/10.5772/56313.

Djabelkhir, N. (2020) *Simulation of Notch Driven Hydraulic Fracture in Open Hole Completion*. Ph. D. Thesis and Dissertation. University of North Dakota, Grand Ford, North Dakota.

Dontsov, E. V. and Zhang, F. (2018) ‘Calibration of Tensile Strength to Model Fracture Toughness with Distinct Element Method’, *International Journal of Solids and Structures*, 144, pp. 180–191. Available at: https://doi.org/10.1016/j.ijsolstr.2018.05.001.

Esmaieli, K., Hadjigeorgiou, J. and Grenon, M. (2010) ‘Estimating Geometrical and Mechanical REV Based on Synthetic Rock Mass Models at Brunswick Mine’, *International Journal of Rock Mechanics and Mining Sciences*, 47(6), pp. 915–926. Available at: https://doi.org/10.1016/j.ijrmms.2010.05.010.

Fairhurst, C. (2013) ‘Fractures and Fracturing - Hydraulic Fracturing in Jointed Rock’, in *ISRM International Conference for Effective and Sustainable Hydraulic Fracturing*, Brisbane, pp. 47–79. Available at: https://doi.org/http://dx.doi.org/10.5772/56366.

Fan, J., Dou, L., He, H., Du, T., Zhang, S., Gui, B. and Sun, X. (2012) ‘Directional Hydraulic Fracturing to Control Hard-Roof Rockburst in Coal Mines’, *International Journal of Mining Science and Technology*, 22(2), pp. 177–181. Available at: https://doi.org/10.1016/j.ijmst.2011.08.007.

Farkas, M. P., Yoon, J. S., Zang, A., Zimmermann, G., Stephansson, O., Lemon, M. and Dankó, G. (2019) ‘Effect of Foliation and Fluid Viscosity on Hydraulic Fracturing Tests in Mica Schists Investigated Using Distinct Element Modeling and Field Data’, *Rock Mechanics and Rock Engineering*, 52(2), pp. 555–574. Available at: https://doi.org/10.1007/s00603-018-1598-7.

Fava, L., Millar, D., Anderson, B., Schafrik, S., O’Connor, D. and Allen, C. (2012) ‘Modeling of the Natural Heat Exchange Area At Creighton Mine For Operational Decision Support’, in *14th United States/North American Mine Ventilation Symposium*. Salt Lake City, pp. 351–358.

Feng, X. T. (2018) ‘Avoiding High-Stress Concentrations by Reasonable Excavation Methods’, in *Rockburst: Mechanisms, Monitoring, Warning, and Mitigation*. Butterworth-Heinemann: Elsevier Inc., pp. 441–451. Available at: https://doi.org/10.1016/B978-0-12-805054-5.00013-5.

Fernandes, J. S., Appoloni, C. R. and Fernandes, C. P. (2012) ‘Determination of the Representative Elementary Volume for the Study of Sandstones and Siltstones By X-Ray Microtomography’, *Materials Research*, 15(4), pp. 662–670. Available at: https://doi.org/10.1590/S1516-14392012005000081.

Fu, W., Savitski, A. A., Damjanac, B. and Bunger, A. P. (2019) ‘Three-Dimensional Lattice Simulation of Hydraulic Fracture Interaction with Natural Fractures’, *Computers and Geotechnics*, 107, pp. 214–234. Available at: https://doi.org/10.1016/j.compgeo.2018.11.023.

Gambino, G .F. ., Harrison, J. P . and Bedi, A. (2014) ‘Parameter Characterization for Rock Mass Preconditioning Using Hydraulic Fracturing’, Rock Engineering and Rock Mechanics: *Structures in and on Rock Masses - in ISRM European Regional Symposium-EUROCK 2014*, Vigo, Spain, 27-29 May 2014. Edited by Alejano, Perucho, Olalla and Jiménez, 695–700. Rotterdam: Balkema. Available at: https://doi.org/10.1201/b16955-119.

Guo, F., Morgenstern, N. R. and Scott, J. D. (1993) ‘Interpretation of Hydraulic Fracturing Breakdown Pressure’, *International Journal of Rock Mechanics and Mining Sciences* and, 30(6), pp. 617–626. Available at: https://doi.org/10.1016/0148-9062(93)91221-4.

Haimson, B. and Fairhurst, C. (1969) ‘In-Situ Stress Determination at Great Depth by Means of Hydraulic Fracturing’, in *11th U.S. Symposium on Rock Mechanics*, USRMS 1969, London, pp. 559–584.

Haimson, B. C. (1993) *The Hydraulic Fracturing Method of Stress Measurement: Theory and Practice, Comprehensive Rock Engineering*. Vol. 3. Pergamon Press Ltd. Available at: https://doi.org/10.1016/b978-0-08-042066-0.50021-5.

Haimson, B. C. and Cornet, F. H. (2003) 'ISRM Suggested Methods for Rock Stress Estimation-Part 3: Hydraulic fracturing (HF) and/or Hydraulic Testing of Pre-Existing Fractures (HTPF)', *International Journal of Rock Mechanics and Mining Sciences*, 40(7–8), pp. 1011–1020. Available at: https://doi.org/10.1016/j.ijrmms.2003.08.002.

Han, H. X. and Yin, S. (2018) 'Determination of In-Situ Stress and Geomechanical Properties from Borehole Deformation', *Energies*, 11(1). Available at: https://doi.org/10.3390/en11010131.

Hayashi, K., Ito, T. and Abe, H. (1989) 'In-Situ Stress Determination by Hydraulic Fracturing—a Method Employing an Artificial Notch.', *In International Journal of Rock Mechanics and Mining Sciences & Geomechanics Abstracts*, 26(3–4), pp. 197–202. Pergamon. Available at: https://doi.org/10.1016/0148-9062(89)91969-4.

Hayashi, K., Sato, A. and Ito, T. (1997) 'In-Situ Stress Measurements by Hydraulic Fracturing For a Rock Mass with many Planes of Weakness', *International Journal of Rock Mechanics and Mining Sciences*, 34(1), pp. 45–58. Available at: https://doi.org/10.1016/S1365-1609(97)80032-9.

He, Q., Suorineni, F. T. and Oh, J. (2016) 'Review of Hydraulic Fracturing for Preconditioning in Cave Mining', *Rock Mechanics and Rock Engineering*, 49(12), pp. 4893–4910. Available at: https://doi.org/10.1007/s00603-016-1075-0.

Healy, J. H. and Zoback, M. D. (1988) ‘Hydraulic Fracturing In-Situ Stress Measurements to 2.1 Km Depth at Cajon Pass, California’, *Geophysical Research Letters*, 15(9), pp. 1005–1008. Available at: https://doi.org/10.1029/GL015i009p01005.

Hoek, E., Kaiser, P .K. and and Bawden, W. F. (2000) *Support of Underground Excavations in Hard Rock*. CRC Press.

Hu, Y., Chen, G., Cheng, W. and Yang, Z. (2014) ‘Simulation of Hydraulic Fracturing in Rock Mass using a Smeared Crack Model’, *Computers and Structures*, 137, pp. 72–77. Available at: https://doi.org/10.1016/j.compstruc.2013.04.011.

Huang, B. X., Huang, C. M., Cheng, Q. Y., Huang, C. H. and Xue, W. C. (2012) ‘Hydraulic Fracturing Technology for Improving Permeability in Gas-Bearing Coal Seams in Underground Coal Mines’, *Journal of the Southern African Institute of Mining and Metallurgy*, 112(6), pp. 485–495.

Huang, L., Liu, J., Zhang, F., Fu, H., Zhu, H. and Damjanac, B. (2020) ‘3D Lattice Modeling of Hydraulic Fracture Initiation and Near-Wellbore Propagation for Different Perforation Models’, *Journal of Petroleum Science and Engineering*, 191. Available at: https://doi.org/10.1016/j.petrol.2020.107169.

Hubbert, M. K. and Willis, D. G. (1957) *Mechanics of Hydraulic Fracture*. *Transactions of the AIME*, 210(01), pp. 153–168. Available at: https://doi.org/10.2118/686-g.

Hudson, J. A. and Harrison, J. P. (1997) *Engineering Rock Mechanics: An Introduction to the Principles*, Pergamon, Elsevier Science Ltd., New York - Oxford: Elsevier Science

Ibrahim, A. F. and Nasr-El-Din, H. (2018) ‘Evaluation of the Breakdown Pressure to Initiate Hydraulic Fractures of Tight Sandstone and Shale Formations’, in *SPE Trinidad and Tobago Section Energy Resources Conferenc*e, pp. 1–19. Available at: https://doi.org/10.2118/191245-ms.

IPI (2022) DuraFRAC ® *HP Straddle, www.ipipackers.com*. Inflatable Packers International (IPI).

Itasca (2013) *X-site User ’ s Guide and Tutorial*. Itasca Consulting Group, Minneapolis, Minnesota 55401, USA.

Itasca (2022) *XSite Version 3.0- Hydraulic Fracture Simulation of 3D Fracture Networks*. Available at: https://www.itascacg.com/software/XSite (Accessed: 26 May 2022).

Ivars, D. M., Pierce, M. E., Darcel, C., Reyes-Montes, J., Potyondy, D. O., Paul Young, R. and Cundall, P .A. (2011) ‘The Synthetic Rock Mass Approach for Jointed Rock Mass Modeling’, *International Journal of Rock Mechanics and Mining Sciences*, 48(2), pp. 219–244. Available at: https://doi.org/10.1016/j.ijrmms.2010.11.014.

Ivars, M. D., Potyondy, D. O., Pierce, M. and and Cundall, P .A. (2008) ‘The Smooth-Joint Contact Model’, *Proceedings of WCCM8-ECCOMAS*, 2008, (July), pp. 1–3.

Jiang, C. (2017) *Hydraulic Fracturing Through 3D Printing and Lattice Modeling*. Ph. D. Thesis, University of New South Wales.

Junkin, W. R., Fava, L., Ben-Awuah, E. and Srivastava, R. M. (2018) ‘Analysis of Mofrac Generated Deterministic and Stochastic Discrete Fracture Network Models’, *2nd International Discrete Fracture Network Engineering Conference*, DFNE 2018 .

Kaiser, P .K. and Cai, M. (2012) ‘Design of Rock Support System Under Rockburst Condition’, *Journal of Rock Mechanics and Geotechnical Engineering*, 4(3), pp. 215–227. Available at: https://doi.org/10.3724/spp.j.1235.2012.00215.

Kaiser, P .K., Valley, B., Dusseault, M. B. and Duff, D. (2013) ‘Hydraulic Fracturing Mine Back Trials — Design Rationale and Project Status’, in *ISRM International Conference for Effective and Sustainable Hydraulic Fracturing*. pp. 877–891. Brisbane, Australia. Available at: https://doi.org/10.5772/56260.

Katsaga, T., Riahi, A., DeGagne, D. O., Valley, B. and Damjanac, B. (2015) ‘Hydraulic Fracturing Operations in Mining: Conceptual Approach and DFN Modeling Example’, *Transactions of the Institutions of Mining and Metallurgy*, Section A: Mining Tech., 124(4), pp. 255–266. Available at: https://doi.org/10.1179/1743286315Y.0000000022.

Klimczak, C., Schultz, R. A., Parashar, R. and Reeves, D. M. (2010) ‘Cubic Law with Aperture-Length Correlation: Implications for Network Scale Fluid Flow’, *Hydrogeology Journal*, 18(4), pp. 851–862. Available at: https://doi.org/10.1007/s10040-009-0572-6.

Konicek, P., Saharan, M. R. and Mitri, H. (2011) ‘Destress Blasting in Coal Mining - State-of-the-Art Review’, in *Procedia Engineering*, pp. 179–194. Available at: https://doi.org/10.1016/j.proeng.2011.11.2157.

Kulatilake, P. H. S. W., Park, J. and Su, X. (2020) ‘Fluid Flow Through Natural Single-Rock Fractures: Experimental and Numerical Investigations’, *International Journal of Geomechanics*, 20(10), pp. 04020168 (1-11). Available at: https://doi.org/10.1061/(asce)gm.1943-5622.0001790.

Lakirouhani, A. and Farkhondeh, S. (2018) ‘Effective Parameters on Breakdown Pressure in Hydraulic Fracturing , Modeling with Finite Difference Method’, 50(3), pp. 171–174. Available at: https://doi.org/10.22060/ceej.2017.12514.5221.

Lavrov, A. (2016) ‘Natural Fractures in Rocks’, in *Lost Circulation: Mechanisms and Solutions*, pp. 49–80. Available at: https://doi.org/10.1016/b978-0-12-803916-8.00003-0.

Lei, Q. (2020) ‘Characterization and Modeling of Natural Fracture Networks: Geometry, Geomechanics and Fluid Flow’, *Rock Mechanics for Natural Resources and Infrastructure Development- Proceedings of the 14th International Congress on Rock Mechanics and Rock Engineering*, ISRM 2019, pp. 183–207.

Lei, Q., Latham, J. P. and Tsang, C. F. (2017) ‘The use of Discrete Fracture Networks for Modeling Coupled Geomechanical and Hydrological Behaviour of Fractured Rocks’, *Computers and Geotechnics*, 85, pp. 151–176. Available at: https://doi.org/10.1016/j.compgeo.2016.12.024.

Lekontsev, Y.. and Sazhin, P. V. (2008) ‘Application of the Directional Hydraulic Fracturing at Berezovskaya Mine’, *Journal of Mining Science*, 44(3), pp. 127–147. Available at: https://doi.org/10.1029/rf003p0127.

Lhomme, T. P. (2005) ‘Initiation of Hydraulic Fractures in Natural Sandstones’, Pages 281. Delft University of Technology

Li, B., Mo, Y., Zou, L., Liu, R. and Cvetkovic, V. (2020) ‘Influence of Surface Roughness on Fluid Flow and Solute Transport Through 3D Crossed Rock Fractures’, *Journal of Hydrology*, 582, pp. 124386. Available at: https://doi.org/10.1016/j.jhydrol.2019.124284.

Li, C. C., Mikula, P., Simser, B., Hebblewhite, B., Joughin, W., Feng, X. and Xu, N. (2019) 'Discussions on Rockburst and Dynamic Ground Support in Deep Mines', *Journal of Rock Mechanics and Geotechnical Engineering*, 11(5), pp. 1110–1118. Available at: https://doi.org/10.1016/j.jrmge.2019.06.001.

Li, X., Feng, Z., Han, G., Elsworth, D., Marone, C., Saffer, D. And Cheon, D. S. (2016) 'Breakdown Pressure and Fracture Surface Morphology of Hydraulic Fracturing in Shale with H_2O, CO_2 and N_2', *Geomechanics and Geophysics for Geo-Energy and Geo-Resources*, 2(2), pp. 63–76. Available at: https://doi.org/10.1007/s40948-016-0022-6.

Lin, H., Oh, J., Masoumi, H., Zhang, C., Canbulat, I. and Dou, L. (2018) 'A Review of In-Situ Stress Measurement Techniques', in *Proceedings of the Coal Operators Conference, Mining Engineering*, University of Wollongong, Australia, pp. 95–10.

Love, J. J. (2007) Fisher Statistics. In *Encyclopedia of Geomagnetism and Paleomagnetism*. Edited by Gubbins, D. and Herrero-Bervera, E. Springer, Dordrecht. https://doi.org/10.1007/978-1-4020-4423-6_100

Maloney, S. and Gonzalez, C. (2017) 'Hydraulic Preconditioning of Highly Stressed Rock Masses', in *RaSiM Presentation*, Chile.

Markou, N. and Papanastasiou, P. (2018) 'Petroleum Geomechanics Modeling in The Eastern Mediterranean Basin : Analysis and application of fault stress mechanics', *Oil & Gas Science and Technology - Revue d'IFP Energies nouvelles*, 73, pp. 57. Available at: https://doi.org/10.2516/ogst/2018034.

Mazaira, A. and Konicek, P. (2015) 'Intense Rockburst Impacts in Deep Underground Construction and their Prevention', *Canadian Geotechnical Journal*, 52(10), pp. 1426–1439. Available at: https://doi.org/10.1139/cgj-2014-0359.

Mcpherson, M. J. (2009) 'Subsurface Ventilation Engineering', 2nd Edition. Mine Ventilation Services, Inc., Fresno, California Pages 905.

MIRARCO (2019) '*Natural Heat Exchange Engineering Technology for Mines'*, [PowerPoint Presentation]. MIRARCO Mining Innovation, Sudbury, ON, Canada. December, 2019.

MIRARCO (2020a) *MoFrac User Manual Version 4.0.1*. MIRARCO Mining Innovation, Sudbury, ON, Canada.

MIRARCO (2020b) '*Natural Heat Exchange Engineering Technology (NHEET) for Mines'* [PowerPoint Presentation]. MIRARCO Mining Innovation, Sudbury, ON. January, 2022.

MIRARCO (2022) '*MOFRAC Software, Version 4.2.0'* [Computer Program], Available at: https://mofrac.com/, MIRARCO Mining Innovation, Sudbury, ON, Canada.

Morris, A. S. and Langari, R. (2012) 'Flow Measurement', in *Measurement and instrumentation: theory and application*. Amsterdam: Academic Press, pp. 426–434.

Nordqvist, W. A., Tsang, Y. W., Tsang, C. F., Dverstorp, B and Andersson, J. (1992) 'A Variable Aperture Fracture Network Model for Flow and Transport in Fractured Rocks', *Water Resources Research*, 28(6), pp. 1703–1713.

Öhman, J. (2005) *Upscaling of Flow, Transport, and Stress-effects in Fractured Rock*. Ph. D. Thesis. Acta Universitatis Upsaliensis.

Ouchterlony, F. (1990) ‘Fracture Toughness Testing of Rock with Core Based Specimens’, *Engineering Fracture Mechanics*, 35(1–3), pp. 351–366. Available at: https://doi.org/10.1016/0013-7944(90)90214-2.

Pardo, C. and Rojas, E. (2016) ‘Selection of Exploitation Method Based on the Experience of Hydraulic Fracture Techniques at the El Teniente Mine’, in *Seventh International Conference & Exhibition on Mass Mining (MassMin 2016)* Sydney, Australia, pp. 97–104.

Pardo, M. C. (2015) *Back Analysis of Intensive Rock Mass Damage at the El Teniente Mine*, Ph. D. Thesis. Curtin University.

Pettitt, W., Pierce, M., Damjanac, B., Hazzard, J., Lorig, L., Fairhurst, C., Gil, I., Sanchez, M., Nagel, N., Reyes-Montes, J. and Young, R.PP. (2011) ‘Fracture Network Engineering for Hydraulic Fracturing’, *Leading Edge*, 30(8), pp. 844–853. Available at: https://doi.org/10.1190/1.3626490.

Pierce, M. E., Mas Ivars, D. and Sainsbury, D. (2009) ‘Use of Synthetic Rock Masses (SRM) to Investigate Jointed Rock Mass Strength and Deformation Behavior’, In *Proceedings of the International Conference on Rock Joints and Jointed Rock Masses*. Tucson, Arizona, USA.

Potyondy, D. O. and Cundall, P .A. (2004) ‘A Bonded-Particle Model for Rock’, *International Journal of Rock Mechanics and Mining Sciences*, 41(8), pp. 1329–1364. Available at: https://doi.org/10.1016/j.ijrmms.2004.09.011.

Qiu, D. (2021) *Hydraulic Fracture Propagation and its Geometry Evolvement in Transversely Isotropic Formations*. Ph. D. Thesis, University of North Dakota, Grand Forks, North Dakota.

Ranjith, P .G. and Viete, D. R. (2011) ‘Applicability of the “ Cubic Law ” for Non-Darcian Fracture Flow’, *Journal of Petroleum Science and Engineering*, 78(2), pp. 321–327. Available at: https://doi.org/10.1016/j.petrol.2011.07.015.

Rocscience Inc. (2022) *DIPS Software* [Computer Program], Version 8, Interactive Analysis of Orientation Based Geological Data, https://www.rocscience.com/software/dips, Toronto, Ontario, Canada.

Rogers, S., Elmo, D. and Beddoes, R. (2009) ‘Mine scale DFN Modeling and Rapid Upscaling in Geomechanical Simulations of large Open Pits’, In *Proceedings of International Conference on Slope Stability*, Santiago Chile, pp. 1–11. Available at: papers3://publication/uuid/91AA0AE7-347B-4AF8-B0A7-68FE3FE7E675.

Rojas, E., Landeros, P. and Vallejos, J. (2017). Hydraulic Fracturing Applied to Tunnel Development at El Teniente Mine. In *Proceedings of the 9th International Symposium on Rockbursts and Seismicity in Mines*, University of Chile, Santiago. pp. 236-242.

Rousell, D. H., Ames, D. E., Brown, G. H., Card, K. D., Fedorowich, J. S., Golightly, J. P., Gray, M. J., James, R. S., Jobin-Bevans, S., Long, D. G.., Naldrett, A. J., Paakki, J. J., Pattison, E. F., Riller, U., Stoness, J. A. and Koziol, B. (2009) A Field Guide to the Geology of Sudbury, Ontario, Ontario Geological Survey Open File.

Rubtsova, E. V. and Skulkin, A. A. (2018) ‘Hydraulic Fracturing Stress Measurement in Underground Salt Rock Mines at Upper Kama Deposit’, *IOP Conference Series: Earth and Environmental Science*, 134(1). IOP Publishing. Available at: https://doi.org/10.1088/1755-1315/134/1/012049.

Saeidi, N., Romero, A., Fava, L. and and Allen, C. (2017) 'Simulation of Large-Scale Thermal Storage in Fragmented Rock Modelled as a Discretised Porous Medium–Application to the Natural Heat Exchange Area at Creighton Mine.', in *UMT 2017: Proceedings of the First International Conference on Underground Mining Technology* (pp. 153-165). Australian Centre for Geomechanics. Available at: https://doi.org/https://doi.org/10.36487/ACG_rep/1710_12_Saeidi.

Saharan, M. R. and Mitri, H. (2011) 'Destress Blasting as a Mines Safety Tool: Some Fundamental Challenges for Successful Applications', in *Procedia Engineering*, pp. 37–47. Available at: https://doi.org/10.1016/j.proeng.2011.11.2137.

Sarkar, S., Toksoz, M. N. and Burns, D. R. (2004) 'Fluid Flow Modeling in Fractures', *Earth Resources Laboratory*, MIT Earth, pp. 1–41.

Serdyukov, S. V., Kurlenya, M. V. and Patutin, A. V. (2016) 'Hydraulic Fracturing for In-Situ Stress Measurement', Journal of Mining Science, 52(6), pp. 1031–1038. Available at: https://doi.org/10.1134/S1062739116061563.

Silva, J., Worsey, T. and Lusk, B. (2019) 'Practical Assessment of Rock Damage due to Blasting', *International Journal of Mining Science and Technology*, 29(3), pp. 379–385. Available at: https://doi.org/10.1016/j.ijmst.2018.11.003.

Singh, K. K., Singh, D. N. and Ranjith, P .G. (2014) 'Simulating Flow Through Fractures in a Rock Mass Using Analog Material', *International Journal of Geomechanics*, 14(1), pp. 8–19. Available at: https://doi.org/10.1061/(asce)gm.1943-5622.0000295.

Singhal, B. B. S. and Gupta, R. P. (2010) ‘Hydraulic Properties of Rocks’, in *Applied Hydrogeology of Fractured Rocks*. Second Edition. New York: Springer, pp. 139–140. Available at: https://doi.org/10.1007/978-90-481-8799-7.

SolidWorks D. S. (2021), *SolidWorks® Software*, Version 2021 [Computer Program], https://www.solidworks.com/. Waltham, MA, USA.

Stacey, T. R. (2010) ‘Preconditioning by Hydraulic Fracturing – What does it do and what are the issues in Modeling it ?’, Deep Mining 2010: *Proceedings of the 5th International Seminar on Deep and High Stress Mining*, Australian Centre for Geomechanics, Perth, pp. 135–142.

Suzuki, A., Kewen, L. and Horne, R. N. (2017) ‘Potential Utilizations of 3D Printed Fracture Network Model’, *42nd Workshop on Geothermal Reservoir Engineering*, (May), pp. 1–7.

Suzuki, A., Minto, J. M., Watanabe, N., Li, K. and Horne, R. N. (2019) ‘Contributions of 3D Printed Fracture Networks to Development of Flow and Transport Models’, *Transport in Porous Media*, 129(2), pp. 485–500. Available at: https://doi.org/10.1007/s11242-018-1154-7.

Tiab, D. and Donaldson, E. C. (2015) *Petrophysics Theory and Practice of Measuring Reservoir Rock and Fluid Transport Properties*. 4th edition. Gulf professional publishing.

Valerio, M., Rogers, S., Lawrence, K. P., Moffitt, K. M., Rysdahl, B. and Gaida, M. (2020) 'Discrete Fracture Network Based Approaches To Assessing Inter-Ramp Design', in *Proceedings of the International Symposium on Slope Stability in Open Pit Mining and Civil Engineering*, Perth, 12–14 May 2020.

Van As, A. and Jeffrey, R.. (2000) ‘Caving Induced by Hydraulic Fracturing at Northparkes Mines’, in *Pacific Rocks 2000: proceedings 4th North American Rock Mechanics Symposium*. Rotterdam, pp. 353–360.

Wang, H. F., Lee, M. Y., Doe, T. W., Haimson, B. C., Oldenburg, C. M. and Dobson, P. F. (2017) ‘In-Situ Stress Measurement at 1550-Meters Depth at the kISMET Test Site in Lead, S.D.’, in *51st US Rock Mechanics / Geomechanics Symposium*. San Francisco, pp. 2419–2425.

Wang, T., Xu, D., Elsworth, D. and Zhou, W. (2016) ‘Distinct Element Modeling of Strength Variation in Jointed Rock Masses Under Uniaxial Compression’, *Geomechanics and Geophysics for Geo-Energy and Geo-Resources*, 2(1), pp. 11–24. Available at: https://doi.org/10.1007/s40948-015-0018-7.

Witherspoon, P. A., Wang, J. S. Y., Iwai, K. and Gale, J. E. (1980) ‘Validity of Cubic Law for Fluid Flow in a Deformable Rock Fracture’, *Water Resources Research*, 16(6), pp. 1016–1024. Available at: https://doi.org/10.1029/WR016i006p01016.

Wong, J. W., Soga, K., Xu, X. and Delenne, J. Y. (2015) ‘Three Dimensional Simulation of Hydraulic Fracturing on Fault Using Lattice Element Method’, in *13th ISRM International Congress of Rock Mechanics*, Montreal, Canada, pp. 1–17.

Wu, F., Li, D., Fan, X., Liu, J. and Li, X. (2020) ‘Analytical Interpretation of Hydraulic Fracturing Initiation Pressure and Breakdown Pressure’, *Journal of Natural Gas Science and Engineering*, 76, pp. 103185 (1-13). Available at: https://doi.org/10.1016/j.jngse.2020.103185.

Xi, X., Yang, S., McDermott, C. I., Shipton, Z. K., Fraser-Harris, A. and Edlmann, K. (2021) 'Modeling Rock Fracture Induced by Hydraulic Pulses', *Rock Mechanics and Rock Engineering*, 54(8), pp. 3977–3994. Available at: https://doi.org/10.1007/s00603-021-02477-0.

Xin, W. and Cai, M. (2020) 'A DFN–DEM Multi-Scale Modeling Approach for Simulating Tunnel Excavation Response in Jointed Rock Masses', *Rock Mechanics and Engineering*, 53, pp. 1053–1077.

Xing, P., Yoshioka, K., Adachi, J., El-Fayoumi, A., Damjanac, B. and Bunger, A. P. (2018) 'Lattice Simulation of Laboratory Hydraulic Fracture Containment in Layered Reservoirs', *Computers and Geotechnics*, 100, pp. 62–75. Available at: https://doi.org/10.1016/j.compgeo.2018.03.010.

Xu, C., Dong, S., Wang, H., Wang, Z., Xiong, F., Jiang, Q., Zeng, L., Faulkner, L., Tian, Z. F. and Dowd, P. (2021) 'Modeling of Coupled Hydro-Thermo-Chemical Fluid Flow Through Rock Fracture Networks and its Applications', *Geosciences*, Switzerland, 11(4), pp. 1–36. Available at: https://doi.org/10.3390/geosciences11040153.

Yang, Y., Sun, D., Meng, W., Li, A. W., Wang, B. And Chen, Q. (2020) 'Deep Borehole In-Situ Stress Measurements By Hydraulic fracturing method in Xuefengshan Area', in *IOP Conference Series: Earth and Environmental Science*. Available at: https://doi.org/10.1088/1755-1315/570/4/042024.

Yong, S. and Maloney, S. (2015) An Update to the Canadian Shield Stress Database, Nuclear Waste Management Organization.

Zang, A. and Stephansson, O. (2009) *Stress field of the Earth's crust*, pp. 327. Berlin, Springer Science and Business Media.

Zhang, J. J. (2019a) 'Geomechanics Applications in Hydraulic Fracturing', in *Applied Petroleum Geomechanics*. Elsevier, pp. 441–481. Available at: https://doi.org/10.1016/b978-0-12-814814-3.00011-3.

Zhang, J. J. (2019b) 'Rock Physical and Mechanical Properties', in *Applied Petroleum Geomechanics*. Elsevier, pp. 29–83. Available at: https://doi.org/10.1016/b978-0-12-814814-3.00002-2.

Zhang, S., Qiao, W. G., Li, Y. Z., Song, W. J., Qin, J. L. and Wang, J. Y. (2019) 'Laboratory Simulation of Flow Through Rough-Walled Microfractures under high Hydraulic Gradient', *Geofluids, 2019*. Available at: https://doi.org/10.1155/2019/4098496.

Zhao, J., Li, J. and Jianchun, L. (2013) 'Mechanism and Experiment of Hydraulic Fracturing in Rock Burst Prevention' , in *Rock Dynamics and Applications State of the Art'*, Edited by Jian Zhao and Jianchun Li pp. 245–250. Available at: https://doi.org/10.1201/9781351181327.

Zhu, Q., Feng, Y., Cai, M., Liu, J. and Wang, H. (2017) 'Interpretation of the Extent of Hydraulic Fracturing for Rockburst Prevention using Microseismic Monitoring Data', *Journal of Natural Gas Science and Engineering*, 38, pp. 107–119.

Appendices

Appendix A Pressure-flow experiment results for Figure 4.15 (a) and (b)

	1.27" Orifice Plate		2.84" Orifice Plate	
Item	Pressure Difference (Pa)	Q (m^3/s)	Pressure Difference (Pa)	Q (m^3/s)
1	-	0.001	-	0.002
2	0.1	0.001	0.2	0.003
3	0.2	0.002	0.5	0.006
4	0.3	0.002	1.1	0.010
5	0.4	0.002	1.8	0.012
6	0.6	0.003	2.6	0.015
7	0.7	0.003	3.7	0.018
8	0.8	0.003	5.5	0.022
9	1.0	0.004	7.1	0.025
10	1.2	0.004	9.2	0.028
11	1.4	0.004	11.5	0.031
12	1.7	0.005	14.4	0.036
13	2.0	0.005	17.4	0.039
14	2.1	0.006	21.9	0.043
15	2.5	0.006	26.2	0.048
16	2.8	0.006	29.3	0.050
17	3.1	0.007	33.0	0.053
18	3.5	0.007	38.0	0.057
19	4.1	0.008	43.9	0.061
20	4.4	0.008	48.2	0.065
21	5.0	0.008	54.3	0.068
22	5.1	0.009	60.2	0.072
23	5.8	0.009	65.5	0.075
24	6.4	0.009	72.3	0.079
25	7.1	0.010	82.2	0.084
26	7.7	0.011	88.9	0.087
27	8.3	0.011	99.8	0.093
28	10.0	0.012	106.4	0.095
29	10.2	0.012	114.7	0.099
30	11.2	0.013	123.4	0.102
31	12.5	0.013	134.1	0.107
32	13.0	0.014	146.3	0.111
33	14.5	0.014	158.5	0.115
34	16.4	0.015	174.8	0.121
35	16.9	0.015	165.9	0.118
36	17.7	0.016	190.6	0.126
37	19.2	0.017	202.2	0.130
38	20.6	0.017	211.7	0.133
39	23.3	0.018	221.5	0.136
40	24.4	0.019	236.5	0.140
41	27.1	0.019	247.3	0.143
42	29.8	0.020		
43	30.7	0.021		
44	34.2	0.022		
45	37.1	0.023		
46	39.5	0.024		
47	43.5	0.025		
48	48.2	0.026		
49	52.6	0.027		
50	59.2	0.028		
51	54.6	0.028		
52	50.8	0.026		

Appendix B 1.27” Pressure-flowrate experimental results

1.27" Orifice Plate					
Item	Pressure Difference (Pa)	Q (m^3/s)	Item	Pressure Difference (Pa)	Q (m^3/s)
1	0.00	0	31	196.12	0.00471
2	4.40	0.00024	32	215.31	0.00500
3	8.30	0.00045	33	228.11	0.00515
4	10.20	0.00054	34	235.29	0.00526
5	11.10	0.00058	35	256.49	0.00553
6	15.41	0.00076	36	260.14	0.00561
7	19.42	0.00094	37	281.75	0.00587
8	22.32	0.00105	38	297.57	0.00602
9	26.84	0.00121	39	319.80	0.00630
10	30.45	0.00133	40	339.73	0.00655
11	31.56	0.00135	41	370.33	0.00688
12	34.87	0.00144	42	405.37	0.00733
13	39.10	0.00163	43	431.82	0.00757
14	45.02	0.00174	44	456.68	0.00782
15	54.07	0.00198	45	479.53	0.00813
16	60.51	0.00216	46	533.22	0.00855
17	62.02	0.00223	47	569.64	0.00889
18	66.85	0.00231	48	599.80	0.00910
19	76.31	0.00254	49	622.40	0.00933
20	82.57	0.00271	50	647.81	0.00956
21	94.24	0.00292	51	671.96	0.00975
22	100.00	0.00308	52	720.76	0.01010
23	108.66	0.00323	53	763.48	0.01047
24	115.92	0.00337	54	803.73	0.01077
25	121.17	0.00348	55	838.84	0.01103
26	130.02	0.00360	56	851.30	0.01113
27	141.85	0.00388	57	878.62	0.01134
28	158.99	0.00415	58	927.85	0.01166
29	176.97	0.00446	59	931.91	0.01170
30	192.48	0.00465	60	998.99	0.01216

Appendix C 2.84” Pressure-flowrate experimental results

2.84" Orifice Plate		
Item	Pressure Difference (Pa)	Q (m^3/s)
1	0.00	-
2	14.46	0.00116
3	30.95	0.00160
4	44.24	0.00193
5	62.83	0.00247
6	82.93	0.00269
7	97.83	0.00327
8	128.94	0.00390
9	156.05	0.00431
10	185.27	0.00481
11	208.08	0.00504
12	230.62	0.00556
13	265.73	0.00576
14	294.67	0.00631
15	320.39	0.00649
16	356.14	0.00698
17	377.55	0.00714
18	407.20	0.00752
19	443.46	0.00801
20	477.10	0.00835
21	508.66	0.00874
22	546.77	0.00880
23	603.27	0.00946
24	657.54	0.00986
25	720.13	0.01035
26	774.31	0.01082
27	861.54	0.01141
28	941.77	0.01202
29	965.11	0.01259
30	1039.27	0.01285
31	1113.41	0.01339
32	1133.17	0.01364
33	1289.08	0.01471

Appendix D Excel VBA Code for Velocity Conversion Calculations

```
Module1 - 1

Option Explicit

Function Cd(Beta As Double, Re As Double, L1 As Double, L2 As Double) As Double
    Dim a As Double
    Dim b As Double
    Dim C As Double

    a = ((19000 * Beta) / Re) ^ 0.8
    C = (2 * L2) / (1 - Beta)
    b = Beta ^ 4 / (1 - Beta ^ 4)

    Cd = 0.5961 + 0.0261 * Beta ^ 2 - 0.216 * Beta ^ 8 + 0.000521 * ((1000000# * Beta) / Re) ^ 0.7
    Cd = Cd + (0.0188 + 0.0063 * a) * (1000000# / Re) ^ 0.3 * Beta ^ 3.5
    Cd = Cd + (0.043 + 0.08 * Exp(-10 * L1) - 0.123 * Exp(-7 * L1)) * (1 - 0.11 * a) * b
    Cd = Cd - 0.031 * (C - 0.8 * C ^ 1.1) * Beta ^ 1.3
End Function

Function VelocityConversion(diameter As Double, orifice As Double, temperature As Double, pressure As
Double, L1 As Double, L2 As Double, deltaP As Double) As Double
    Dim tolerance As Double
    tolerance = 0.000001

    Dim initialVelocity As Double
    initialVelocity = 1

    Dim density As Double
    Dim viscosity As Double
    Dim isentropicCoefficient As Double
    Dim Beta As Double
    Dim E As Double
    Dim expansionCoefficient As Double

    density = pressure * 1000 / (287.04 * (temperature + 273.15))
    viscosity = (17 + 0.045 * temperature) * 0.000001
    isentropicCoefficient = 1.4
    Beta = orifice / diameter
    E = Sqr(1 / (1 - Beta ^ 4))
    expansionCoefficient = 1 - (deltaP / (isentropicCoefficient * (pressure * 1000 + deltaP))) * (0.41
 + 0.35 * Beta ^ 4)

    Dim Re As Double
    Dim velocity As Double
    Dim dischargeCoefficient As Double
    velocity = 0.01
    Do While Abs(velocity - initialVelocity) > tolerance
        Re = density * velocity * diameter / viscosity
        dischargeCoefficient = Cd(Beta, Re, L1, L2)
        initialVelocity = velocity
        velocity = Beta ^ 2 * E * dischargeCoefficient * expansionCoefficient * Sqr(2 * deltaP / densi
ty)
    Loop

    VelocityConversion = velocity
End Function
```